Angle-dependent deposition of thin amorphous hydrogenated carbon (a-C:H) layers on selected biodegradable polymer films

-

a geometrical control of the hybridization states

by

Lucas Beucher

Neugasse 1a
56070 Koblenz

Accepted Dissertation thesis for the partial fulfillment of the requirements for the degree of
DOCTOR RERUM NATURALIUM

at the
University of Koblenz
Department 3: Mathematics / Applied Sciences
Institute of Physics

Declaration of Authorship

I, Lucas Beucher, declare that this thesis and the work presented in it are my own, and I confirm the following:

- I have independently written the submitted dissertation and have properly acknowledged all tools and sources used in the work, as well as clearly identified the contributions of any collaborating colleagues or other authors.

- I have not sought or received paid assistance from any intermediary or consulting services.

- I have not submitted the dissertation in the same or similar form as an examination paper for a state or other academic examination in Germany or abroad.

- I have not submitted the same or a different dissertation in another field of study or at another academic institution.

- I am aware that a violation of any of the above points may result in the revocation of the doctoral title and could potentially have further legal consequences.

$Unterschrift:$ $Ort, Datum:$

Abstract auf Deutsch

Die aus nachwachsenden Rohstoffen hergestellten biologisch abbaubaren Polymere Polymilchsäure (*polylactic acid*, PLA) und Polyhydroxybuttersäure (*polyhydroxybutyrate*, PHB) wurden im Rahmen dieser Arbeit mit hydrierten amorphen Kohlenstoffschichten (*amorphous hydrogenated carbon*, a-C:H) bei unterschiedlichen Winkeleinstellungen mit verschiedenen Dicken beschichtet. Ähnlich wie herkömmliche Polymere haben Biopolymere oft ungeeignete Oberflächeneigenschaften für industrielle Zwecke, z.B. eine geringe Härte. Für manche Anwendungen ist es daher notwendig und vorteilhaft, die Oberflächeneigenschaften von Biopolymeren unter Beibehaltung der Haupteigenschaften des Trägermaterials zu modifizieren. Eine geeignete Oberflächenmodifikation ist das Aufbringen von dünnen a-C:H Schichten. Ihre Eigenschaften hängen wesentlich vom sp^2- und sp^3-Hybridisierungsverhältnis der Kohlenstoffatome und dem Gehalt an Wasserstoffatomen ab. Das $\frac{sp^2}{sp^3}$-Verhältnis sollte in der vorliegenden Arbeit durch Variation der Beschichtungsgeometrie gesteuert werden. Da Beschichtungen bei 0°, direkt vor der Plasmaquelle, einen höheren Anteil an sp^3 und indirekt (180°) beschichtete ein höheren Anteil an sp^2 aufweisen, wird in dieser Arbeit gezeigt, dass es möglich ist, das $\frac{sp^2}{sp^3}$-Verhältnis zu kontrollieren. Dazu werden die einzelnen Proben in den Winkeln 0, 30, 60, 90, 120, 150 und 180° vor der Plasmaquelle platziert und mit einer Dauer von 2.5, 5.0, 7.5 und 10.0 Minuten beschichtet. Für den Winkeln 0° ergaben sich die Schichtdicken von 25, 50, 75 und 100 nm. Die a-C:H Schichten wurden alle mit Radiofrequenzplasma-unterstützter chemischer Gasphasenabscheidung und Acetylen als C und H Quelle abgeschieden, nachdem sie 10 Minuten lang mit einem Sauerstoffplasma vorbehandelt worden waren. Nach dieser O_2-Behandlung und der a-C:H Abscheidung werden die Oberflächen mit makroskopischen und mikroskopischen Messmethoden untersucht und die Daten anschließend analysiert. Die Oberflächenmorphologie wird mit Hilfe der Rasterelektronenmikroskopie und der Rasterkraftmikroskopie erfasst. Auf diese Weise können auch Informationen über die Stabilität der Schicht und die Oberflächenrauhigkeit gesammelt werden. Mit Kontaktwinkelmessungen (*contact angle*, CA) wird nicht nur die Benetzbarkeit, sondern auch die Kontaktwinkelhysterese durch Auf- und Abpumpen des Tropfenvolumens bestimmt. Durch Messung des CA von verschiedenen Flüssigkeiten und deren Vergleich werden die freie Oberflächenenergie (*surface free energy*, SFE) und ihre polaren und dispersiven Bestandteile bestimmt. Die Veränderungen der Barriereeigenschaften werden durch Wasserdampftransmissionstests (*water vapor transmission rate*, WVTR) überprüft. Die chemische Analyse der Oberfläche erfolgt zum einen durch Fourier-Transformations-Infrarotspektroskopie mit spiegelnder Reflexion und zum anderen durch Synchrotron unterstützte Techniken wie der Nahkanten-Röntgenabsorptionsfeinstruktur und der Röntgen-Photoelektronenspektroskopie. Bei der Analyse der Oberflächen nach der O_2 Behandlung, von der zunächst angenommen wurde, dass sie nur der Reinigung und Aktivierung der Oberfläche für die a-C:H Beschichtung dient, wurde festgestellt, dass die Veränderungen drastischer sind als ursprünglich angenommen. Wird PLA zum Beispiel bei 0° für 10 Minuten behandelt, steigt die Rauheit um das Fünffache. Mit zunehmendem Winkel verringert sich diese wieder, bis sie bei 180° wieder dem Ausgangswert entspricht. Bei PHB hingegen wird durchgehend ein ähnlicher Wert gemessen. Für beide Polymere lässt sich zeigen, dass der polare Anteil der SFE zunimmt. In der WVTR ist bei PLA eine Abnahme der Permeabilität und bei PHB ein Anstieg des Ausgangswertes zu beobachten. Die chemische Ober-

flächenanalyse zeigt, dass die O_2-Behandlung kaum Auswirkungen auf die Oberflächenbindungen hat. Insgesamt kann in dieser Arbeit gezeigt werden, dass sich die O_2-Behandlung auf die Eigenschaften der Oberfläche auswirkt und nicht ausschließlich als Reinigungs- und Aktivierungsprozess betrachtet werden kann. Bei direkter a-C:H Beschichtung (bei 0°) ist sowohl bei PLA als auch bei PHB ein Schichtversagen bei 10.0 Minuten aufgrund von Eigenspannung zu beobachten. Dies ist bei PHB in geringerem Maße auch bei 30° zu erkennen. Die Durchlässigkeit der Polymere wird bei einer fünf minütigen Beschichtung um 47% reduziert und auch die Schicht bei 10.0 Minuten führt diesen Effekt trotz auftretender Risse weiter. Die Aufbringung von a-C:H Schichten zeigt für beide Polymertypen bei direkter Beschichtung eine Dominanz von sp^3-Bindungen. Mit zunehmendem Winkel nimmt diese ab und bei indirekten Beschichtungen werden sp^2-Bindungen dominierend. Dieses Ergebnis ist für alle Schichtdicken ähnlich, nur der Winkel, bei dem der Wechsel der dominanten Bindung stattfindet, ist unterschiedlich. Es wird gezeigt, dass es möglich ist, die Oberflächeneigenschaften durch eine winkelabhängige Beschichtung zu steuern und somit das Verhältnis $\frac{sp^2}{sp^3}$ zu kontrollieren.

Abstract in english

The biodegradable polymers polylactic acid (PLA) and polyhydroxybutyrate (PHB) produced from renewable raw materials were coated with hydrogenated amorphous carbon layers (a-C:H) at different deposition angles with various thicknesses as part of this thesis. Similar to conventional polymers, biopolymers often have unsuitable surface properties for industrial purposes, e.g. low hardness. For some applications, it is therefore necessary and advantageous to modify the surface properties of biopolymers while retaining the main properties of the substrate material. A suitable surface modification is the deposition of thin a-C:H layers. Their properties depend essentially on the sp^2 and sp^3 hybridization ratio of the carbon atoms and the content of hydrogen atoms. The $\frac{sp^2}{sp^3}$ ratio was to be controlled in the present work by varying the coating geometry. Since coatings at 0°, directly in front of the plasma source, contain a higher percentage of sp^3 and indirectly coated (180°) a higher amount of sp^2, it is shown in this work that it is possible to control the $\frac{sp^2}{sp^3}$ ratio. For this purpose, the samples are placed in front of the plasma source at angles of 0, 30, 60, 90, 120, 150 and 180° and coated for 2.5, 5.0, 7.5 and 10.0 minutes. For the angles 0°, the layer thicknesses were 25, 50, 75 and 100 nm. The a-C:H layers were all deposited using radio-frequency plasma-enhanced chemical vapor deposition and acetylene as C and H sources after being pretreated with an oxygen plasma for 10 minutes. Following the O_2 treatment and the a-C:H deposition, the surfaces are examined using macroscopic and microscopic measurement methods and the data is then analyzed. The surface morphology is recorded using scanning electron microscopy and atomic force microscopy. In addition, data on the stability of the layer and the surface roughness can be collected. Contact angle (CA) measurements are used to determine not only the wettability, but also the contact angle hysteresis by pumping the drop volume up and down. By measuring the CA with different liquids and comparing them, the surface free energy (SFE) and its polar and disperse components are determined. The changes in barrier properties are verified by water vapor transmission rate tests (WVTR). The chemical analysis of the surface is carried out on the one hand by Fourier transform infrared spectroscopy with specular reflection and on the other hand by synchrotron-supported techniques such as near-edge X-ray absorption fine structure and X-ray photoelectron spectroscopy. When analyzing the surfaces after the O_2 treatment, which was initially assumed to serve only to clean and activate the surface for the a-C:H coating, it was found that the changes were more drastic than originally assumed. For example, if PLA is treated at 0° for 10 minutes, the roughness increases fivefold. As the angle increases, it decreases again until it returns to the initial value at 180°. This can be recognized to a lesser extent with PHB at 30°. For both polymers, it can be shown that the polar fraction of the SFE increases. In the WVTR, a decrease in permeability can be observed for PLA and an increase in the initial value for PHB. The chemical surface analysis shows that the O_2 treatment has little effect on the surface bonds. Overall, it can be shown in this work that the O_2 treatment has an effect on the properties of the surface and cannot be regarded exclusively as a cleaning and activation process. With direct a-C:H coating (at 0°), a layer failure due to internal stress can be observed for both PLA and PHB. This also occurs with PHB at 30°, but to a lesser extent. Permeability of the polymers is reduced by 47% with a five-minute coating and the layer at 10.0 minutes continues to have this effect despite cracks appearing. The application

of a-C:H layers shows a dominance of sp^3 bonds for both polymer types with direct coating. This decreases with increasing angle and sp^2 bonds become dominant for indirect coatings. This result is similar for all coating thicknesses, only the angle at which the change of the dominant bond takes place is different. It is shown that it is possible to control the surface properties by an angle-dependent coating and thus to control the ratio $\frac{sp^2}{sp^3}$.

Contents

List of Figures

List of Tables

Part I.

Introduction and fundamentals of plasma physics and theory of layer deposition

1. Introduction

Polymers are an important raw material that can be found in almost all areas of modern life due to their advantages. These are mostly conventional crude oil based polymers. However, crude oil is a resource that is not available in unlimited quantities [1, p. 28-31]. Polymers in general are characterized above all by their easy formability, elasticity, low weight, a wide working temperature range and good chemical resistance [2, 3, 4, 5]. Conventional plastics also have a negative impact on human health, wildlife and the environment. Another important fact is the increasing production of plastic waste (e.g. packaging materials), as they do not decompose. Around 140 million tons of petroleum-based plastic waste are produced worldwide every year, of which 56.3 million tons are generated in Europe alone [6]. A fatal development with regard to plastic waste is that the average size of plastic particles in the environment seems to be decreasing. In addition, the global distribution of microplastic fragments has increased in recent years. The environmental impact of this microscopic waste is also still little known and, finally, the crude oil on which conventional polymers are based is always a political component [7, 8]. For this reason, it is all the more important to find suitable environmentally friendly alternative materials that can replace at least some of the conventional plastics used in industry. When it comes to saving resources and reducing the environmental impact, bio-based and biodegradable polymers can be an alternative product [1, p. 28-31][5]. Such biopolymers include polylactic acid (PLA) and polyhydroxybutyrate (PHB) [9, p. 3-7][10, 11, 12]. Similar to conventional polymers, these often have unsuitable surface properties for industry, such as low scratch resistance, low hardness and limited gas barrier properties [4, 13]. For some applications, it is therefore necessary and advantageous to modify the surface properties of biopolymers while maintaining the main characteristics of the substrate material. A suitable surface modification, such as the deposition of thin amorphous hydrogenated carbon layers (a-C:H) produced by radio frequency plasma-enhanced chemical vapor deposition (RF-PECVD), modifies the surface properties while preserving the main properties of the carrier material. The temperatures remain low in this process, making it suitable for materials such as polymers [14, 15, 16]. The properties of the a-C:H layers depend strongly on the acetylene (C_2H_2) precursor gas used and its purity. The resulting ratio of sp^2 and sp^3 hybridization of the carbon atoms and the amount of hydrogen atoms are decisive [14, 17, 18]. Due to the fact that C_2H_2 contains oxygen compounds for stabilization, it is possible that O is also incorporated into the layer or generates volatile molecules. If the sp^3 proportion of the layer is very high, this leads to a diamond-like layer, which is characterized by high hardness, chemical inertness, optical transparency or higher resistance. With a high sp^2 content, the layer becomes graphite-like and properties such as softer surfaces, better electrical conductivity or low friction are achieved [14]. This means that if the $\frac{sp^2}{sp^3}$ ratio is varied, customized surface properties can be created that are adapted to the application process. Which $\frac{sp^2}{sp^3}$ the layer has is in turn influenced by multiple factors: for example, it depends on the gas composition, the gas flow, the prevailing pressure and the ionization power [14, 17, 19, 20]. Another important factor is the coating geometry, which can be used to control the $\frac{sp^2}{sp^3}$ ratio. It is known that an a-C:H coating applied directly in front of the source forms sp^3 dominant layers, while coatings applied turned 180° away from the source (indirectly coated) are sp^2 rich [19, 20]. Preliminary experiments by the working group have already shown this phenomenon [15, 16, 21, 22, 23]. It

was also shown that it is possible to apply a-C:H to the biopolymers PLA and PHB using RF-PECVD [16, 24, 25, 26, 27, 28]. This is exploited in this work, and a-C:H is applied to PLA and PHB at different coating times (2.5, 5.0, 7.5 and 10.0 min) and resulting thicknesses (at $0°$: 25, 50, 75 and 100 nm) in an angle-dependent manner to confirm the gradual change from sp^3 (at $0°$ of deposition) to sp^2 ($180°$) richer layers in $30°$ steps. The relationship between the sp^2/sp^3 ratios and the macroscopic effects was investigated by contact angle (CA) measurements and surface free energy (SFE) determination. The expected improvement of the barrier properties of the a-C:H coated PLA films and uncoated PHB was verified by water vapor transmission rate (WVTR) tests. Prior to each coating, the surfaces were also treated with a 10 minute oxygen plasma in an angle-dependent manner to enable better deposition of the subsequent a-C:H layer. In this work it is also shown that the O_2 plasma process also has an effect on the surface properties of PLA and PHB.

The effects of the O_2 treatment and the a-C:H application in terms of their microscopic and macroscopic effects were all investigated ex-situ and subsequently analyzed. The surface morphology was recorded with two different methods. Macroscopic surface images were taken using scanning electron microscopy (SEM). Microscopic morphologies were made using atomic force microscopy (AFM). CA measurements also support contact angle hysteresis (CAH) by pumping the drop up and down, as well as surface free energy (SFE) by measuring the CA of different liquids. The chemical analysis of the surface was carried out using three different analysis methods. Firstly, specular reflectance Fourier transform infrared spectroscopy (SR-FTIR) was used and secondly, two surface-sensitive synchrotron X-ray techniques. These included near-edge X-ray absorption fine structure (NEXAFS) and X-ray photoelectron spectroscopy (XPS). The changing barrier and permeability properties of PLA and PHB films were determined by WVTR tests.

2. The fundamentals of plasma physics

In this work, the polymers PLA and PHB were treated with O_2 plasma and after a-C:H layers were deposited using RF-PECVD. First, the basics of plasma physics are discussed in order to highlight the most important physical aspects responsible for the layer growth behavior by a plasma process in the following chapter.

2.1. Definition of a plasma

Plasmas are referred to as the fourth state of aggregation alongside solid, liquid and gaseous. However, the transition from a gas to a plasma is not a phase transition in the thermodynamic sense. If a molecular gas is gradually dissociated into an atomic gas due to collisions caused by energy supplied that exceeds the molecular binding energy. If an increasing proportion of the atoms have sufficient kinetic energy to overcome the binding energy of the electrons in the outermost orbitals through collisions, the gas ionizes and a plasma is formed. Below the ionization limit of $kT \approx U_{ion}$, all particles are present as neutral atoms [29, p. 2 ff][30]. The plasma state can be generated in different ways. This thesis focuses on the generation of a plasma by discharge mechanisms. Gases are fundamentally poor conductors and distance and pressure-dependent dielectric strengths are specific to each gas. They are described by Paschens law. An electron must be accelerated by an electric field over a certain path length in order to obtain sufficiently high energy in the prevailing gas space. The breakdown voltage U_{break} results in [31, p. 158 ff]:

$$U_{break} = \frac{Bpd}{ln(Apd) - ln\left(ln\left(1 + \gamma^{-1}\right)\right)} \tag{1}$$

The two constants A and B can be determined experimentally. The electrode spacing is d, p as the prevailing pressure and γ as the Townsend coefficient [31, p. 158 ff].

To generate a discharge, an electric field is required, which is generated by two electrodes at a distance d apart. Between them is a gas as an insulator. This gas becomes conductive when the electric field becomes so large that its electrons are accelerated in the direction of the anode and its ions in the direction of the cathode. This is also known as the breakdown voltage. If a single electron is accelerated on its way to the anode to such an extent that it generates further electrons by colliding with non-ionized atoms, a cascade occurs. The boundary between dependent and independent discharge is known as Townsend's discharge mechanism. At the cathode, the ion bombardment generates further free charge carriers, which, among other things, generate radiation through recombination processes, which in turn releases new starting electrons and can lead to further ionization cascades [31, p. 158 ff][32, 33, 34][35, p. 515].
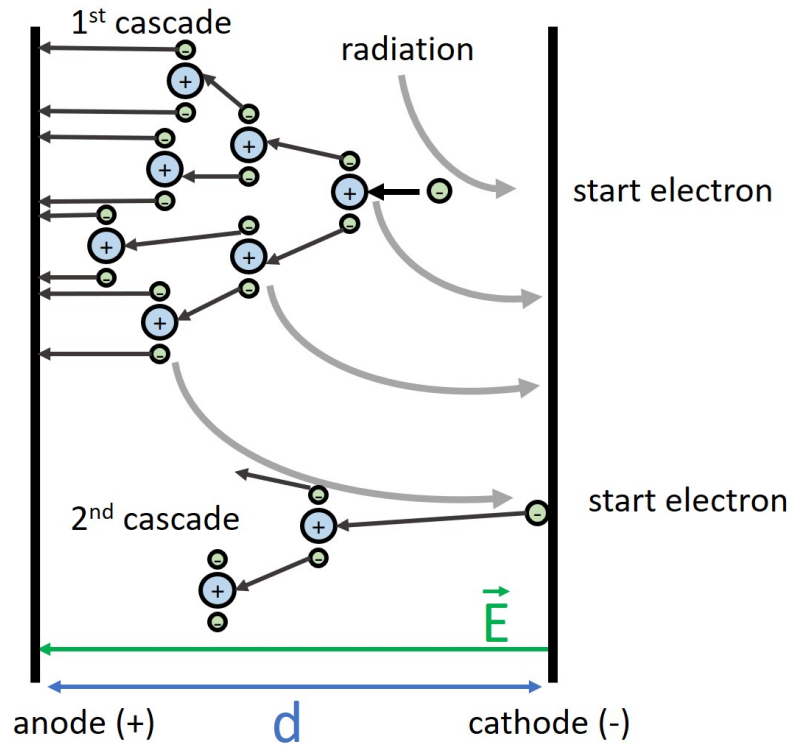
Fig. 1: Schematic model of a Townsend gas discharge. The figure is based on [31, p. 158 ff][32, 33]

The breakthrough and ignition conditions for plasmas in alternating fields depend on the mobility of the ions k and the applied field E_0 and the distance d between the electrodes. The frequency f derived from this then results [36, p. 384 ff]:

$$f = \frac{k \cdot E_0}{2\pi d} \cdot sin(\omega t) \tag{2}$$

At the maximum frequency f_{max}, a test ion just barely reaches the cathode from the anode, resulting in: $f_{max} = \frac{k \cdot E_0}{2\pi d}$. If the frequency $f > f_{max}$, a constant voltage is recorded between the electrodes. Space charge effects in the kHz - MHz range can still be neglected under this condition [36, p. 384 ff].

High-frequency plasmas are often excited at the standard frequency of 13.56 MHz, which is widely used for industrial applications; at high frequencies, the displacement current caused by the movement of the sheath and the scattering on the sheath contribute to ionization, so that lower voltages are sufficient to achieve higher plasma densities [37].

2.2. Distribution functions of a plasma

The distribution and propagation function within a plasma is a characteristic and can be described in different ways. The most important ones are briefly explained below [30].

2.2.1. Saha equation

To determine the degree of ionization X, the density of the neutral particles n_0 and the density of the charged particles n_e $[m^{-3}]$ are considered in the ratio $X = \frac{n_e}{n_e + n_0}$. If more than 50%

of the gas is ionized, $X \geq 0.5$ results. If the system is in thermodynamic equilibrium, this results in the so-called Saha ionization equilibrium [29, p. 184 ff][30]:

$$\frac{n_e}{n_0} = 2.405 \cdot 10^{21} \cdot T^{3/2} \cdot \frac{1}{n_e} \cdot exp\left(\frac{U_{ion}}{kT}\right) \tag{3}$$

With T as temperature at $X \geq 0.5$ and k as the Boltzmanns constant.

2.2.2. Boltzmann distribution

The Boltzmann distribution specifies the probability of occupation of the energy levels of a certain state. The function depends on the energy of this state and on the temperature of the system. The probability densities p and the energies E are considered in states i and j [38, p. 68 ff].

$$\frac{p_i}{p_j} = exp\left(\frac{E_j - E_i}{kT}\right) \tag{4}$$

2.2.3. Maxwell-Boltzmann distribution

The kinetic theory of gases describes the movement of gas molecules with a randomly distributed, continuous velocity and the mass m. This molecular motion depends on the gas temperature and is described by collisions with other molecules, which lead to a kinetic energy exchange. The molecules are considered as independent spheres with an average particle velocity v. The number of particles is assumed to be n [39, p. 33 ff][40, p. 11 ff].

$$f_n(v) = n \left(\frac{m}{2\pi kT}\right)^{2/3} \cdot v^2 \cdot exp\left(\frac{mv^2}{kT}\right) \tag{5}$$

2.3. Quasineutrality, Debye length and plasma frequency

Although a plasma consists of partially or completely ionized gas as described in section 2.1, a plasma is outwardly neutral. This means that the negative electron density n_e compensates for the sum of the positive charge carrier density n_p. The thermal energy of the particles and the resulting movement counteract this charge equalization. If the plasma is in thermal equilibrium and a point charge q is introduced into this system, the Poisson equation for the electric potential $\Phi = -\frac{1}{\lambda_D^2}$ applies [29, p. 6 ff][31, p. 141 ff]. The Debye length λ_D is defined by:

$$\lambda_D = \sqrt{\frac{\epsilon_0 kT}{n_e q^2}} \tag{6}$$

With ϵ_0 as electric field constant. If the potential equation is solved using a spherical approach, the potential Φ only depends on the distance r of the sample charge q and the result is [29, p. 8, 278 ff][30][31, p.101 ff]:

$$\Phi = -\frac{q}{4\pi\epsilon_0} \cdot \frac{1}{r} \cdot exp\left(-\frac{\sqrt{2} \cdot r}{\lambda_D}\right) \tag{7}$$

This leads to the following options:

- $r \gg \lambda_D$: The potential disappears exponentially. As a result, the potential of the test charge is shielded from the surrounding plasma for distances of more than the Debye length.

- $r \ll \lambda_D$: The exponential function is approximately one, which results in the Coulomb potential.

In order to describe electrons and ions not as individual particles but as a density distribution, there must be many particles in a defined volume. For this purpose, the number of particles N_D is defined in a sphere of radius λ_D, the so-called Debye sphere [29, p. 276 ff][30][31, p.141 ff].

$$N_D = \frac{4}{3}\pi \cdot n_e \cdot \left(\frac{\epsilon_0 kT}{n_e \cdot q^2} \right)^{\frac{3}{2}} \tag{8}$$

For $N_D \gg 1$, the Debye sphere consists of many particles and forms a shielding charge cloud, which results in Debye shielding. The limit $N_D = 1$ extends parallel to the limit $E_{pot} = kT$ for an ideal plasma, which means that Debye shielding is almost always present [31, p. 141 ff].

The displacement of the electrons relative to the ions creates high restoring forces in the plasma due to the electric field between the charged particles. Electrons are more mobile than ions due to their smaller mass. Due to their inertia, they oscillate harmoniously around the rest position of the ions, causing the electron-ion system to oscillate. The frequency of the system is referred to as the plasma frequency ω_P and the following applies [29, p. 292 ff][30][31, p.145 ff]:

$$\omega_P = \sqrt{\frac{n_e \cdot e^2}{m_e \epsilon_0}} \tag{9}$$

If an external electromagnetic field is generated, the following applies to the harmonic oscillator: below the plasma frequency ω_P, electromagnetic waves are reflected and cannot penetrate the plasma, which is referred to as 'cut-off'. Above ω_P, a plasma becomes transparent to electromagnetic radiation[29, p. 583 ff][30].

2.4. Rate equations and elementary processes

The plasma used for layer deposition involves a large number of chemical reactions and equilibrium processes that influence the particles present. Due to the high speed, many processes are triggered by electron collisions. These lead to further ionization reactions or they can recombine with positive ions. Negative particles can also be generated. There are also collision processes with ions and fragments of partially or completely dissociated molecules, as well as with neutral particles. Charge transfer effect can also occur among the different plasma species. The chemical reaction rates depend on the particle concentration and the energy distribution of the reaction partners [30][31, p. 14 ff]. Reactions of particles of the type A or B are described below. Electrons are marked with e, positive charges are marked with $+$, negative with $-$.

The most important processes are listed:

- Impact ionization, electron-ion pair: $e^- + A \rightarrow A^+ + e^- + e^-$

- Impact ionization, negative ion: $e^- + AB \rightarrow A^- + B$

- Produce radical: $e^- + AB \rightarrow A + B + e^-$

- Recombination: $e^- + A^+ \rightarrow A$

- Charge transfer: $A^+ + B \rightarrow A + B^+$

3. Theory of film deposition

In this work, coatings of different thicknesses are applied to surfaces. Deposits on surfaces are important in many industrial manufacturing processes. The possible layer thicknesses range from a few nanometers to a few micrometers, depending on the application. The growth and deposition behavior of the layers is described in detail in this section. Layer formation is explained in six consecutive steps [41, p. 119].

1 First, incident particles are adsorbed on the surface.

2 After they often diffuse a certain distance on the surface.

3 Then the particles react with free binding sites of the surface atoms or with other deposited particles.

4 These bound particles are referred to as nuclei, on which more and more particles accumulate and the layer begins to grow.

5 If the layer becomes thicker, it develops a structure or morphology and a roughness.

6 Finally, diffusion interactions occur within the layer mass and with the surface.

3.1. Physisorption and chemisorption on the surface and diffusion

Fig. 2 shows the impingement of the species deposited from the plasma and the possible sequential deposition steps of an impacting particle on the substrate surface until it is deposited. When these particles approach the surface, an interaction takes place. The surface applies an attractive force to these particles within a few atomic distances and they are attracted to the substrate surface (Fig. 2). These move along the potential to its minimum, where they are attracted by the nuclei. If the incoming particles have sufficient kinetic energy, they remain on the surface and trapped in a weakly-adsorbed state known as physical adsorption or physisorption (Fig. 2 and 3). If the particle cannot dissipate enough energy as it approaches the substrate for physisorption to take place, it is reflected back from the surface [39, p. 340 ff][41, p. 119 ff][42, p. 127 ff].
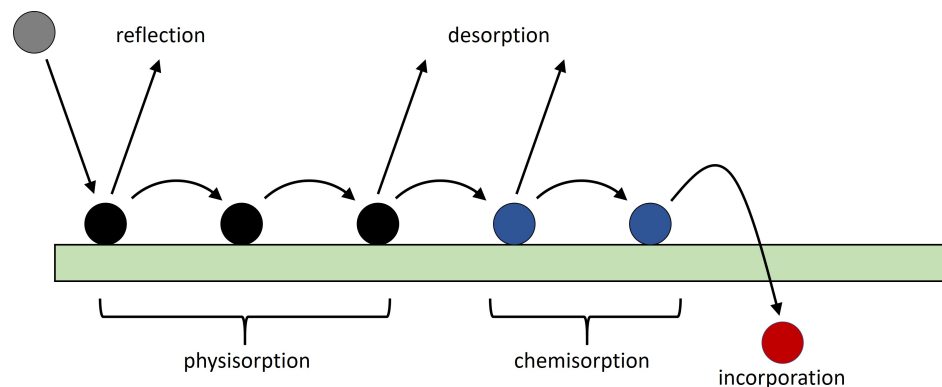
Fig. 2: Schematic model of the impact of an unbound particle (gray) from the plasma on the substrate surface. The resulting possible interactions are shown. The black particles are weakly bound (physisorbed), the blue ones are chemisorbed (strongly bound) and the red ones are incorporated into the layer. The figure is based on [41, p. 120].

In physisorption, the particle is only weakly bound to the surface by the van der Waals force and is in a first potential minimum (Fig. 3A/B). Accordingly, it can move on the surface between the atomic sites, which is called diffusion. If the physisorbed particles acquire enough energy during diffusion, they can desorb from the surface Fig. 2 3A/B) [39, p. 442][41, p. 119 ff][42, p. 133 ff]. The desorbed and reflected particles can hit the surface again from the plasma and start the application process all over again. If the physisorbed particles continue to interact with the surface, they can reach a lower energy potential and form a chemically more stable bond with the surface (see Fig. 3A/B). The particles are now no longer bound only by dipole interactions, but the electrons of the incident particles and the surface atoms enter into new molecular orbitals. This is known as chemisorption [41, p. 119 ff][42, p. 133 ff].
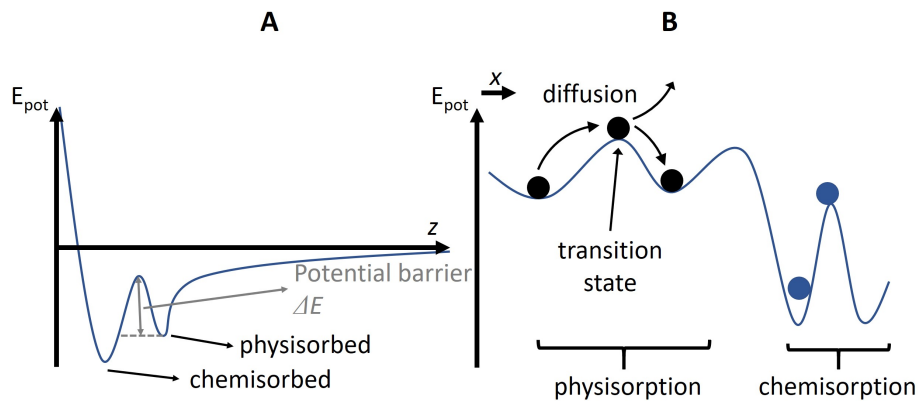
Fig. 3: A The potential energy of a particle as a function of the distance to the substrate surface z is shown. **B** The potential energy of surface diffusion as a function of the position x on the surface. The respective state of physisorption and chemisorption is shown. The figure is based on A [41, p. 123] and B [41, p. 130].

In Fig. 3A the potential energy of a particle as a function of the distance to the substrate surface z is shown. The energy curve shows the lower potential of the chemisorbed state compared to physisorption. The potential barrier ΔE between the two states must be overcome if a physisorbed particle is to switch to chemisorption and thus to the more strongly bound state. How big ΔE is depends on how strong the bonds of the particles are within the precursor state and the surface from their relaxed state [41, p. 122 ff][42, p. 156]. Fig. 3B shows the potential curve of a particle moving on the surface in different bonding states. If the particle is at an energy maximum, this is referred to as a transition state. At the maximum, the particle can desorb or diffuse on the surface. The particle can also move from a physisorbed state to a physisorbed state, whereby it ends up in a deep potential minimum [41, p. 129 ff]. In plasma-enhanced chemical vapor deposition processes, such as those used for this work, the species entering are already activated and therefore chemisorbed directly on the surface. The physisorption state does not occur. To achieve this, the quantity of the molar potential energy of the incoming vapor must be high enough [41, p. 122 ff].

3.2. Nucleation and growth modes

The introduction of the particles into the substrate marks the start of nucleation and thus the growth of the layer. To do this, the free molecular contacts on the surface must be removed or

saturated. To achieve this, bonds must be broken and energy expended. This is influenced by the surface free energy (SFE) γ. The SFE is provided by the forces generated during surface formation and always aims for a minimum. Minimization is achieved through surface diffusion, which strongly influences the formation of surface structures and topography. The chemical composition of the surface, the crystallographic orientation, the atomic reconstruction and the roughness on an atomic scale are also influencing factors. The SFE is therefore the stored work per unit area and is given in J/m^2 or N/m [41, p. 139 ff][42, p. 337]. For deposition on a surface, the surface energies of the free substrate surface γ_s, the layer surface γ_l and the substrate-layer interface γ_i must be taken into account. If the particles can diffuse sufficiently well on the surface, the deposited material can minimize its SFE itself. In this case, nucleation is not kinetically limited. For this, the diffusion length Λ must be much greater than the distance a between the atomic layers ($\Lambda \gg a$), a so-called equilibrium growth mode is present [41, p. 142 ff]. If there is no diffusion, or $\Lambda \ll a$, each atom sticks directly where it lands. This is referred to as a non-equilibrium growth mode [41, p. 142 ff][42, p. 228].

3.2.1. Equilibrium growth modes

Fig. 4 shows three different options for layer equilibrium growth mode. These are determined by the sign of the SFE difference [39, p. 195 ff][41, p. 143 ff].
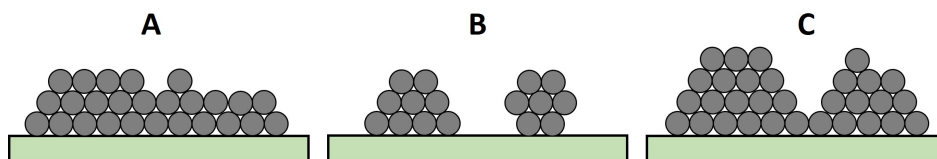
Fig. 4: Layer growth modes in equilibrium mode: **A** Frank-Van der Merwe (layer), **B** Volmer-Weber (island), and **C** Stranski-Krastanov. The figure is based on [39, p. 197][41, p. 144].

In the Frank-Van der Merwe growth mode (Fig. 4A), the deposited layer wets the substrate surface. This results from the fact that the free substrate surface γ_s is larger than the layer surface γ_l and the substrate-layer interface γ_i, which results in the following [41, p. 143]:

$$\gamma_s > \gamma_l + \gamma_i \tag{10}$$

This means that the SFE of the coating surface is lower than that of the raw substrate surface, resulting in very uniform layer growth. The bond between the deposited layer and the surface must be strong in order to reduce γ_i [39, p. 195 ff][41, p. 143 ff].

If the free substrate surface γ_s is smaller, the layer begins to form three-dimensional (3D) islands on the surface and does not cover the surface evenly. This follows [39, p. 195 ff][41, p. 143 ff]:

$$\gamma_s < \gamma_l + \gamma_i \tag{11}$$

Due to the island formation, the contact with the surface is reduced, which is referred to as the Volmer-Weber growth mode (Fig. 4B) [39, p. 195 ff][41, p. 143 ff].

The Stranski-Krastanov growth mode (Fig. 4C) is a hybrid between the Frank-Van der Merwe and the Volmer-Weber growth mode. The layer-to-layer growth changes one or two

monolayers to a 3D island growth. This results from the fact that the SFE of the layer surface γ_l becomes larger than the SFE of the free surface γ_s after the completion of the first layers. This mode is the most frequently observed for the deposition of layers on solids [39, p. 195 ff][41, p. 143 ff].

3.2.2. Non-equilibrium growth modes

Initially, all growth modes can be observed as being in equilibrium. To do this, the forward and reverse reaction rates of the reactants involved in layer growth must be so fast that they equalize within the time scale of a monolayer deposition. If this is not the case, the system is driven away from the equilibrium state. For example, due to differing reaction rates of individual species on the surface or their diffusion rates (as in the case of plasma deposition). If, for example, the forward speed is so slow that the product concentration does not have time to reach an equilibrium level within this time scale, the concentration is determined by the kinetics of the reaction and not by thermodynamics [41, p. 150 ff][42, p. 354 ff]. Whether kinetics or thermodynamics determines layer growth depends on the rate constants of various surface processes and their kinetic balances. The applicable rate constants are usually unknown, as these are dynamic processes that are carried out in the absence of back reactions. In CVD processes, it is particularly imprecise to determine these velocities due to the many different reactions. In principle, two parameters can be modified to control the system out of the equilibrium state: The temperature and the pressure [41, p. 150 ff]. If the kinetic process dominates the layer growth, the kinetic equilibrium of several different surface processes must be analyzed. The basic processes are shown in Fig. 5 and take place after chemisorption in addition to the deposition step. Parallel to deposition, nucleation of particles on the surface, terrace diffusion, accommodation of atoms on formed steps or diffusion across these steps also take place [42, p. 355 ff].
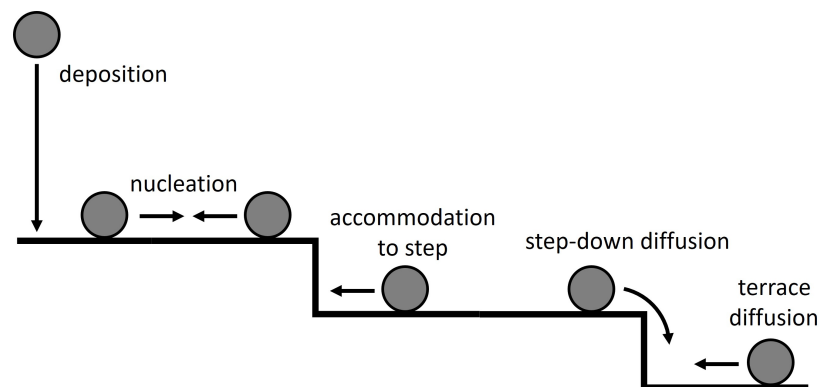
Fig. 5: Surface processes involved in non-equilibrium layer growth. The figure is based on [42, p. 356].

In energetic terms, step-down diffusion is significant, especially at low process temperatures. The reason for this is that the particles are more strongly bound at the bottom of the steps. The relative process rates of the different processes determine the growth mode and the morphology of the layer. In a non-equilibrium state, the layer growth can be divided into three different growth modes [42, p. 355 ff]. This is shown in Fig. 6.

Close to equilibrium, a step flow growth is the predominant growth process (Fig. 6A). There is no material transport between neighboring layers. Likewise, terrace diffusion is so

fast that all particles reach a stage before islands can nucleate. The nucleation of islands occurs rapidly when the system is far from equilibrium. The growth mode of the island is characterized by the transport between the adjacent layers. The layer is formed by the coalescence of 2D islands that occur at the boundary of the transport. No new nucleation takes place on these 2D islands until the gaps between the islands are filled. This growth mode is shown in Fig. 6B. Fig. 6C illustrate the state when nucleation occurs on the islands before the layer is closed. This starts when there is no or too little transport between the layers and is called 3D multilayer growth. The higher the amount of deposit deposited on the surface, the greater the number of new islands that grow on islands. As a result, the system moves further and further away from the equilibrium state and becomes rough due to the pyramid-like structures that form [42, p. 355 ff].
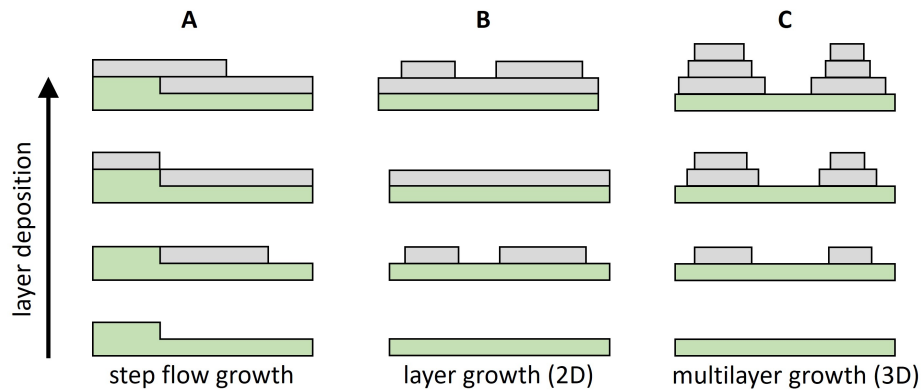
Fig. 6: Schematic layer growth modes at non-equilibrium: The substrate is shown in green. **A** shows the substrate step flow growth, **B** the Layer growth by island coalescence and **C** a multilayer growth. The deposition increases from bottom to top. The figure is based on [42, 357].

The distinction between layer and multilayer growth (Fig. 6B/C) can be described qualitatively. For this purpose, the critical layer coverage Θ_C is considered, at which the nucleation takes place on the growing islands. The coverage Θ_{coal}, at which the islands grow together to form a coherent layer, is also considered. For the conditions of the growth modes follows from this [42, p. 355 ff]:

$$\Theta_C > \Theta_{coal} \Rightarrow \text{layer growth}$$

$$\Theta_C < \Theta_{coal} \Rightarrow \text{multilayer growth}$$

General, Θ_C ranges in the interval $\{0.5 \leq \Theta_C \leq 0.8\}$. The critical layer coverage can be increased by reducing the deposition rate or increasing the temperature. Variable process parameters that determine the growth mode include pressure and temperature. The system temperature T_s determines the diffusion rate and the pressure determines the deposition rate r_{dep}. For $T_s \to \infty$ and $r_{dep} \to 0$, the system approaches the equilibrium state and step flow growth is observed. At $T_s \to 0$ and $r_{dep} \to \infty$ the transport between the layers comes to a standstill. Nucleation is then not yet complete and multilayer growth takes place. In summary, step-flow growth is preferred at high temperatures and low deposition rates and multilayer growth is preferred at low temperatures and high deposition rates [42, p. 355 ff].

3.3. Nucleation rate, grains and coalescence phenomena

The nucleation rate describes how many nuclei of critical size form on a substrate surface per unit area and time. This is relevant because the formation of a new phase is not possible without the existence of nuclei. The size of the nuclei r is crucial so that they can be used for further layer growth. Small nuclei are thermodynamically unstable and shrink as their free energy change ΔG_γ tries to minimize $(d\frac{\Delta G_\gamma}{dr} \rightarrow 0)$. So-called critical nuclei r_c lack only one atom to be thermodynamically stable and thus to be used for layer growth. The speed at which critical nuclei grow depends on how quickly adsorbed monomers (so-called adatoms) attach to the nuclei. High-energy particles that hit the surface usually remain there for a period of time τ_s. During this time, they can attach to the nuclei [39, p. 201 ff].

$$\tau_s = \frac{1}{\nu} \cdot exp\left(\frac{E_{des}}{kT}\right) \tag{12}$$

The vibrational frequency ν is typically in the range of $10^{12} \ \frac{1}{s}$, and E_{des} is the energy required to desorb it back into the vapor. Adatoms that have not yet thermally adapted to the substrate perform random diffusion jumps. They can also form pairs with other atoms during their movement and then join together to form larger grains or they can be captured by existing grains. When this happens, it is improbable that these atoms will return to the vapor phase. As the grains continue to grow, coalescence can occur between different grains. Three mass transport mechanisms have been proposed to explain these phenomena which are shown in Fig. 7. These include Ostwald ripening, sintering and cluster migration [39, p. 201 ff].
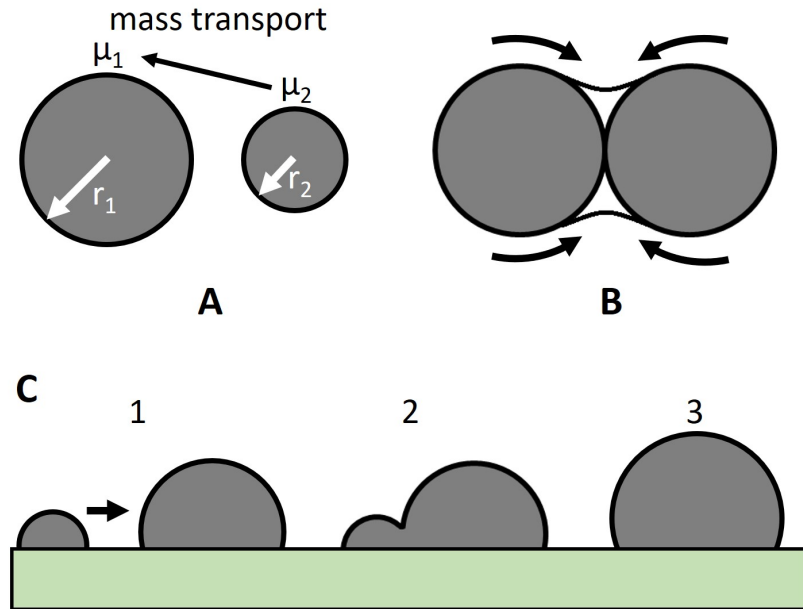
Fig. 7: Coalescence phenomena of islands on the substrate surface. **A** Ostwald ripening, **B** sintering and **C** cluster migration. The cluster migration is additionally separated in three parts: **1** cluster migration, **2** cluster collision, **3** merged cluster. The figure is based on [39, p. 214].

So-called Ostwald ripening coalescence occurs when, in an accumulation of grains of different sizes, the larger ones grow at the expense of the smaller ones. The reason for this is that the SFE is minimized as a result of the aggregation. First, two isolated but closely spaced

grains are considered. The grains are of different size and surface energy γ, as shown in Fig. 7A. For simplification, it is assumed that the grains are spherical $r_{1,2}$. The free energy G_γ of a grain is with $i = 1, 2$ [39, p. 214 ff]:

$$G_{\gamma/i} = 4\pi\gamma r_i^2 \tag{13}$$

The number of atoms n_i bound in the islands can be calculated as [39, p. 214 ff]:

$$n_i = \frac{4\pi}{3\Omega}r_i^3 \tag{14}$$

Ω is the atomic volume of the individual grains. The free energy per atom μ_i results from the derivation of the free energy according to the atomic volume [39, p. 214 ff]:

$$\mu_i = \frac{dG_{\gamma/i}}{dn_i} = \frac{8\pi\gamma r_i dr_i}{4\pi r_i^2 dr_i/\Omega} = \frac{2\Omega\gamma}{r_i} \tag{15}$$

If μ is large, the atomic concentration is also large. The atoms are forced to migrate to smaller μ values. Above $r_1 > r_2$, the free energy is $\mu_1 < \mu_2$. This means that atoms from nucleus 2 migrate across the surface to nucleus 1. It is a transport mechanism in which no direct contact between the nuclei is required [39, p. 214 ff].

Fig. 7B shows the coalescence phenomenon of sintering. Here, the grains must be in contact so that a neck can form. Diffusion of atoms causes the neck to become larger and larger, thus minimizing the surface energy of the system. The energy for atoms in the convex part of the grains exceeds the energy of the atoms in the concave parts. As a result, an effective concentration gradient develops between these two regions, which leads to mass diffusion in the direction of the neck [39, p. 215 ff].

Fig. 7C shows coalescence due to collisions between individual grains. It is divided by three different steps: C1 the grain migration, C2 the grain collision and C3 the formation of the combined grains. The migration of grains takes place after the end of deposition. I.e. in systems in which the mass of the deposit remains constant (conservative system). The diameter of the grains is usually between 5 nm and 10 nm. If the substrate temperature is high enough (min. $450K$), these grains can migrate, which can lead to grain collision. The coalescence of these conservative systems is characterized by a lower density of the grains, their larger average volume and a lower coverage of the substrate [39, p. 217 ff].

3.4. Layer structure development

As the layer thickness increases, the surface develops according to the non-equilibrium processes shown in Fig. 6. At the same time, as the deposition progresses, the layer volume also changes to mainly three different main types and one transition zone of bulk structures within the coating. The amount of thermally driven motion that takes place during layer growth is decisive for the structure that forms. This is characterized by the ratio $\frac{T_s}{T_m}$ between the substrate temperature T_s under working conditions and the melting temperature T_m of the growing layer. At the same time, the resulting structure is also determined by the amount

of additional energy supplied to the growth surface. The three different resulting structural zones (Fig 8: Z1, Z2 and Z3), which are created during layer deposition, are shown in Fig. 8. A intermediate transition zone ZT can also be classified between Z1 and Z2.
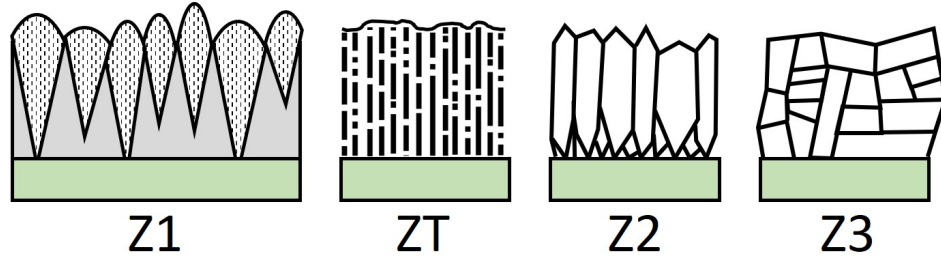
Fig. 8: Schematical characteristics of the three basic structural zones as a cross-section during layer deposition and one transition zone. The ratio of substrate temperatur T_S to layer melting temperatur T_L increases in the direction $Z1 \rightarrow ZT \rightarrow Z2 \rightarrow Z3$. The figure is based on [41, p. 160].

In the following the different structural zones are described:

If the ratio of substrate to melting temperature $\frac{T_s}{T_m} < 0.3$ and the core diffusion length Λ is smaller than a, surface diffusion can be neglected. The layer then consists of inverted conical columns with characteristic diameters in the order of a few tens of nm (Fig. 8Z1). The cones end in domes on the surface (this increases with increasing layer thickness). The cone structures are separated by voids with a size of a few nm. The columns have a low crystallinity (many defects) or are ultimately amorphous. As the layer thickness increases, the structures overlap, forming a collection of cones with wider cavities between them [39, p. 226 ff][41, p. 159 ff].

The transition zone ZT (Fig. 8ZT) occurs when surface diffusion processes are negligible, i.e. $\lambda < a$. Similar to Z1, it consists of defective columns, but the voids are smaller ($\sim 0.5\ nm$) and there are no domes. The ZT structure occurs in energy-enhanced processes [39, p. 226 ff][41, p. 159 ff].

If the temperature ratio is in the interval $\{0.3 < \frac{T_s}{T_m} < 0.5\}$, the surface diffusion must also be taken into account. The structure (Fig. 8Z2) consists of columns with narrow edges and a characteristic diameter that increases with increasing $\frac{T_s}{T_m}$. The grain boundaries of the columns are very dense and the surface often appears faceted. The Z2 structure can also occur in amorphous films, but the column boundaries tend to be flatter [39, p. 226 ff][41, p. 159 ff].

Z3 occurs at $\frac{T_s}{T_m} > 0.5$ (Fig. 8Z3). Considerable annealing of the layer occurs during the deposition process and considerable diffusion takes place at the surface. The Z3 structure has isotropic or equiaxed crystallite shapes. Grooves can form at the grain boundaries in this structure [39, p. 226 ff][41, p. 159 ff].

The transition from one structure to another is not always abrupt with increasing $\frac{T_s}{T_m}$. This is because the transition temperature in the systems depends not only on the substrate, but also on system parameters such as ion energy, ion flux, surface energy anisotropy or the coating angle. A different structure can be detected at different layer depths due to the possibly changing parameters. Amorphous coatings only have such a structure in the case of inhomogeneity because they do not have a crystallographic pattern that defines a boundary between the grains [41, p. 159 ff].

Part II.

Amorphous hydrogenated carbon coatings on bioplastic materials and the characterization methods

4. Substrate materials

This chapter provides an overview of the biopolymers used in this thesis. A brief insight into the definition of these polymers and a short introduction is necessary.

Plastics or polymers are nowadays used in many everyday objects. Examples include laptops, smartphones, packaging materials and countless other things [2, 3]. Polymers are composed of macromolecules, which are usually linked by covalent bonds between the basic building blocks known as monomers. During the production of polymers, they are covalently linked one after the other as recurring units until they are referred to as macromolecules. The properties relating to the interactions of the polymer depend on its macromolecular structure [43][44, p. 4]. Most of the plastics used today are thermoplastics. For simple applications such as packaging, for example, polyethylene or polyethylene terephthalate (PET) are used [45, p. 4-7][46, p. 17-19]. Thermoplastics consist of physically linked or linearly branched macromolecules and are subject to a series of reversible property changes due to temperature fluctuations. They are hard at low temperatures and soften when heated to a plastic state in which they can be deformed relatively easily. Most commercial polymers used in industry are made of non-biodegradable material and are produced from crude oil. This leads to disposal problems and environmental pollution, among other things because they are normally broken down very slowly in the environment by natural microorganisms and enzymes [9]. A fatal development with regard to plastic waste is also that the average size of plastic particles in the environment is decreasing and so-called microplastics are being created. The environmental impact of this microscopic waste is still poorly understood and the identification and quantification of this is still part of scientific research [7, 47, 48].

In recent decades, due to environmental awareness and the implementation of increasingly stringent politically motivated environmental regulations, more efforts have been made to establish biopolymers [49]. As a result, they are becoming an increasingly important raw material. A distinction is also necessary within biopolymers and is divided into three categories (Fig. 9). Firstly, plastics that are obtained from renewable raw materials but are not biodegradable. Secondly, polymers made from renewable raw materials that are also biodegradable, and thirdly, polymers that were involved in the extraction of crude oil but are biodegradable [50, p. 21-29].
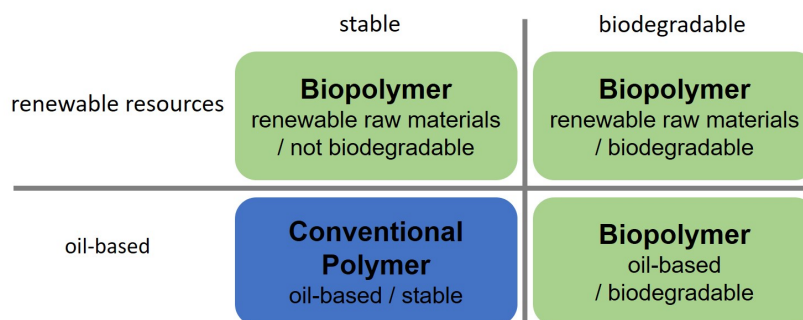
Fig. 9: Classification of the different types of biopolymers. The figure is based on [50, p. 6].

The following two biopolymers were selected for this work due to their wide range of industrial applications.

4.1. Polylactide acid
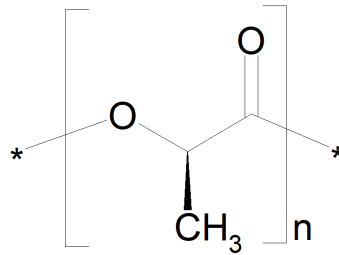
Fig. 10: Structural formula of PLA ($[-OCH(CH_3)CO-]_n$).

polylactide acid (PLA) is a biodegradable thermoplastic polymer that is produced from renewable raw materials such as potatoes or cassava roots [10, 11, 12]. The chemical structure of PLA is shown in Fig. 10 and consists of oxygen and carbon in the backbone and a methyl group ($-CH_3$) as a side chain. PLA is mainly produced using two different manufacturing processes. Firstly, PLA can be produced by fermenting biological materials such as starch with the help of bacteria, fungi or cell cultures. On the other hand, it can also be synthesized by condensation polymerization of lactic acid or by ring-opening polymerization of lactide with the help of a catalyst. Production by fermentative processes accounts for the majority ($70 - 90\%$) of the production volume [50, p. 103-108][51]. PLA has a pore structure due to the manufacturing process. Such a pore is shown in an AFM image in Fig. 11.
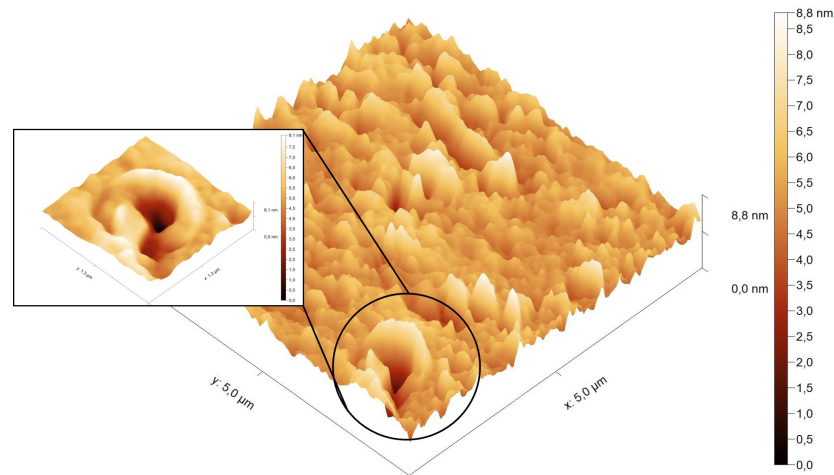
Fig. 11: Production-related pore of PLA, shown in a 3D AFM image.

Due to the thermoplastic character of PLA and numerous industrial processes, it can be used in a wide range of application [50, p. 187-194][52]. As PLA is biocompatible, i.e. compatible with biological substances, it can also be used in medical applications [53]. Due to its optical transparency, it is also used in the food industry as a packaging material or in the textile industry. [10]. For the present PLA the CA of 79.64° and a water vapor permeability of 122 $g/(m^2 \cdot 24\ h)$, which severely limits its range of application in food packaging [54]. It also has a melting range of $170 - 180\ °C$ and a heat deflection temperature of $55\ °C$. The glass transition temperature is around $60\ °C$. This is comparable to PET [52, 55], and

outlines the temperatures at which PLA can be further processed. PLA film with a thickness of 50 μm was delivered in industrial quality from Goodfellow GmbH, Friedberg, Germany and were cut to 10×5 cm pieces.

4.2. Polyhydroxybutyrate
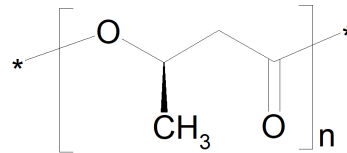
Fig. 12: Structural formula of PHB ($[-OCH(CH_3)CH_2CO-]_n$).

Polyhydroxybutyrate (PHB) is a biodegradable thermoplastic polymer. It is produced from renewable resources and is a polyhydroxyalkanoate (PHA). The structure of PHB is shown in Fig. 12 and, similar to the structure of PLA, consists of oxygen and carbon in the backbone and a methyl group ($-CH_3$) as a side chain. PHB is obtained from fermentative production processes. This usually involves the use of sugar and starch, which are processed by microorganisms [9, p. 3-7]. PHB serves as an energy and carbon store for the organisms. Two different types of microorganisms can be used. One type produces PHB continuously and the others produce PHB only when the substances required for their growth are lacking but there is an excess of carbon [50, p. 121-128]. PHB can be hydrolyzed by extracellular PHA depolymerases, and the cleavage products are then used by many organisms as a source of carbon and energy, as described above. PHB is therefore degraded without residues. Some microorganisms are able to degrade 90% of a PHB film at 50 $°C$ after five days [50, p. 121-128][56]. As PHB, like PLA, has good body compatibility and biocompatibility, it is also used for medical products [53, 57]. Another area of application for PHB is the packaging industry, where it is also used for foodstuffs. It also has a melting point of about 179 $°C$ and a glass transition temperature of 60 $°C$ [58, 59]. An industrial grade PHB blended film with a thickness of 25 μm and a content of 8% polyhydoxyvalerate was supplied by Goodfellow GmbH, Friedberg, Germany, and cut into 10×5 cm pieces. The present PHB appears milky and has a measured CA of 74.95°.

5. A general overview of amorphous hydrogenated carbon layers (a-C:H)

In this section, the deposited amorphous hydrogenated carbon (a-C:H) layer is examined in more detail and the fundamentals are explained. The a-C:H deposition mechanism is described. In particular, how a layer is deposited on a polymer surface and which conditions are involved in the process. Finally, the experimental details and the coating process are described and the interaction between polymer and coating is examined.

5.1. Definition of a a-C:H layer and the cluster network

a-C:H is a metastable form of amorphous carbon, which consists of differently hybridized carbon atoms in which hydrogen could be incorporated. First, the different hybridization states are shown in Fig. 13. The 2s and the different 2p orbitals of the carbon form the so-called sp^3-, sp^2- and sp^1-bonds [14][60, p. 3 ff].

In the sp^3 configuration, the four valence electrons of a carbon atom are each aligned tetrahedrally, as in a diamond (C−C). One electron from the $2s$ orbital and one from the $2p$ orbital change to an energetically more favorable hybrid. The four resulting hybrid orbitals are oriented with the greatest possible distance to each other in space, which corresponds to the tetrahedral structure (109.5°). As a result, the electron (or electron orbital) binds covalently (σ-bond) to another neighboring carbon atom [14][60, p. 3 ff].

sp^2 configuration (C=C) occurs when two of the three available $2p$ orbitals are involved in the hybridization of the $2s$-orbital. The third p-orbital remains in its original state. The sp^2-hybridized carbon atoms can form covalent bonds with each other, which are then on the same level and form a trigonal structure. The hybrid orbitals are located in a plane with an angle of 120° to each other, which corresponds to the bonding of graphite. The fourth electron (in the uninvolved p-orbital) is in a π-orbital that is perpendicular to the σ bonding plane. This π-orbital forms a weaker π-bond with a π-orbital on one or more neighboring atoms [14][60, p. 3 ff].

The s-orbital hybridizes with only one of the three p-orbitals in the σ orbital (sp^1). The two π-orbitals are perpendicular to it. Two sp^1-hybridized carbon atoms can form a triple bond (C≡C) with each other.
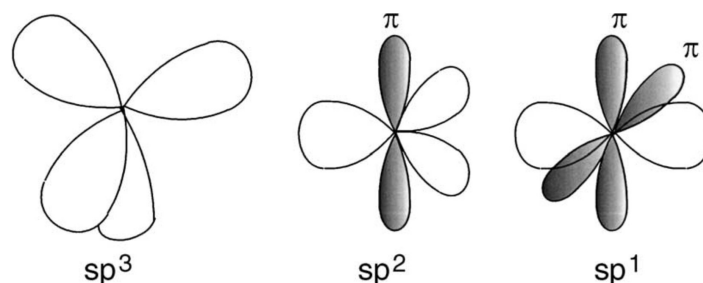
Fig. 13: The three carbon hybridized bonding sp^3, the sp^2 and sp^1. The figure is taken from [14].

Amorphous carbon layers offer an extreme variety of different disordered structures. On the one hand, the combination of the three different hybridization states sp^1, sp^2 (graphite-like) and sp^3 (diamond-like) and, on the other hand, the possible integration of hydrogen into

the carbon compound [14]. Fig. 14 shows the so-called ternary phase diagram of carbon by Jacob and Möller [61]. It is used to classify the different types of amorphous carbon layers depending on their sp^2/sp^3 ratio and hydrogen content. The hybridization states are also strongly dependent on the hydrogen content of the layer; the H content can be between less than 10% and 60% [14, 19, 20, 62].
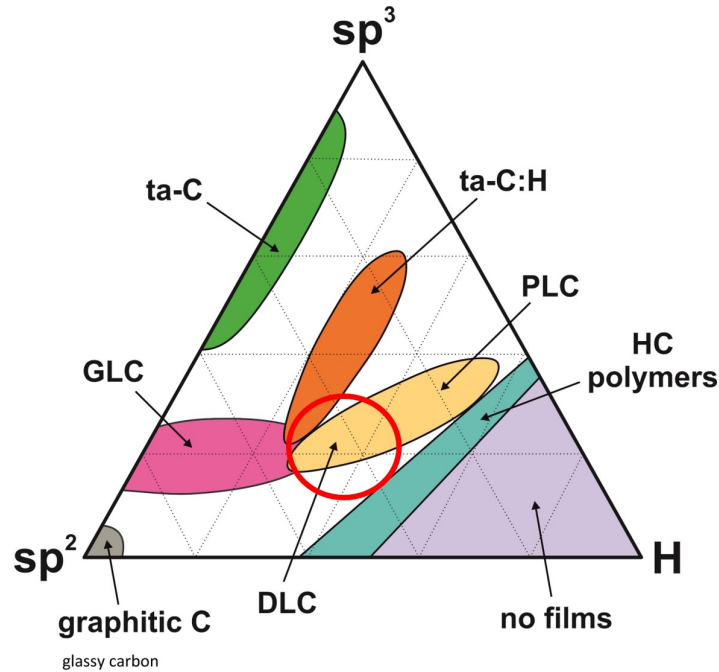
Fig. 14: Ternary phase diagram of bonding in a-C:H. The different categories of carbon layers, classified on their sp^2, sp^3 and hydrogen content is shown. a-C:H is highlighted by a red circle. The figure is based on [19].

The chemical composition of the layer (sp^2, sp^3 and H content) fundamentally influences the properties of a layer. If the sp^3 bonds dominate, the layer has diamond-like properties and is hard, chemically inherent and has a high electrical resistance. If, on the other hand, the layer contains sp^2, the properties are similar to those of graphite, the layer is soft, more flexible and has a high conductivity. Layers with no or very low hydrogen content are also referred to as a-C layers (amorphous carbon, Fig. 14 gray area); if the sp^3 content is very high, they are referred to as ta-C (Fig. 14 green area). Diamond-like carbon layers (DLC, Fig. 14 red circle) are part of the hydrogenated carbon layers (a-C:H) [14, 19]. The hydrogen content passivates the dangling bonds of the amorphous structures, thereby influencing the density, hardness and electrical and optical properties of the layer. The stress in the layer is also influenced by the hydrogen, as the residual stress decreases with an increasing number of C-H bonds [20, 62, 63]. A reduction in the H content leads to a higher structural disorder; if it is still a layer with a high density, these layers are mechanically highly stressable [17, 64, 63]. The main layer types from Fig. 14 are described below, the list follows a descending sp^3 content.

Tetrahedral amorphous carbon layers (ta-C, green) whose sp^3 content is up to 90%. sp^2 bonds are impurities for the sp^3 network. Due to the strong covalent bonds between the sp^3-hybridized carbon atoms, they usually have a high hardness between 60 GPa and 80 GPa. At the same time, these layers have a high density in the range of approx. 3.0 g/cm^3 [14, 19,

20][60, p. 8 ff][65, 66]. The hydrogenated counterpart is tetrahedral amorphous hydrogenated carbon (ta-C:H, orange). The H content makes the layer softer (approx. 50 GPa) and the density decreases to 2.4 g/cm^3 [14, 19, 20][60, p. 5 ff][66]. The a-C:H layers form one of the most hydrogen-containing layers (a-C:H, red circle) and range from polymer-like carbon layers (PLC, in the upper part) to diamond-like layers (DLC, in the lower part). The fraction for sp^3 bonds is between $30 - 60\%$ The hydrogen fraction is between 25% and 55%. This generally leads to a soft layer, whereby the hardness is below 10 GPa with a low sp^3 content and $10 - 20$ GPa with a higher sp^3 content. The density varies between $1.6 - 2.2$ g/cm^3 for low sp^3 and between $1.2 - 1.6$ g/cm^3 [14, 19, 20][60, p. 5 ff][66]. Graphitic carbon (C=C, gray) has the largest proportion of sp^2 bonds and has little to no sp^3 or H bonds. The sixfold rings are layered on planes. The bonds between the layers are weak. Open rings, distorted bond angles and possibly adherent sp^3 bonds are examples of impurities in the layer. Due to the high C content, their density is $1.2 - 1.6$ g/cm^3 with a hardness of $20 - 30$ GPa. The graphite-like carbon layers (GLC, magenta) represent the hydrogenated form with a density of 2.2 g/cm^3 and an hardness of 5 GPa [14, 19, 20][60, p. 10 ff][66]. Hydrocarbon polymers (HC polymers, light blue) form the layers with the highest hydrogen content, while the sp^2 and sp^3 content is relatively low. This results in amorphous chains of carbon and hydrogen atoms that are connected to each other and are very unstable due to the low content of C-C bonds. At a hydrogen content of more than about 65% no layer is formed [14, 19][60, p. 56 ff].
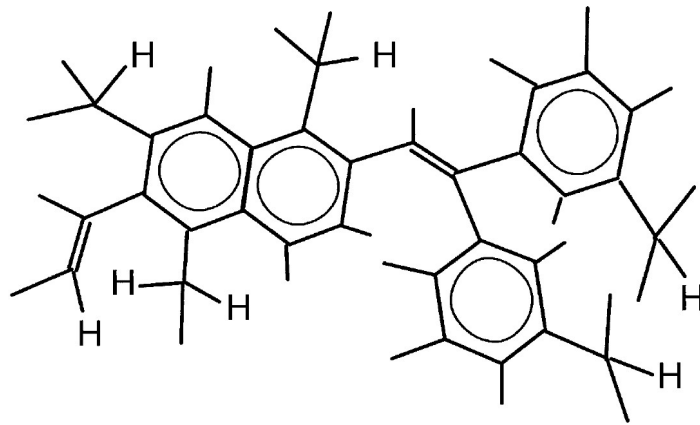
Fig. 15: a-C:H network according to the cluster model. sp^2 clusters are embedded in a sp^3 matrix consisting of C-C and C-H bonds. The figure is taken from [14, 65].

Since only a-C:H layers are used in this work, the structure is illustrated here using the cluster model. In Fig. 15 such a model is shown schematically. The structure consists of a graphitic cluster made up of sp^2-bonded carbon in the form of sixfold rings. These are arranged in planes and embedded in a matrix of sp^3-bonded carbon. The sp^2 clusters are restricted to single six-fold rings and short chains of sp^2 sites [14, 17, 19, 65, 67]. The composition of the cluster model clearly shows that the distribution of the sp^2 fraction and the organization of the sp^3 matrix influence the layer properties [68]. A short- to medium-range order in the order of approx. 1 nm is predominantly recognizable [19, 65].

5.2. Physical aspects of the a-C:H deposition mechanism

The formation of sp^3 bonds is a key property for a-C:H layers, so the growth mechanism is described in more detail by the so-called subplantation process. However, only high-energy C^+ and H^+ ions with $10 - 1000 \, eV$ are involved in this process, as low-energy ions ($< 10 \, eV$) do not have enough energy to penetrate the surface. Low-energy C^+ ions adhere to the topmost layer, where they either form sp^2 bonds or are reflected back into the plasma, depending on the adhesion coefficient. Passivation allows low-energy H^+ ions to adhere to dangling surface bonds. High-energy C^+ and H^+ ions on the other side can penetrate directly into the subsurface sites, losing their energy through elastic collisions with the target atoms (core stop) [14, 19, 66, 69]. The higher the ion energy, the deeper they can penetrate into the surface [69].
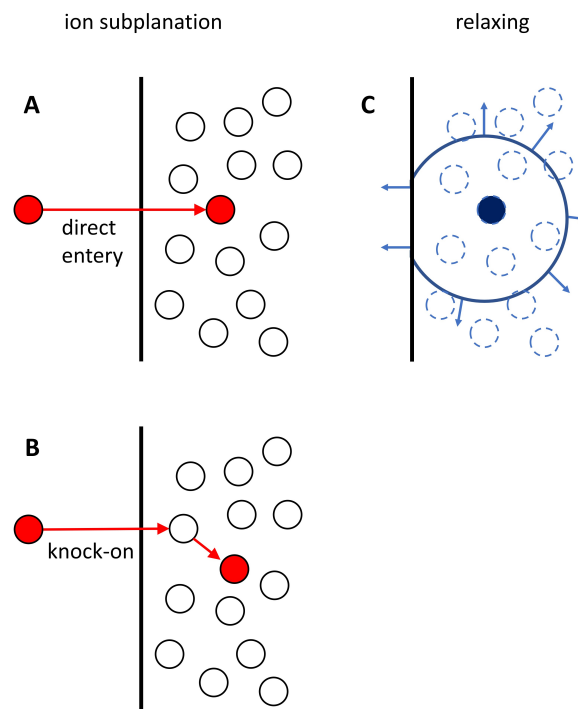
Fig. 16: Schematic sketch of the subplantation processes that occur during growth of the a-C layer by energetic ions. **A** shows direct penetration and **B** knock-on of surface atoms. **C** shows the relaxation of the densified region. The figure is based on ref [14].

The two different ways in which a subplantation process takes place are shown in Fig. 16. These processes are referred to as direct penetration and bumping. During direct penetration (Fig. 16A), ions can penetrate directly through the surfaces into the near-surface material. During collision (Fig. 16B), the ions transfer their energy to a collision partner in the area near the surface, which in use penetrates deeper into the layer and contributes to an increase in density below the surface. The energy released by the ions is used to integrate the ion itself into the layer, which occurs through the emission of phonons in the lattice (thermal dissipation). Alternatively, the energy loss is achieved by converting it into thermal energy. The volume into which this thermal energy is introduced is very small. This is called thermal spiking. This local heating leads to thermal diffusion, which spreads out in a spherical shape

(Fig. 16C). In this relaxation process, the energy is dissipated as phonons (heat production) and the energy is distributed to all atoms within the volume [14, 19].
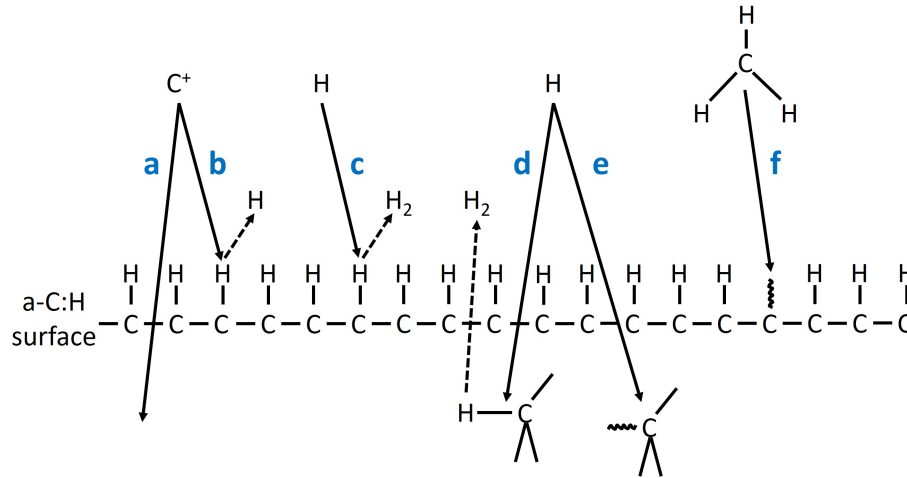
Fig. 17: Deposition processes for the growth of an a-C:H layer: **a** ion subplantation processes, **b** generation of dangling surface bonds by ion collisions, **c** generation of dangling surface bonds by abstraction of hydrogen atoms, **d** hydrogen abstraction from the subsurface, **e** passivation of free dangling bonds in the subsurface by hydrogen and **f** passivation of dangling bonds by hydrocarbons. The figure is based on refs [14, 66].

Ion subplantation is also shown schematically in Fig. 17a. It can be seen that other a-C:H growth mechanisms are known and take place. For example, carbon ions can abstract and form free dangling bonds after hitting the surface (Fig. 17b) instead of subplantating. Free dangling bonds can also form when hydrogen atoms (Fig. 17c) react with hydrogen bound in the layer and form molecular hydrogen. Hydrogen ions can also penetrate the surface and reach the subsurface. On the one hand, they can be desorbed and abstract other hydrogen atoms, creating free dangling bonds (Fig. 17d) - the resulting H_2 molecule then leaves the layer again. On the other hand, penetrating hydrogen atoms can passivate free dangling bonds (Fig. 17e). Since hydrocarbons such as CH and CH_3 are too large to penetrate the surface, dangling bonds can be passivated by attachment of these species (Fig. 17f). The attachment leads to the formation of sp^2 states [14, 66].

5.3. Experimental details of the coating process

a-C:H layers can be deposited using different methods, which can be divided into two main categories. The first is physical vapor deposition (PVD) and the second is chemical vapor deposition (CVD). There are a variety of PVD methods in which a process converts a solid starting material into a vapor phase and then condenses it back into a solid phase. Examples of PVD processes include electron beam evaporation, arc evaporation, sputtering and pulsed laser deposition. These processes are usually used to apply a-C layers [14, 70, 71]. In the CVD process, on the other hand, chemical reactions of gaseous reactants take place on a substrate surface. In the CVD method, the molecules of the reactant gas are dissociated by applying external heat [72]. Radio-frequency plasma-enhanced chemical vapor deposition (RF-PECVD) is a special form in which the gases are excited by a high-frequency field in a high-vacuum chamber. This deposition method was used in this work. An HF-driven

COPRA DN 400 (CCR GmbH, Troisdorf, Germany) was used as the plasma source. The COPRA is an inductively coupled HF discharge (13.6 MHz) with a single winding and a superimposed static transverse magnetic field. The transverse magnetic field generates two circularly polarized waves, one of which is resonantly coupled with the plasma. This results in a high absorption of RF energy and highly ionized plasmas with a density of about 10^{13} cm^{-3} and at the same time a low working temperature [37, 73, 74]. The working group [15, 16, 24] and others [14, 74] have shown that the process temperature is always below $40°C$. This means that temperature-sensitive polymer substrates can also be treated.
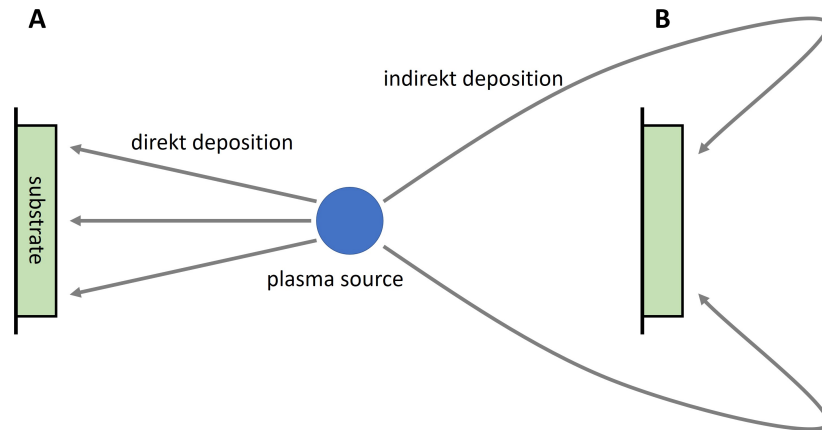
Fig. 18: Schematic illustration of the two different deposition processes. In **A**, the substrate surface points directly ($0°$) to the plasma source, which generates sp^3 rich layers. In **B**, the substrate surface faces away from the plasma source by $180°$. The layer deposited in this way is sp^2 rich.

Preliminary studies from the research group [15, 16, 21, 22, 24] as well as other research groups [19, 20] have shown that there are two different types of a-C:H layers, which are shown in Fig. 18. In Fig. 18A the direct coating is displayed, the substrate is at an angle of $0°$ relative to the sample. A large number of high-energy ion species hit the substrate surface and are subplanarized. The subplantation processes that take place lead to a higher degree of cross-linked sp^3 hybridization and thus to a harder (more robust) coating [19, 20]. In the literature, this is also referred to as r-type deposition [15, 16]. In the indirect deposition process (18B), the substrate surface faces away from the plasma source and is offset from the plasma source by $180°$. As the component of the particle momentum parallel to this surface is increased, increased diffusion processes take place on the substrate surface. The impinging particles therefore only reach the surface indirectly and consist of more radical and neutral species than energetic ions [15, 66, 69]. This showed that the geometry of the coating is a decisive factor for the chemical composition, in particular the sp^2/sp^3 ratio of the a-C:H layer. These different processes were utilized to develop an angle-dependent coating. The sp^2/sp^3 ratio of a thin a-C:H layer is controlled by varying the coating angle. This results in a customized coating. The chosen coating angles were $0°$, $30°$, $60°$, $120°$, $150°$ and $180°$. Fig. 19 shows the experimental setup that is used.
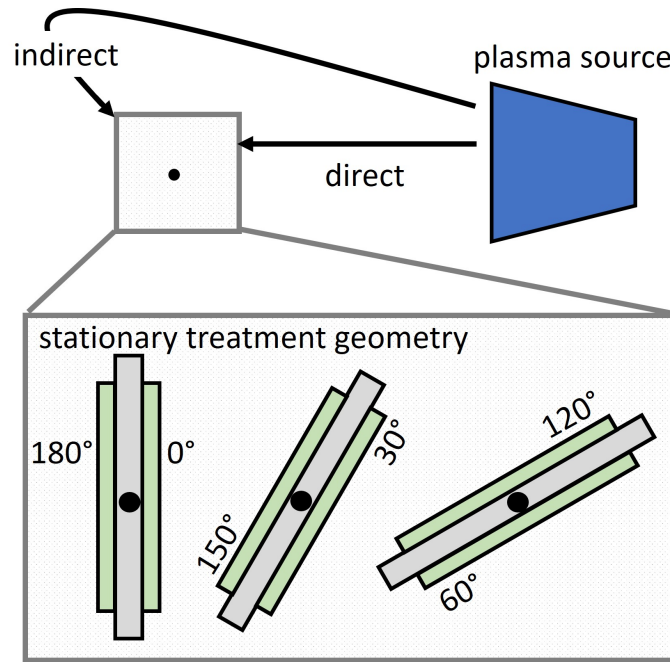
Fig. 19: Schematic representation of the angle-dependent coating process used in this work. The substrate was positioned between 0 and 180° in 30° steps in front of the plasma source in order to analyze the angle-dependent deposition mechanism. The center of the samples marked with a black dot is the pivot point. The distance between the pivot point and the plasma source was 275 mm. The figure is based on [75].

The two different substrate foils (PLA/PHB) cut into 10×5 cm (described in chapter 4) were clamped in self-made aluminum sample holders. These were attached to a self-made device at angles from 0° to 180° in 30° steps in front of the source. The distance of the pivot point of the samples was always 275 mm away from the plasma source. As no significant change in the surface could be observed at a treatment angle of 90°, this is not considered further below. The angle-dependent deposition process takes place in two steps. First, the surfaces were pretreated with an oxygen plasma at the corresponding coating angle (O_2 purity: 6.0). The 10 minute pretreatment took place at a pressure of 1 Pa with an O_2 flow rate of 60 $sccm/min$ at a power of 200 W. This process was initially considered only as surface cleaning and activation, but in this work it was revealed in more detail and found that changes also occur in the permeability of the polymers. The substrates were then coated with a-C:H in a second plasma process. Acetylene (C_2H_2) with a purity of 2.6 (containing acetone as solvent) was used as precursor gas as carbon and hydrogen source. The coating process took place at a pressure of 0.65 Pa with a C_2H_2 flow rate of 60 $sccm/min$ at a power of 107 W. Different layer thicknesses were achieved by varying the coating time. The carbon plasma deposition rate by direct coating is ~ 10 nm/min; that for the indirect coatings is ~ 2 nm/min. The respective deposition times of 2.5, 5.0, 7.5 and 10.0 min resulted in corresponding a-C:H thicknesses of 25, 50, 75 and 100 nm for direkt coating (0°). The obtained depositions were verified by measuring a film edge on a semi-coated silicon wafer with a profilometer (Veeco Instruments Inc., Dektak3 surface profile measurement system, Plainview, NY, USA). A silicon wafer (111, Silicon Materials, Kaufering, Germany), which was partially covered with vacuum-suitable and residue-free removable Kapton tape (Hi-Temp Masking Tape, Elegoo Inc., China), was applied and coated together with the polymers on the aluminum holder. As silicon is a hard

material that does not form an intermediate layer, it serves as a reference for the applied layers. The coating thickness can be determined on the basis of the resulting coating edge.

5.4. a-C:H coatings on plastic materials

The deposition process of an a-C:H layer onto a polymer surface using RF-PECVD offers three different possibilities how the a-C:H layer interacts with the polymer. The possible interactions are shown in Fig. 20. Depending on the deposition process and the specific polymer, the mechanisms can be different [15]. The simplest case is the direct deposition of the a-C:H onto the surface of the polymer without further interaction, which is shown in Fig. 20A. The layer simply adheres to the polymer surface and does not form a direct bond. This makes it easy to remove [15]. An example of this is polyoxymethylene, where the bond between the a-C:H layer and the polymer is only weak [76]. In the second case (Fig. 20B), not only deposition but also erosion processes take place on the surface of the polymer. On the one hand, the impinging plasma species deposit a layer on the substrate surface, but on the other hand they also continuously erode both the substrate material as well as the deposited layer. The deposited coating therefore consists of a thin layer that is mainly composed of its own carbonization products [15]. In the last possible process in Fig. 20C, it is assumed that an intermediate layer region forms between the substrate material and a-C:H. This mixing phase leads to a stable combination of both materials through a gradual density rearrangement from the polymer substrate to the a-C:H layer. This means that the interlayer region increases until the pure a-C:H layer starts. The intermediate layer is complete when no further surface material of the polymer can be removed and can no longer be achieved by impinging. The dominant material detectable on the surface changes from the polymer substrate to the a-C:H layer and is dependent on the layer thickness. Overall, this process leads to a lower thickness of the pure a-C:H layer [15].
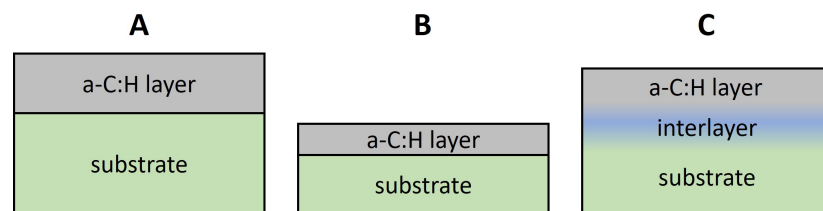
Fig. 20: Illustration of the three possible interactions between a general polymer substrate and the plasma-based a-C:H deposition: **A** shows the direct deposition of the a-C:H layer on the polymer, **B** shows the erosion of the polymer and the a-C:H layer during deposition, and **C** shows the formation of an interlayer between the polymer and the a-C:H layer. The figure is based on [15].

For the substrate polymers PLA and PHB used in this work and presented in chapter 4, it has already been established that interlayer formation is proven. For PLA, an intermediate layer with a thickness of $\sim 40\ nm$ could be determined in the RF-PECVD process used here. A slightly smaller interlayer of $\sim 20\ nm$ was determined for the PHB film [28].

6. Experimental techniques

In the following chapter, the measurement methods used in this work to investigate the properties of the coatings produced are presented in detail. A goniometer was used to specify the wettability of the coated and uncoated surfaces of the samples. This also allowed conclusions to be drawn about the surface free energy and the contact angle hysteresis. To obtain information about the permeability of the coating, the water vapor transmission rate was measured. To analyze the molecular composition of the samples, the surface was examined using infrared spectroscopy and X-ray absorption spectroscopy such as X-ray near-edge absorption spectroscopy and X-ray photoelectron spectroscopy.

6.1. Contact angle (CA)

The interphase between a liquid and a solid forms an angle between the liquid surface and the contour of the contact surface; this is referred to as the contact angle (CA) θ [77]. For surfaces the CA is measured from a drop of a suitable liquid resting on a surface; Fig. 21 illustrates the measuring method schematically. This is measured on a macroscopic level and the average wettability of the surface is characterized. The capillary effect, roughness and baseline are decisive factors here. On a microscopic level, contact angles examine the interaction of the microscopic area at the contact line [78, 79, 80]. This provides information on the interaction between the substances and therefore on the wettability, surface energy/properties and surface topographies of a sample. The surface free energy is determined by chemical bonds on the surface. For example, different hybridization states of the carbon on the surface are decisive [14, 81, 82, 83, 84, 85, 86].
The measurements were carried out with a OCA 15EC goniometer (DataPhysics Instruments GmbH, Filderstadt, Germany).
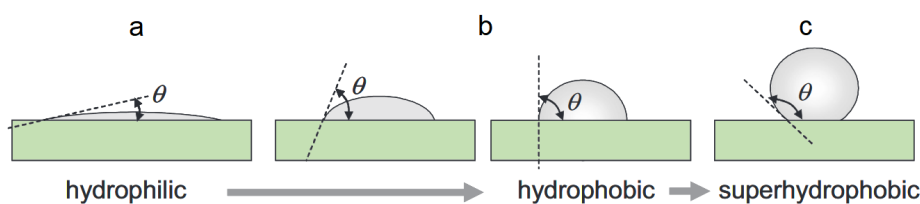
Fig. 21: Schematic of different levels of wettability on surfaces. **a** shows a hydrophilic, **b** two different hydrophobic and **c** a superhydrophobic surface. The figure is taken from [87, p. 471–473].

If the liquid is very strongly attracted to the solid surface, as for example, water on a hydrophilic solid, the droplet will completely spread out on the solid surface and the CA will be close to zero degrees, shown in Fig. 21a. Less strongly hydrophilic solids will have a CA up to 90°. If the solid surface is more hydrophobic, the CA will be larger than 90° (Fig. 21b). Surfaces with a CA greater than 120° are called superhydrophobic Fig. 21c. On these surfaces, water droplets simply rest on the surface, without actually wetting to any significant extent. The CA thus directly provides information on the interaction energy between the surface and the liquid [79, 84]. Using the simplified planar geometry of Young-Dupré equation can be written as:

$$0 = \gamma_{SV} - \gamma_{SL} - \gamma_{LV} \cdot cos(\Theta) \tag{16}$$

With γ_{SV} as the solid/vapour surface tension; γ_{SL} as the solid/liquid surface tension; γ_{LV} as the liquid/vapour surface tension; Θ as the CA [77, 78, 88]. The relationship between the variables in Eq. 16 is illustrated in Fig. 22 for visualization.
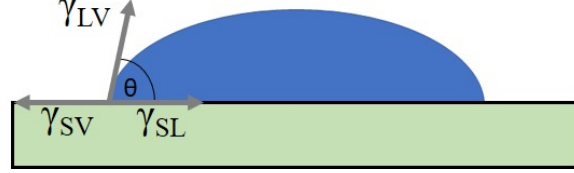
Fig. 22: CA Θ of a drop of liquid deposited on a solid sample. The tensions of solid/vapour γ_{SV}, solid/liquid γ_{SL} and liquid/vapour γ_{LV} are shown. The figure is based on [88].

Later, Young eliminated the vapor interactions from the equation, resulting in Eq. 17

$$0 = \gamma_S - \gamma_{SL} - \gamma_L \cdot cos(\Theta) \tag{17}$$

With γ_S is the solid surface free energy (SFE) and γ_L the SFE of a measuring liquid.

6.1.1. Surface free energy (SFE)

As there is no known method for direct determination of the SFE, it is determined indirectly. This is done by observing the interaction of different solvents and their interaction with the surface. As a basis, the interfacial tension γ_{SL} (Eq. 17) was first calculated by Good-Girifalco and then by Fowkes using the two surface tensions γ_S and γ_L and the corresponding interactions between the phases. The interactions were described as the geometric mean of a disperse component γ_S^d and γ_L^d of the surface tension. Φ_{ik} was added as a dimensionless function of the thermodynamic state of the system (between 0 and 1). The dispersive interaction temporarily leads to asymmetrical charge distributions (Van der Waals interactions). Polar corrections were estimated by Fowkes, but no systematic method for their treatment or determination has been proposed [89, 90, 91, 92]. This results finally in:

$$\gamma_{SL} = \gamma_S + \gamma_L - 2 \cdot \Phi_{ik} \sqrt{\gamma_S^d + \gamma_L^d} \tag{18}$$

Owens and Wendt modified Fowke's Eq. 18 and assumed that polar interactions γ_L^p and γ_S^p are considered connected [91, 93]. This results in the following equation:

$$\gamma_{SL} = \gamma_S + \gamma_L - 2 \cdot \sqrt{\gamma_S^d + \gamma_L^d} - 2 \cdot \sqrt{\gamma_S^p + \gamma_L^p} \tag{19}$$

The combination of Eq. 17 with Eq. 19 results in the following relation:

$$\sqrt{\gamma_S^d + \gamma_L^d} + \sqrt{\gamma_S^p + \gamma_L^p} = 0,5 \cdot \gamma_L(1 + cos\Theta) \tag{20}$$

As γ_S^d and γ_l^p are unknown, the contact angle of at least two different measuring liquids must be measured. It is important that one liquid has a high electronegativity difference

around the polar component (e.g. HPLC water) and one with a predominantly non-polar component (e.g. diiodomethane). This results in two equations in the form of Eq. 19 with different values for the constant coefficients. The result is two linear systems of equations:

$$x + ay = b(1 + cos\Theta_1)$$

(21)

$$x + cy = d(1 + cos\Theta_2)$$

With $x = (\gamma_S^d)^{0.5}$ and $y = (\gamma_S^p)^{0.5}$; Θ_1 and Θ_2 as CA of the two different liquids and $a - d$ as coefficients dependent on these liquids [92]. Kaelble and Rabel took this as an opportunity to divide a variety of substances into their polar and dispersive components [94, 95]. This is the name given to the standard method for calculating the surface free energy of a solid from the contact angle with several liquids according to Owens, Wendt, Rabel and Kaelble (OWRK).

Because SFE is based on CA analysis, the above-mentioned influences such as morphology also play a decisive role. Chemical bonds and hybridization states are also of decisive importance. An sp^3-terminated surface has a high SFE due to its strong covalent character. A strong polarity leads to lower contact angles and increased hydrophilicity. In comparison, the SFE of an sp^2-terminated surface is lower due to the weak polarity of the dangling bonds. Therefore, an sp^2-rich surface has a higher contact angle than an sp^3-rich surface [14, 80, 82, 86, 96]. If free dangling bonds on the surface are saturated with hydrogen - $C-H$ bonds are formed, a polar interaction between the sample surface and the water is reduced - the surface becomes hydrophobic [83, 84, 85]. The formation of functional oxygen groups on the surface leads to more polar bonds and thus to an increased attraction for polar solvents, e.g. water - the surface becomes hydrophilic [81, 97].

Table 1: The polar γ_p and disperse γ_d components of the five liquids used in this work: water, ethylene glycerol, formamide, 1-bromonaphthalene and diiodomethane. Sorted by decreasing polar fraction.

	water [mN/m]	ethylene glycerol [mN/m]	formamide [mN/m]	diiodomethane [mN/m]	1-bromon-aphthalene [mN/m]
γ_p	47	21	29	3	0
γ_d	26	26	28	47	44

6.1.2. Contact angle hysteresis (CAH)

The static CA (section 6.1) describes the state at equilibrium, i.e. at rest. In addition to the static CA, a dynamic CA can also be determined. In a dynamic CA measurement, the droplet repeatedly wets an dewetted surface with the liquid front. This is called advancing CA (ACA). The ACA provides information about the fluid mechanics on a freshly wetted surface, i.e. about the dry-wetting behavior of a liquid or a surface. The droplet can also be removed from the wetted surface, i.e. the surface is dewetted. Dewetting when the droplet shrinks is referred to as receding CA (RCA). This provides information about the adhesive forces between the liquid and the surface. The difference between the ACA and the RCA is referred to as CA hysteresis (CAH).

$$CAH = \Theta_{ACA} - \Theta_{RCA} \tag{22}$$

The CAH is a measure of the mobility of a droplet on the surface and a means of evaluating the macroscopic method roughness of the sample [80, 98, 99]. There are two common methods for wetting and removal.
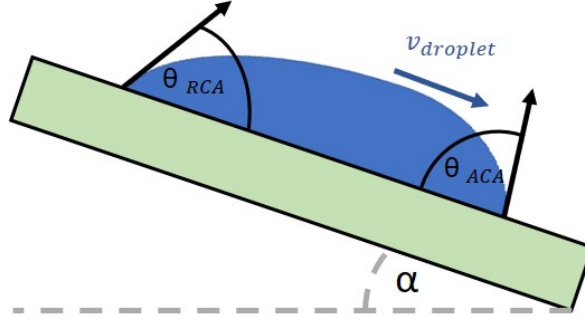
Fig. 23: ACA and RCA of a droplet running off on a tilting surface. The figure is based on [100].

On the one hand, a drop of water can start to roll off hydrophobic surfaces by tilting the sample. The surface is tilted until the angle α is at the stability limit and the drop just starts to move, which is shown schematically in Fig. 23. Just at this moment, the ACA and the RCA can be measured and results in Eq. 23 [100, 101]:

$$sin\alpha = C \cdot \gamma \left(cos(\Theta_{RCA}) - cos(\Theta_{ACA})\right) \tag{23}$$

With γ as the SFE of the liquid and C as a multifactorial constant that takes into account the liquid density drop shape and gravity [100].

On the other hand, the method of increasing and decreasing the volume of a droplet so that the ACA and RCA can be accommodated. Fig. 24 illustrates this principle. For this purpose, a static drop is placed on the surface (Fig. 24a) and is enlarged by filling up the water volume (Fig. 24b). Initially, the contact line of the droplet with the surface (this is called the baseline) remains constant until the surface tension is overcome and the baseline increases (Fig. 24c). As the baseline expands, the ACA can be measured, which remains stable. The situation is similar when receding. Initially, the baseline remains the same as the volume decreases (Fig. 24d), until the adhesion forces of the surface are no longer sufficient and the baseline is reduced (Fig. 24e). the RCA can be measured, which also remains stable. This process can be repeated several times [102].
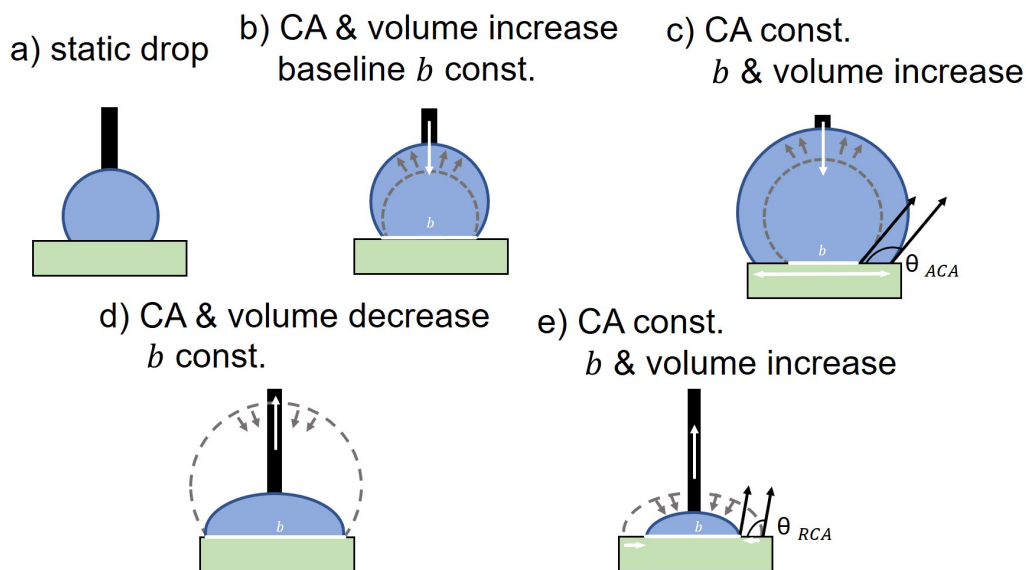
Fig. 24: Model ACA and RCA measurement by variable drop volume. **a** small static drop is deposited on a surface with needle in. **b** Liquid is pumped into the drop and volume increases while the baseline b (white line) is constant. **c** The volume increasing, the CA is stable and the baseline starts to advance - the CA is the ACA. **d** Liquid is resumed of the drop and volume decreases, while the baseline is constant. The CA decreases - it is not the RCA. **e** the volume of the drop and the baseline decrease and the CA stays constant - the RCA is reached. The figure is based on [102].

This method was mainly used in the present work. The static output drop was 1 μl HPLC water. The volume was then increased by 5.0 μl with 0.2 $\mu l/s$ and reduced by 4.5 μl after 1 s with 0.1 $\mu l/s$. Since the drop volume is subject to an evaporation process at room temperature, leaving 0.5 μl at each cycle ensured that the needle was in the drop. The receding speed was reduced because the baseline change at the RCA and the volume interval used changes at 4.0 μl. An increase in the drop volume was not possible with the analyzed image section.

6.2. Water vapor transmission rate (WVTR)

The water vapour transmission measurement is a gravimetric method and by definition describes the penetration of water vapour through a volume with a standardized area of one m^2 over a period of 24 h under defined test conditions. Fig. 25 shows the schematic setup of such a measurement. The sample holder is a dish filled with HPLC water and the sample is pressed against it by means of seals and a screw ring. This means that the inside of the dish - called the wet chamber or absorption chamber - is sealed off from the test chamber by the clamped sample. When the system is heated, the humidity in the absorption chamber begins to rise and transports through the test surface/volume into the test chamber. The test chamber is continuously monitored using a humidity sensor. At the same time, the weight of the tray is measured at regular intervals. The WVTR is determined by the difference in humidity and the difference in mass of the tray. I.e. the WVTR is not a material constant and always related to the thickness, the test surface, the density and the properties of the material and the surface [103, 104].
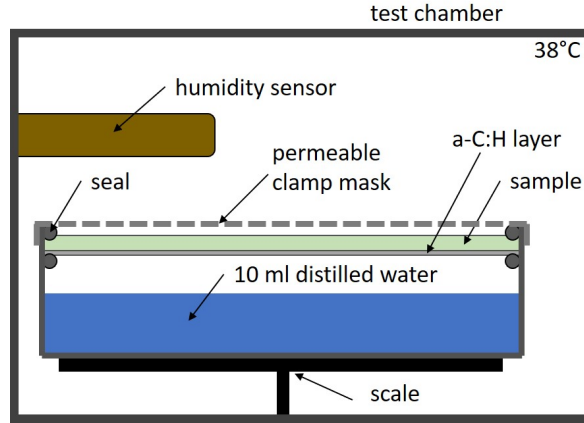
Fig. 25: Sketch representation of the measuring conditions for WVTR measurements. Shown is the test chamber with the moisture sensor, the scale and the tray with water sealed off by seals, a clamp mask and the sample. During the measurement, the treated and coated side faces the water.

The WVTR measurements were performed with a W3/031 Water Vapor Transmission Rate Tester from Labthink (Labthink GmbH, Neu-Isenburg, Germany). The measuring area of the sample is 4.91 cm^2, clamped in a customized adapter in a sealed test dish with 10 ml HPLC water, with treated sample surfaces facing the water reservoir. The test temperature is $38°C$ and a relative humidity difference of 90 $\%RH$ is created between the two sides of the sample.

The WVTR W of the coated samples is a combination of different WVTRs; on the one hand the permeability of the substrate W_s and on the other hand the applied a-C:H layer W_l. Assuming that the substrate and the coating are homogeneous, the WVTR is inversely proportional to the thickness $W = 1/d$ [103]. This means for the layer-system:

$$\frac{W_s}{W_l} = \frac{d_l}{d_s} \tag{24}$$

To obtain the total permeability, the reciprocal values of the WVTRs must be added together [103].

$$W_{ges} = \frac{W_s \cdot W_l}{W_s + W_l} \tag{25}$$

6.3. Scanning electron microscopy (SEM)

An SEM scans the surface of a sample with an electron beam and generates an image by observing different interactions between the beam and the sample. Fig. 26 shows the schematic representation of the lens and condenser system. The process takes place in a vacuum to minimize errors in the electron beam caused by foreign atoms. The electron beam is generated by a hot cathode, usually a tungsten heating element. The free electrons are accelerated towards the sample in an electric field in a so-called Wehnelt cylinder. The acceleration voltage is several kV. The beam is directed and focused with a lens system of magnetic or electrostatic coils in such a way that the sample is optimally hit. The coils are then used to guide the beam over the entire sample, which can then be scanned step by step. When the beam hits the sample, two different types of interaction occur between the electron beam and

the surface. On the one hand, the primary beam can be reflected by the surface and on the other hand, secondary electrons from the surface can be triggered. The secondary electrons are released from the upper layers of the sample and are of lower energy. The electrons are detected by detectors and a grayscale image of the surface topography is created [105, p. 24 ff.]

cathode

Wehnelt cylinder

anode

1st condensor lense

2nd condensor lense

objective lens
for imaging/screening

electron detector

sample
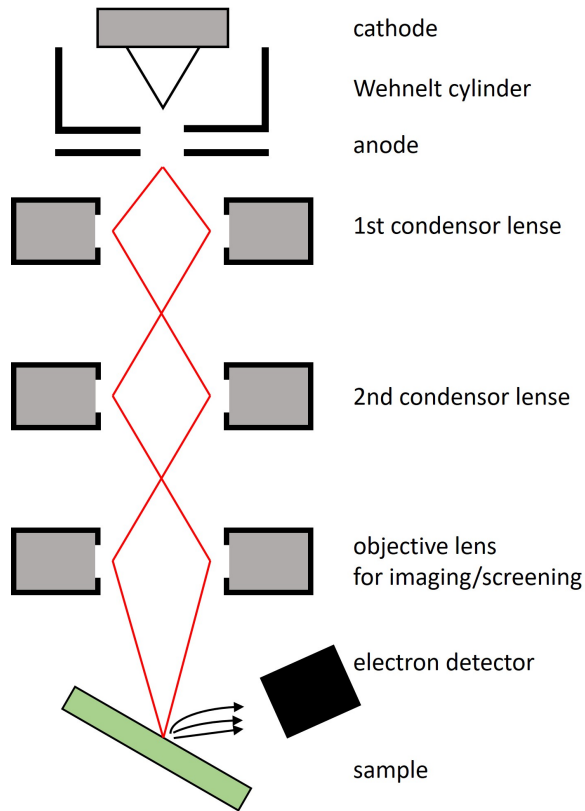
Fig. 26: Schematically sketch of the operating principles of a SEM. The figure is based on [105, p. 24 ff.].

For the morphological investigations in this work, an SEM515 device from the Phillips company at the Koblenz University of Applied Sciences, RheinAhrCampus Remagen, was used. The operating acceleration voltage was between $10 - 20 \, kV$ at an average distance of $20 \, mm$. Since non-conductive polymers are subject to the effects of charging by the electron beam in the SEM, the samples were previously coated with a conductive gold layer with a thickness of approximately $17 \, nm$. The low layer thickness ensures that the imaged surface can be assigned to the sample surface. The images can be used to collect macroscopic information about the surface. For example, whether there are manufacturing-related inclusions in the samples, whether a layer has been applied and whether it is detached, intact, wavy (so-called cord buckling) or cracked [106, 107].

6.4. Atomic force microscope (AFM)

Atomic force microscopy (AFM) is a method to investigate the topography of a sample surface. The material itself is irrelevant for the topography. It can be hard or soft, synthetic or natural (biological structures such as cells and biomolecules are included). Furthermore, it is independent of opacity or conductivity. The sample is imaged at ambient air and room

temperature. The typical resolution range of this measurement method is several microm-
eters vertically with subnanometer height resolution [108, p. 1 ff.]. The function is shown
schematically in Fig. 27.
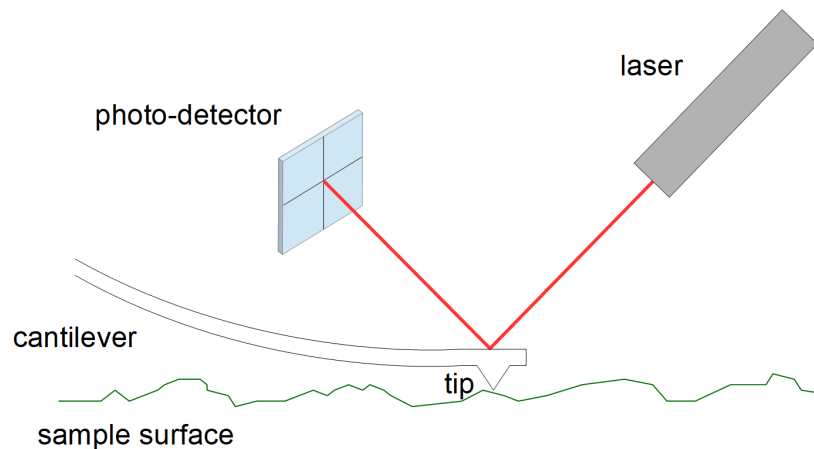
Fig. 27: Schematic illustration of the core components of the AFM: cantilever with the tip, laser with
the beam directed at the cantilever, photo detector.

The tip is attached to a flexible cantilever. This can be bent under the influence of force.
Consequently, the tip is mounted like a spring and can swing upwards freely. The laser
beam is reflected by the cantilever. The reflected beam is then measured with the aid of
a divided photo-diode acting as a detector. Displacements of the cantilever are detected
accordingly on the photo-diode vertical tip movement is identified by vertical displacement
of the laser point. If the laser point moves horizontally, the tip or cantilever is twisted by
lateral forces. The surface morphology can now be achieved by direct contact of the tip with
the surface or indirectly by feeling the surface forces [108, p. 5 ff.]. Controlled by piezoelectric
components, the cantilever and tip can be moved laterally over the sample surface in x- and
y-direction. Electrical potentials are applied and converted into mechanical movements by
electromechanical converters. This allows a lateral movement of the cantilever. Due to the
different height profiles, the cantilever bends up or down during such movements. During
the scanning process, the height shift (z-displacement) is compensated by a feedback system,
whereby the contact force of the tip on the surface is kept constant [108, p. 93 ff.]. As already
described, the cantilever behaves like a spring, so its displacement Δx can be described by
the Hook's law with the normal force F_N [35, p. 103]:

$$F_N = D \cdot \Delta x \tag{26}$$

D is the spring constant. The vertical spring constants of cantilevers commonly in the range
of $10^{-2} \frac{N}{m}$ to $10^2 \frac{N}{m}$ respectively $\frac{nN}{nm}$ [108, p. 5]. Since the tip has to be close to the surface,
two phenomena can occur as a result of attraction forces. First, the tip jumps to the surface
or second the tip jumps off the surface. In order to prevent this, the contact force between
tip and substrate is recorded with software during the entire image acquisition process and
displayed in a force-distance curve [108, p. 106 ff.].
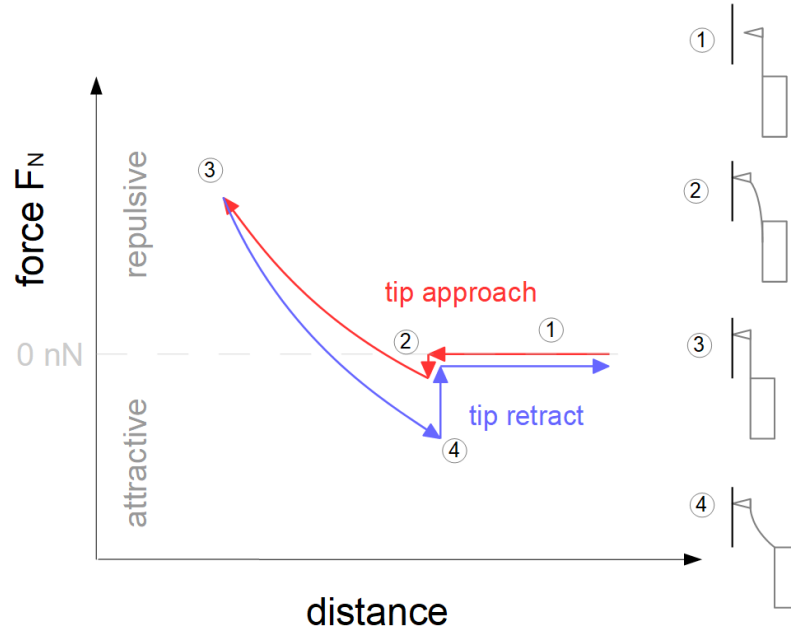
Fig. 28: Force-distance curve for AFM system: The interaction force when approaching the tip is represented by the red line. The blue line shows the retract of the tip. **1** shows the pull over, **2** shows the tip jumping towards the sample. **3** shows the maximum force increase and represents the turning point at which the tip is pulled out of the sample. **4** shows the tip retracting from the sample.

The force-distance curve shows the interaction force between tip and surface as a function of the distance. The tip is lowered onto the sample with a defined force and removed again. This allows conclusions to be drawn about different properties of the sample or surface area.

The approach phase is shown in red in Fig. 28 1. When the tip approaches the surface, it begins to feel an attractive force and the tip jumps to the surface (Fig. 28, 2). As soon as the tip is pressed further against the substrate, a repulsive force begins to interact. In Fig. 28 3, the maximum force is reached and the direction of movement changes. This retreat process is represented by the blue curve. By reversing the direction of movement of the tip, the interaction becomes attractive again and the tip jumps back from the sample surface at point 4 [108, p. 104-109].

The surface morphology in this work was investigated using an Asylum Research MFP-3D-BIO atomic force microscope (Oxford Instruments, Abingdon, UK). The measurement was performed in contact mode at ambient conditions. A height profile of an area of $5 \times 5\ \mu m^2$ was recorded with a resolution of 512 scan points. this corresponds to a pixel image size of $512 \times 512\ px$. The measurements were performed at a speed of $5\ \mu m/s$ with AC240TS cantilevers (Oxford Instruments, Abingdon, UK). The recorded images were analyzed, processed and plotted as a 3D representation using the software Gwyddion 2.58 (GNU General Public License). To smooth artifacts and suppress noise, filters with a mean, median and conservative noise reduction of 3 px each were applied. At least three different positions distributed over the sample were recorded. The roughness R_a and R_q were statistically determined from the height return (same parameter set as deflection return).

6.5. Infrared (IR) spectroscopy

The theoretical background of infrared spectroscopy and the measurement method are presented. IR spectroscopy belongs to the methods of molecular spectroscopy. It is based on resonant absorption of a photon by the molecule. The location and intensity of the absorption bands can therefore be clearly assigned to chemical groups. The good reproducibility indicates a high specificity with which the absorption maxima can be measured with the aid of the wave number transmission. These bands are particularly suitable for the identification of the substance. The bands are assigned to the basic structure of the molecule [109, p. 4].

6.5.1. Theoretical overview

The infrared radiation can have a wavelength λ from 800 nm to 50 μm. Molecules are compounds of several atoms. The atoms in the molecule are arranged at defined distances from each other. These distances make it possible for molecules to assume vibration and rotational states. Since in our case the molecules are not excited by the IR to rotate, the case is not described further. The distances of the atomic nuclei are determined by the sum of all forces. Through energy absorption, the atoms can be stimulated to oscillate around their equilibrium position. Like the energy of the electrons, the oscillation energy is also quantized, i. e. it can only assume certain values that can be described by quantum numbers. If a transition from one state of vibration to another occurs, very specific selection rules must be observed. These are defined as $\Delta E = E_1 - E_2$ according to the difference in energy consumption or release between the respective pathways (Fig. 29). This means that if a photon is to change a vibration state, its energy E_{Ph} must match the energy difference of the vibration states ΔE. This is called frequency condition [109, p. 13, 14][110, p. 690].

$$E = h\nu = \hbar\omega = \frac{hc}{\lambda} \tag{27}$$

With $\hbar$ as reduced Planck constant, h as Planck constant, c as the light speed, ω as angular frequency of photon and ν as the frequency of photon.

It is assumed that a bi-atomic molecule of masses m_1 and m_2 is present. In addition, the binding of the molecule is assumed to be an elastic spring. Close to the equilibrium position x_0 the potential can be approximated as parabola (Fig. 29). The deflection $x - x_0$ counteracts the harmonic force

$$F = -D(x - x_0) \tag{28}$$
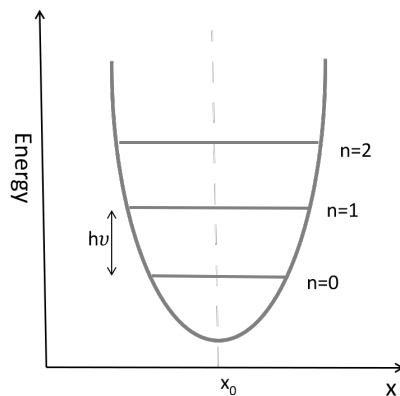
Fig. 29: Molecular energie. The horizontal lines represent the vibrational energie levels up to exemplary quantum numbers $n = 2$.

The acceleration of the masses m_1 and m_2 is done according to $m_i \ddot{x}_i = -D \; \Delta x$ [35, p. 103]. However, the center of gravity remains in r_0, instead of the masses the reduced mass $\mu = \frac{m_1 m_2}{m_1 + m_2}$ can be used.

$$\mu \ddot{x} = -D \Delta x \tag{29}$$

Results from the fact that the molecule oscillates with the angular frequency ω.

$$\omega = \sqrt{\frac{D}{\mu}} \tag{30}$$

This frequency also applies to quantum mechanics. If the harmonic oscillator is solved with the help of the Schrödinger equation, the required discrete energy levels are obtained.

$$E_n = \hbar \omega (n + \frac{1}{2}) \tag{31}$$

Whereby n is a quantum number and can assume the values $n = 0, 1, 2, 3, ...$ [109, p. 15 ff][110, p. 846].

6.5.2. Specular reflectance fourier transform infrared spectroscopy (SR-FTIR)

IR spectroscopy is used to determine molecules whose identification is based on a reference spectrum. The method of infrared spectroscopy used in this work is the specular reflectance fourier transform infrared spectroscopy (SR-FTIR). The measurements were carried out with an IRPrestige-21 and a specular reflectance unit (SRM 8000A). The SRM 8000A device contains the optical system described below, shown in Fig. 30.
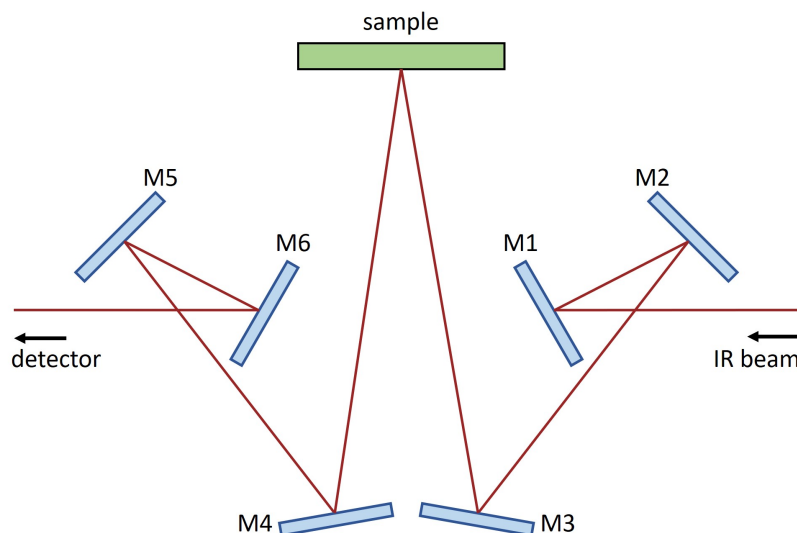
Fig. 30: Schematic representation of the beam path of the SRM 8000A module. The figure is based on[111].

The light reflected by the plane mirrors $M1$ and $M2$ is reflected by the spherical mirror $M3$ and hits the sample surface. The light beam has an average angle of incidence of $10°$ relative to the sample. The IR reflected from the sample is reflected by the spherical mirror $M4$ and the plane mirrors $M5$ and $M6$ onto the detector [111]. This means that the total radiant flux is divided into absorption, transmission and reflection. If the transmission value of the radiant flux Φ_T is used in relation to the total radiant flux Φ_0, the transmission τ is obtained by $\tau = \frac{\Phi_T}{\Phi_0}$. This is done with the absorbed and reflected part of the intensity and one gets the absorptance α and the reflectance ρ. If these are now inserted into each other, one obtains [35, p. 328 ff][109, p. 12][110, p. 573 ff]:

$$\alpha + \tau + \rho = 1 \tag{32}$$

In order to obtain the best possible information, it is therefore important to keep the level of reflected radiation as low as possible.
The hydrocarbons present in a-C:H layers consist of the alkynes ($3100 - 3300 \; cm^{-1}$), alkenes ($3150 - 3000 \; cm^{-1}$), alkanes ($3000 - 2750 \; cm^{-1}$) and aromatics ($3080 - 3030 \; cm^{-1}$) [109, p. 177-196]. The SR-FTIR measurements were performed under ambient air conditions at room temperature. In order to analyse the molecular composition of the samples, they are irradiated with electromagnetic radiation of the wavenumber $\tilde{\nu}$ from 500 to 4000 cm^{-1} (where applicable: $\tilde{\nu} = \frac{1}{\lambda} = \frac{\nu}{c_n}$, where c_n is the light speed in matter [35, p. 559]). The simple measurements were recorded with 100 repetitions. Whereas the detailed measurements were recorded with 300 repetitions in a range of 2800 to 3050 cm^{-1}. These detailed measurements are exactly in the range of the stretching area. The analysing tool for the spectra is a commercial IR-Solution-FTIR Control Software (Shimadzu IRsolution 1.30 from Shimadzu Corporation, Kyoto, Japan). The spectra were line corrected by multipoint baseline operations and get smoothed by parameter manipulation. These manipulations were used to highlight all relevant information. The penetration depth into the a-C:H layer is only a few nm. Since the measuring device is done under ambient conditions, the CO_2 peak of the measurements increases steadily.

In order to be able to analyse the spectra better, they were first corrected by multipoint baseline manipulations and refined by smoothing. These manipulation steps do not change the relevant information of the analysis, but highlight it for better analysis.

6.6. X-ray photoelectron spectroscopy (XPS)

X-ray photoelectron spectroscopy (XPS) is used to analyze the chemical states of the first atomic layers and assign them to atoms. To do this, the sample surface is bombarded with monochromatic soft X-rays with the energy $h\nu$. If the atoms are excited by the X-rays with the right energy, electrons are released and leave the solid into the vacuum, where they are described as free electrons. There they reach the electron detector, which records both the quantity and the kinetic energy E_{kin} of the electrons. A schematic sequence is shown in Fig. 31a. The Eq. 33 can be used to relate the binding energy E_{bind} and the kinetic energy to each other [112, 113].

$$h\nu = E_{kin} + E_{bind} + \Phi \tag{33}$$

With Φ as the spectrometer work function. As the binding energies are element-specific, the element and state in which they were bound can be deduced from the recorded spectra. The surface sensitivity results from the free path length that the electrons can travel without losing energy and is in the range of several nanometers. This results from the fact that even if electrons are released deep in atomic layers by the photons penetrating several micrometers into the material; they cannot reach the surface. This is because energy would be lost through interaction with the material as they pass through it [113][114, p. 9 ff.].
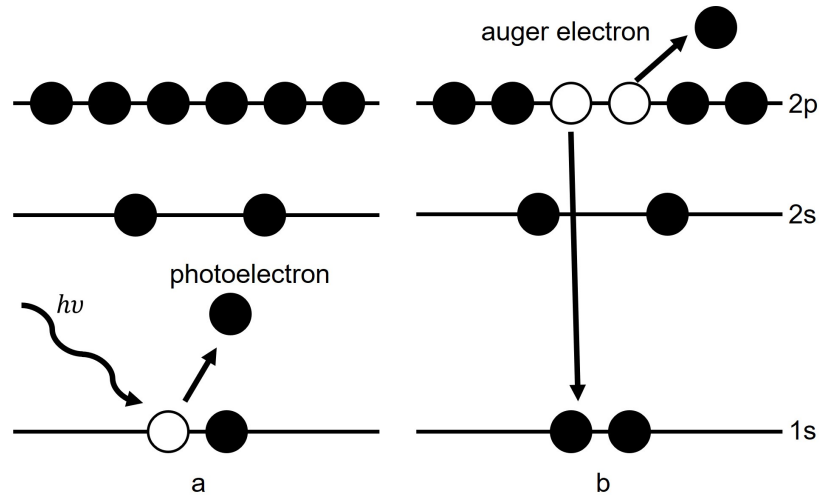
Fig. 31: a: The XPS emissin process for a model atom. An incoming photon cause the ejection of the photoelectron. **b**: The relaxation process for a model atom resulting in the emission of a 2p electron in 1s and he simultaneous emmitted auger electron. The figure is based on [114, p. 10].

However, it should be noted that differences in the chemical environment or the polarization of the components can lead to small fluctuations in the binding energies. These shifts can be used to determine the chemical state of the atoms under investigation. Similarly, with an offset of 10^{-15} s for each photoelectron released from the atom, a so-called Auger electron is

also released. An electron moves from an energetically higher level (e.g. 2p) to the now free position and transfers its energy in the form of kinetic energy to a previously neighboring electron. This electron then also leaves the atom (Fig. 33b) and the XPS detector measures the photoelectron, which is detected for the measurement, and an Auger electron, which has a lower energy. The sum of the kinetic energies of the emitted electrons cannot exceed the energy of the ionizing photons[112, 113][114, p. 9 ff.]. As a result, high intensities between $700-650\,eV$ were measured. Since the measurement accuracy depends directly on the monochromy of the incident wavelength of the radiation (Eq. 33), stable sources with a very narrow wavelength interval are required. Synchrotron radiation from an electron storage ring was therefore used for this work [112, 113][114, p. 9 ff.]. The XPS measurements were executed out at the HE-SGM beamline of the KIT at BESSY II in the Helmholtz-Zentrum Berlin für Materialien und Energie during the low alpha mode (ring current max. 100 mA, decay mode). The measurement system used is described in detail elsewhere [115]. Due to the charging effects of the poorly conducting polymer surface and the associated shift of the C1s peak, an e-gun was used for equalization. A complete survey spectrum of $600-0\,eV$ was recorded. The $C1s$ peak obtained (approx. $285\,eV$) was then analyzed and evaluated using the CasaXPS software (software version 2.3.18, Casa Software Ltd., United Kingdom). The evaluation was performed using the NIST database (https://srdata.nist.gov/xps/main search menu.aspx) and the work of other groups to determine the positions of the respective hybridization states [116, 117, 118] and the respective binding percentages were plotted in the OriginPro 8G software.

6.7. Near-edge X-ray absorption fine structure spectroscopy (NEXAFS)

Near-edge X-ray absorption fine structure spectroscopy (NEXAFS) is a technique that is performed near an ionization potential. In NEXAFS measurements, atoms are ionized by radiation that is varied over a certain energy range. The step size of the variation is usually not constant and is adapted to the element under investigation. Electrons close to the nucleus, the so-called K shell (hence the K absorption edge), can be brought into two states by the X-ray absorption process which is shown in Fig. 32 schematically. On the one hand into states below or into continuum states above the ionization threshold. Excitation of the core shell emits photoelectrons, which are a direct measure of the number of unoccupied electron positions generated in the core. To monitor the absorption cross-section, the photoelectrons are considered primary. However, if they remain below this level, the entire structural information is lost. They can only be detected when they are exceeded. If an electron from a higher shell falls into one of the generated core holes, fluorescent photons and Auger electrons are generated. This allows the annihilation or excitation of core holes to be monitored indirectly. Auger decay is faster for the K-shell excitations and therefore particularly suitable for elements with low Z, whereby the intense absorption edges of carbon, nitrogen and oxygen, for example, is in the soft X-ray range between 100 and 700 eV. L-shell excitations of elements with higher Z can also be investigated [119, 120]. A distinction can be made between two approaches to electron detection. On the one hand, all electrons can be measured, which is referred to as total electron yield (TEY). In another method, electrons with low kinetic energy are suppressed and thus only electrons from the area close to the surface are measured.

This is referred to as partial electron yield (PEY) [120, 121]. This is realized by applying a counter voltage in the range of the energy of the atoms to be measured. This means that not all electrons emitted from the material reach the sensor, but only those emitted close to the surface with sufficient energy [119]. Fluorescence analysis is particularly suitable for deeper layers, as the emitted fluorescence photons can penetrate the material over a greater distance [120, 121]. Since not only the binding energy but also the fluorescent photons and Auger electrons are detected, different types of molecular orbitals and binding states can be distinguished. Thus, specific bonding states (C−C, C=C, C−H, C=O) are investigated in this work.
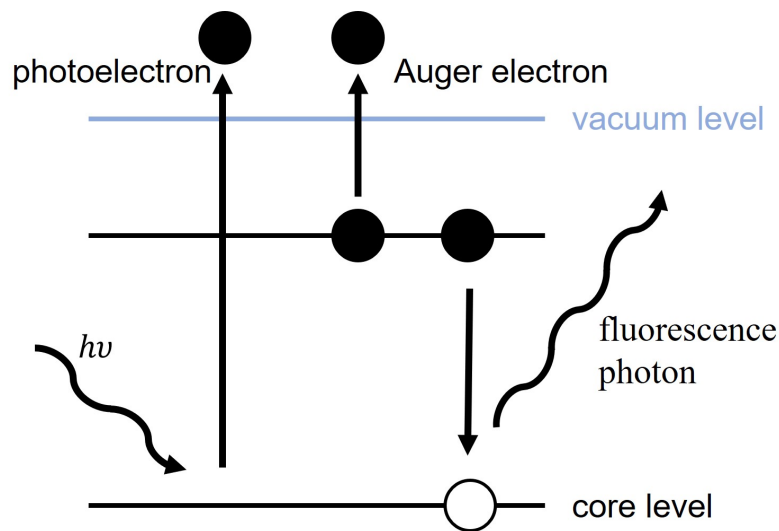
Fig. 32: Schematic representation of the basic principle of NEXAFS spectroscopy. X-ray absorption followed by the emission of a photoelectron The fluorescence decay process and the Auger decay process. The figure is based on [120].

Like the XPS method in section 6.6, the NEFAFS measurements were also performed at the beamline HE-SGM at BESSY II in Berlin using synchrotron radiation with partial electron yield (PEY) at a photon incidence angle of $55°$. The measurements were carried out with a maximum ring current of $100\ mA$ in decay mode and the O- and C-edges were measured. The O-edges were used to determine whether O-bonds were present on the surface, but were not evaluated further. The C-edge was recorded at two locations to ensure redundancy of measurements. The spectra were normalized, smoothed, synchronized with the ring current decay and the background noise was corrected. The adjustments were made with OriginPro 8.1G according to [119]. In order to detect and, if necessary, correct mirror artifacts and grid contamination, adjustments were made at the beginning of the measurement campaign using a gold edge. For the investigations, the peak positions were determined on the basis of the work of own and other groups [118, 122, 123, 124, 125, 126]. The analyzed peaks are shifted to the C=C π peak ($284.85\ eV$). other analyzed peaks are C−H at $286.40\ eV$, C=O at $287.3\ eV$, C−C at $288.35\ eV$ and C=C σ at $292.55\ eV$.

References

[1] R. L. Hirsch, R. Bezdek, and R. Wendling. Peaking of world oil production: Impacts, mitigation, and risk management.

[2] R. Auras, B. Harte, and S. Selke. An overview of polylactides as packaging materials. *Macromol. Biosci.*, 4(9):835–864, 2004.

[3] R. G. Sinclair. The case for polylactic acid as a commodity packaging plastic. *J. Macromol. Sci., Part A: Pure Appl.Chem.*, 33(5):585–597, 1996.

[4] A. L. Andrady and M. A. Neal. Applications and societal benefits of plastics. *Philos. Trans. R. Soc., B*, 364(1526):1977–1984, 2009.

[5] R. Andini, M. I. Sulaiman, Martunis, A. H. Umam, M. Olivia, and H. J. Endres. Biopolymer nanocomposites: their mechanical, thermal, and gas barrier properties for food packaging. *IOP Conf. Ser.: Earth Environ. Sci.*, 667(1):012067, 2021.

[6] G. Kale, T. Kijchavengkul, R. Auras, M. Rubino, S. E. Selke, and S. P. Singh. Compostability of bioplastic packaging materials: An overview. *Macromol. Biosci.*, 7(3):255–277, 2007.

[7] D.K.A. Barnes, F. Galgani, R. C. Thompson, and M. Barlaz. Accumulation and fragmentation of plastic debris in global environments. *Philos. Trans. R. Soc., B*, 364(1526):1985–1998, 2009.

[8] Q. Pan and Y. Sun. Changes in volatility leverage and spillover effects of crude oil futures markets affected by the 2022 Russia-Ukraine conflict. *Finance Research Letters*, 58(2):104442, 2023.

[9] J.W.C. Wong. *Current developments in biotechnology and bioengineering.* Elsevier, Amsterdam, Netherlands and Cambridge, MA, United States, 2017.

[10] A. Ruellan, A. Guinault, C. Sollogoub, G. Chollet, A. Ait-Mada, V. Ducruet, and S. Domenek. Industrial vegetable oil by-products increase the ductility of polylactide. *eXPRESS Polym. Lett.*, 9(12):1087–1103, 2015.

[11] L. T. Lim, R. Auras, and M. Rubino. Processing technologies for poly(lactic acid). *Prog. Polym. Sci.*, 33(8):820–852, 2008.

[12] R. Datta and M. Henry. Lactic acid: recent advances in products, processes and technologies - a review. *J. Appl. Chem. Biotechnol.*, 81(7):1119–1129, 2006.

[13] W. J. Feast, J. Tsibouklis, K. L. Pouwer, L. Groenendaal, and E. W. Meijer. Synthesis, processing and material properties of conjugated polymers. *Polymer*, 37(22):5017–5047, 1996.

[14] J. Robertson. Diamond-like amorphous carbon. *Mater. Sci. Eng., R*, 37(4-6):129–281, 2002.

[15] C. B. Fischer, M. Rohrbeck, S. Wehner, M. Richter, and D. Schmeißer. Interlayer formation of diamond-like carbon coatings on industrial polyethylene: Thickness dependent surface characterization by SEM, AFM and NEXAFS. *Appl. Surf. Sci.*, 271:381–389, 2013.

[16] M. Rohrbeck, S. Körsten, C. B. Fischer, S. Wehner, and B. Kessler. Diamond-like carbon coating of a pure bioplastic foil. *Thin Solid Films*, 545:558–563, 2013.

[17] P. Couderc and Y. Catherine. Structure and physical properties of plasma-grown amorphous hydrogenated carbon films. *Thin Solid Films*, 146(1):93–107, 1987.

[18] A. Grill. Diamond-like carbon coatings as biocompatible materials - an overview. *Diamond Relat. Mater.*, 12(2):166–170, 2003.

[19] J. Robertson. Plasma deposition of diamond-like carbon. *Jpn. J. Appl. Phys.*, 50(1S1):01AF01, 2011.

[20] A. Grill. Diamond-like carbon: state of the art. *Diamond Relat. Mater.*, 8(2-5):428–434, 1999.

[21] A. Catena, T. McJunkin, S. Agnello, F. M. Gelardi, S. Wehner, and C. B. Fischer. Surface morphology and grain analysis of successively industrially grown amorphous hydrogenated carbon films (a-C:H) on silicon. *Appl. Surf. Sci.*, 347:657–667, 2015.

[22] A. Catena, S. Agnello, L. M. Rösken, H. Bergen, E. Recktenwald, F. Bernsmann, H. Busch, M. Cannas, F. M. Gelardi, B. Hahn, S. Wehner, and C. B. Fischer. Characteristics of industrially manufactured amorphous hydrogenated carbon (a-C:H) depositions on high-density polyethylene. *Carbon*, 96(6):661–671, 2016.

[23] A. Catena, Q. Guo, M. R. Kunze, S. Agnello, F. M. Gelardi, S. Wehner, and C. B. Fischer. Morphological and chemical evolution of gradually deposited diamond-like carbon films on polyethylene terephthalate: from subplantation processes to structural reorganization by intrinsic stress release phenomena. *ACS Appl. Mater. Interfaces*, 8(16):10636–10646, 2016.

[24] M. Rohrbeck, C. B. Fischer, S. Wehner, J. Meier, and W. Manz. DLC-coated pure bioplastic foil. *Vak. Forsch. Prax.*, 26(2):42–47, 2014.

[25] T. Schlebrowski, L. Beucher, H. Bazzi, B. Hahn, S. Wehner, and C. B. Fischer. Prediction of a-C:H layer failure on industrial relevant biopolymer polylactide acide (PLA) foils based on the sp2/sp3 ratio. *Surf. Coat. Technol.*, 368:79–87, 2019.

[26] T. Schlebrowski, L. Beucher, H. Bazzi, B. Hahn, S. Wehner, and C. B. Fischer. Changing Contents of Carbon Hybridizations in Amorphous Hydrogenated Carbon Layers (a-C:H) on Sustainable Polyhydroxybutyrate (PHB) Exhibit a Significant Deterioration in Stability, Depending on Thickness. *C*, 5(3):52, 2019.

[27] T. Schlebrowski, R. Ouali, B. Hahn, S. Wehner, and C. B. Fischer. Comparing the Influence of Residual Stress on Composite Materials Made of Polyhydroxybutyrate (PHB) and Amorphous Hydrogenated Carbon (a-C:H) Layers: Differences Caused by Single Side and Full Substrate Film Attachment during Plasma Coating. *Polymers*, 13(2), 2021.

[28] T. Schlebrowski, S. Wehner, and C. B. Fischer. Thin amorphous hydrogenated carbon layers on polylactic acid and polyhydroxybutyrate biopolymers - influence of substrate chemistry on interlayer formation. *Thin Solid Films*, 780:139943, 2023.

[29] J. A. Bittencourt. *Fundamentals of Plasma Physics*. Springer New York, New York, NY, 2004.

[30] G. Fußmann. Einführung in die Plasmaphysik: Vorlesung Vorlesung an der Humboldt Universität zu Berlin, 2001.

[31] A. A. Fridman. *Plasma chemistry*. Cambridge University Press, Cambridge, 2012.

[32] T. Manegold. *Untersuchungen zur Kollision und Kompression von Plasmen koaxialer Beschleuniger.* Dissertation, Johann Wolfgang Goethe-Universität, Frankfurt am Main, 2017.

[33] A. Küchler. *Hochspannungstechnik.* Springer Berlin Heidelberg, Berlin, Heidelberg, 2009.

[34] J. Wiechula. *Aufbau von koaxialen Plasmabeschleunigern zur Untersuchung von kollidierenden Plasmen.* Dissertation, Johann Wolfgang Goethe-Universität, Frankfurt am Main, 2015.

[35] H. Kuchling. *Taschenbuch der Physik: Mit zahlreichen Tabellen.* Fachbuchverl. Leipzig im Carl-Hanser-Verl., München, aktualisierte auflage 19 edition, 2007.

[36] E. Nasser. *Fundamentals of gaseous ionization and plasma electronics.* Wiley series in plasma physics. Wiley-Interscience, New York, 1971.

[37] M. Weiler, K. Lang, E. Li, and J. Robertson. Deposition of tetrahedral hydrogenated amorphous carbon using a novel electron cyclotron wave resonance reactor. *Appl. Phys. Lett.*, 72(11):1314–1316, 1998.

[38] D. A. McQuarrie. *Statistical mechanics.* University Science Books, Sausalito, Calif. and Great Britain, 2000.

[39] M. Ohring. *The materials science of thin films.* Academic Press, Boston, 1992.

[40] H.J.W. Müller-Kirsten. *Basics of statistical physics.* World Scientific, Singapore, 2. ed. edition, 2013.

[41] D. L. Smith. *Thin-film deposition: Principles and practice.* McGraw-Hill, Boston, Mass., internat. ed. edition, 1995.

[42] K. W. Kolasinski. *Surface science: Foundations of catalysis and nanoscience.* Wiley, Chichester, 2. ed. edition, 2008.

[43] A. D. Jenkins, P. Kratochvíl, R. F. T. Stepto, and U. W. Suter. Glossary of basic terms in polymer science (IUPAC Recommendations). *Pure and Applied Chemistry*, 68(12), 1996.

[44] S. Koltzenburg, M. Maskos, O. Nuyken, and R. Mülhaupt. *Polymere: Synthese, Eigenschaften und Anwendungen.* Springer Spektrum, Berlin, 2014.

[45] G. W. Ehrenstein and S. Pongratz. *Beständigkeit von Kunststoffen.* Edition Kunststoffe. Hanser, München, 2007.

[46] S. Fakirov. *Fundamentals of Polymer Science for Engineers.* John Wiley & Sons Incorporated, Newark, 2017.

[47] N. Peez, J. Becker, S. M. Ehlers, M. Fritz, C. B. Fischer, J.H.E. Koop, C. Winkelmann, and W. Imhof. Quantitative analysis of PET microplastics in environmental model samples using quantitative 1H-NMR spectroscopy: validation of an optimized and consistent sample clean-up method. *Anal. Bioanal. Chem.*, 411(28):7409–7418, 2019.

[48] N. Peez, M. C. Janiska, and W. Imhof. The first application of quantitative 1H NMR spectroscopy as a simple and fast method of identification and quantification of microplastic particles (PE, PET, and PS). *Anal. Bioanal. Chem.*, 411(4):823–833, 2019.

[49] N. Singh, O. A. Ogunseitan, M. H. Wong, and Y. Tang. Sustainable materials alternative to petrochemical plastics pollution: A review analysis. *Sustainable Horizons*, 2(1):100016, 2022.

[50] H. J. Endres and A. Siebert-Raths. *Technische Biopolymere: Rahmenbedingungen, Marktsitutation, Herstellung, Aufbau und Eigenschaften.* Hanser, München, 2009.

[51] Y. Tokiwa, B. P. Calabia, C. U. Ugwu, and S. Aiba. Biodegradability of plastics. *Int. J. Mol. Sci.*, 10(9):3722–3742, 2009.

[52] S. Mecking. Biologisch abbaubare Werkstoffe- Natur oder Petrochemie? *Angew. Chem.*, 116(9):1096–1104, 2004.

[53] A. S. Hoffman. Hydrogels for biomedical applications. *Adv. Drug Delivery Rev.*, 64:18–23, 2012.

[54] E. Pasquier, B. D. Mattos, H. Koivula, A. Khakalo, M. N. Belgacem, O. J. Rojas, and J. Bras. Multilayers of Renewable Nanostructured Materials with High Oxygen and Water Vapor Barriers for Food Packaging. *ACS Appl. Mater. Interfaces*, 14(26):30236–30245, 2022.

[55] J. C. Middleton and A. J. Tipton. Synthetic biodegradable polymers as orthopedic devices. *Biomaterials*, 21(23):2335–2346, 2000.

[56] A. Steinbüchel. Perspectives for Biotechnological Production and Utilization of Biopolymers: Metabolic Engineering of Polyhydroxyalkanoate Biosynthesis Pathways as a Successful Example. *Macromol. Biosci.*, 1(1):1–24, 2001.

[57] B. Kramp, H. E. Bernd, W. A. Schumacher, M. Blynow, W. Schmidt, C. Kunze, D. Behrend, and K. P. Schmitz. Polyhydroxybuttersäure (PHB)-Folien und -Platten zur Defektdeckung des knöchernen Schädels im Kaninchenmodell. *Laryngo-Rhino-Otologie*, 81(5):351–356, 2002.

[58] D. Chen and H. G. Zachmann. Glass transition temperature of copolyesters of PET, PEN and PHB as determined by dynamic mechanical analysis. *Polymer*, 32(9):1612–1621, 1991.

[59] Nicolas Jacquel, Chi-Wei Lo, Ho-Shing Wu, Yu-Hong Wei, and Shaw S. Wang. Solubility of polyhydroxyalkanoates by experiment and thermodynamic correlations. *AIChE Journal*, 53(10):2704–2714, 2007.

[60] S.R.P. Silva. *Properties of amorphous carbon*, volume 29 of *Emis data reviews series*. The Institution of Engineering and Technology, London, 2008.

[61] W. Jacob and W. Möller. On the structure of thin hydrocarbon films. *Appl. Phys. Lett.*, 63(13):1771–1773, 1993.

[62] A. Grill. Plasma-deposited diamondlike carbon and related materials. *IBM J. Res. Dev.*, 43(1.2):147–162, 1999.

[63] J. S. Hsu, S. S. Tzeng, and Y. J. Wu. Influence of hydrogen on the mechanical properties and microstructure of DLC films synthesized by RF-PECVD. *Vacuum*, 83(3):622–624, 2008.

[64] E. Tomasella, L. Thomas, M. Dubois, and C. Meunier. Structural and mechanical properties of a-C:H thin films grown by RF-PECVD. *Diamond Relat. Mater.*, 13(9):1618–1624, 2004.

[65] J. Robertson. Electronic processes in hydrogenated amorphous carbon. *J. Non-Cryst. Solids*, 198-200:615–618, 1996.

[66] E. Neyts, A. Bogaerts, and M.C.M. van de Sanden. Reaction mechanisms and thin a-C:H film growth from low energy hydrocarbon radicals. *J. Phys.: Conf. Ser.*, 86:012020, 2007.

[67] J. Robertson. Mechanical properties and coordinations of amorphous carbons. *Phys. Rev. Lett.*, 68(2):220–223, 1992.

[68] S. Neuville and A. Matthews. A perspective on the optimisation of hard carbon and related coatings for engineering applications. *Thin Solid Films*, 515(17):6619–6653, 2007.

[69] D. Liu, G. Benstetter, E. Lodermeier, and J. Vancea. Influence of the incident angle of energetic carbon ions on the properties of tetrahedral amorphous carbon (ta-C) films. *J. Vac. Sci. Technol., A*, 21(5):1665–1670, 2003.

[70] N. Selvakumar and H. C. Barshilia. Review of physical vapor deposited (PVD) spectrally selective coatings for mid- and high-temperature solar thermal applications. *Sol. Energy Mater. Sol. Cells*, 98(2):1–23, 2012.

[71] U. Narula, C. M. Tan, and C. S. Lai. Growth mechanism for low temperature PVD graphene synthesis on copper using amorphous carbon. *Sci. Rep.*, 7:44112, 2017.

[72] K. Choy. Chemical vapour deposition of coatings. *Prog. Mater. Sci.*, 48(2):57–170, 2003.

[73] N. A. Morrison, S. Muhl, S. E. Rodil, A. C. Ferrari, M. Nesládek, W. I. Milne, and J. Robertson. The preparation, characterization and tribological properties of ta-C:H deposited using an electron cyclotron wave resonance plasma beam source. *physica status solidi (a)*, 172(1):79–90, 1999.

[74] L. Kleinen, U. Böde, K. Schenk, H. Busch, J. Bradenahl, S. C. Müller, B. Hillebrands, and N. Laube. Amorphous carbon coatings inhibit crystalline biofilm formation on urological implants. *Plasma Process. Polym.*, 4(S1):S386–S391, 2007.

[75] L. Beucher, T. Schlebrowski, K. Rohe, S. Wehner, and C. B. Fischer. Surface treatment of biopolymer films Polylactic acid and Polyhydroxybutyrat with angular changing oxygen plasma - More than just gradual purification. *Surf. Interfaces*, 30(3):101856, 2022.

[76] A. Catena, M. R. Kunze, S. Agnello, F. M. Gelardi, S. Wehner, and C. B. Fischer. Amorphous hydrogenated carbon (a-C:H) depositions on polyoxymethylene: Substrate influence on the characteristics of the developing coatings. *Surf. Coat. Technol.*, 307(4):658–665, 2016.

[77] A. Marmur. Contact angle equilibrium: the intrinsic contact angle. *J. Adhes. Sci. Technol.*, 6(6):689–701, 1992.

[78] E. L. Decker, B. Frank, Y. Suo, and S. Garoff. Physics of contact angle measurement. *Colloids Surf., A*, 156(1-3):177–189, 1999.

[79] H. J. Busscher, A.W.J. van Pelt, P. de Boer, H. P. de Jong, and J. Arends. The effect of surface roughening of polymers on measured contact angles of liquids. *Colloids Surf.*, 9(4):319–331, 1984.

[80] K.F. Gebhardt. *Report: Grundlagen der physikalischen Chemie von Grenzflächen und Methoden zur Bestimmung grenzflächenenergetischer Probleme.* Stuttgart, 1982.

[81] B.K Tay, D. Sheeja, S.P Lau, and J.X Guo. Study of surface energy of tetrahedral amorphous carbon films modified in various gas plasma. *Diamond Relat. Mater.*, 12(10-11):2072–2076, 2003.

[82] R. Paul, S. N. Das, S. Dalui, R. N. Gayen, R. K. Roy, R. Bhar, and A. K. Pal. Synthesis of DLC films with different sp2/sp3 ratios and their hydrophobic behaviour. *J. Phys. D: Appl. Phys.*, 41(5):055309, 2008.

[83] L. Ostrovskaya. Studies of diamond and diamond-like film surfaces using XAES, AFM and wetting. *Vacuum*, 68(3):219–238, 2002.

[84] F. Piazza and G. Morell. Wettability of hydrogenated tetrahedral amorphous carbon. *Diamond Relat. Mater.*, 18(1):43–50, 2009.

[85] L. Ostrovskaya, V. Perevertailo, V. Ralchenko, A. Dementjev, and O. Loginova. Wettability and surface energy of oxidized and hydrogen plasma-treated diamond films. *Diamond Relat. Mater.*, 11(3-6):845–850, 2002.

[86] A. Bismarck, W. Brostow, R. Chiu, Haley E. Hagg L., and K.K.C. Ho. Effects of surface plasma treatment on tribology of thermoplastic polymers. *Polym. Eng. Sci.*, 48(10):1971–1976, 2008.

[87] H. Schönherr. *Surface Design: Applications in Bioscience and Nanotechnology.* John Wiley & Sons Incorporated, Weinheim, 1st ed. edition, 2009.

[88] N. Vandencasteele and F. Reniers. Plasma-modified polymer surfaces: Characterization using XPS. *J. Electron Spectrosc. Relat. Phenom.*, 178-179:394–408, 2010.

[89] L. A. Girifalco and R. J. Good. A theory for the estimation of surface and interfacial energies. i. derivation and application to interfacial tension. *J. Phys. Chem.*, 61(7):904–909, 1957.

[90] F. M. Fowkes. Attractive forces at interfaces. *Ind. Eng. Chem.*, 56(12):40–52, 1964.

[91] B. N. Altay, R. Ma, P. D. Fleming, M. J. Joyce, A. Anand, T. Chen, B. Keskin, D. Maddipatla, V. S. Turkani, P. R. Kotkar, A. Fleck, R. Rasheed, and D. He. Surface Free Energy Estimation: A New Methodology for Solid Surfaces. *Adv. Mater. Interfaces*, 7(6):368, 2020.

[92] M. Żenkiewicz. Methods for the calculation of surface free energy of solids. *J. Achiev. Mater. Manuf. Eng.*, 24(24), 2007.

[93] D. K. Owens and R. C. Wendt. Estimation of the surface free energy of polymers. *J. Appl. Polym. Sci.*, 13(8):1741–1747, 1969.

[94] D. H. Kaelble. Dispersion-polar surface tension properties of organic solids. *J. Adhes. Sci. Technol.*, 2(2):66–81, 1970.

[95] W. Rabel. Einige Aspekte der Benetzungstheorie und ihre Anwendung auf die Untersuchung und Veränderung der Oberflächeneigenschaften von Polymeren. *Farbe und Lack*, 1971(77):997–1005, 1971.

[96] S. Falah Toosi, S. Moradi, M. Ebrahimi, and S. G. Hatzikiriakos. Microfabrication of polymeric surfaces with extreme wettability using hot embossing. *Appl. Surf. Sci.*, 378:426–434, 2016.

[97] A. Scholze, W. G. Schmidt, and F. Bechstedt. Structure of the diamond (111) surface: Single-dangling-bond versus triple-dangling-bond face. *Phys. Rev. B: Condens. Matter Mater. Phys.*, 53(20):13725–13733, 1996.

[98] T. Huhtamäki, X. Tian, J. T. Korhonen, and R.H.A. Ras. Surface-wetting characterization using contact-angle measurements. *Nat. Protoc.*, 13(7):1521–1538, 2018.

[99] Micro and Nano Technologies, editor. *Microfluidics: modelling, mechanics and mathematics: Chapter 20 - surface tension*, volume 421-444. Elsevier, 2017.

[100] B. Krasovitski and A. Marmur. Drops down the hill: theoretical study of limiting contact angles and the hysteresis range on a tilted plate. *Langmuir*, 21(9):3881–3885, 2005.

[101] B. E. Rapp. Surface tension. In Micro and Nano Technologies, editor, *Microfluidics: Modelling, Mechanics and Mathematics*, volume 62, pages 421–444. Elsevier, 2017.

[102] J. T. Korhonen, T. Huhtamäki, O. Ikkala, and R.H.A. Ras. Reliable measurement of the receding contact angle. *Langmuir*, 29(12):3858–3863, 2013.

[103] DIN 53122-1:2001-08, Prüfung von Kunststoff-Folien, Elastomerfolien, Papier, Pappe und anderen Flächengebilden- Bestimmung der Wasserdampfdurchlässigkeit- Teil 1: Gravimetrisches Verfahren, 08.2001.

[104] International Organization for Standardization. ISO 2528:2017-10, sheet materials: Determination of water vapour transmission rate (WVTR).

[105] W. Demtröder. *Experimentalphysik 3: Atome, Moleküle und Festkörper*. Springer-Lehrbuch. Springer Berlin Heidelberg, Berlin, Heidelberg, 5. aufl. 2016 edition, 2016.

[106] H. Mei, R. Huang, J. Y. Chung, C. M. Stafford, and H. H. Yu. Buckling modes of elastic thin films on elastic substrates. *Appl. Phys. Lett.*, 90(15):295, 2007.

[107] A. A. Volinsky. Experiments with in-situ thin film telephone cord buckling delamination propagation. *MRS Online Proc. Libr.*, 749:72, 2002.

[108] G. Haugstad. *Atomic Force Microscopy*. John Wiley & Sons, Inc, Hoboken, NJ, USA, 2012.

[109] H. Günzler and H. U. Gremlich. *IR-Spektroskopie*. Wiley-VCH Verlag GmbH & Co. KGaA, Weinheim, Germany, 2003.

[110] D. Meschede and H. Vogel. *Gerthsen Physik*. Springer-Lehrbuch. Springer, Berlin, überarbeitete auflage 24 edition, 2010.

[111] Shimadzu Scientific Korea Corp. Accessories for fourier transform infrared spectrophotometers: FTIR series accessories: C103-E005P. C103-E005P, 2007.

[112] Klaus Wandelt, editor. *Surface and interface science: Volume 2: Properties of elemental surfaces*. Wiley-VCH, Weinheim, 2012.

[113] C. S. Fadley. X-ray photoelectron spectroscopy: Progress and perspectives. *J. Electron Spectrosc. Relat. Phenom.*, 178-179(1):2–32, 2010.

[114] J. F. Moulder, W. F. Stickle, P. E. Sobol, and K. D. Bomben. *Handbook of X-ray photoelectron spectroscopy: A reference book of standard spectra for identification and interpretation of XPS data*. Perkin-Elmer Corporation, Eden Prairie„ 1992.

[115] G. Bracco and B. Holst, editors. *Surface Science Techniques.* Springer Series in Surface Sciences. Springer Berlin Heidelberg, Berlin, Heidelberg, 2013.

[116] T. Werder, J. H. Walther, R. L. Jaffe, T. Halicioglu, and P. Koumoutsakos. On the Water-Carbon Interaction for Use in Molecular Dynamics Simulations of Graphite and Carbon Nanotubes. *J. Phys. Chem. B*, 107(6):1345–1352, 2003.

[117] P. M. Dietrich, T. Horlacher, P. L. Girard-Lauriault, T. Gross, A. Lippitz, H. Min, T. Wirth, R. Castelli, P. H. Seeberger, and W.E.S. Unger. Adlayers of dimannoside thiols on gold: surface chemical analysis. *Langmuir*, 27(8):4808–4815, 2011.

[118] F. C. Tai, S. C. Lee, C. H. Wei, and S. L. Tyan. Correlation between ID/IG ratio from visible raman spectra and sp2/sp3 ratio from XPS spectra of annealed hydrogenated DLC film. *Mater. Trans.*, 47(7):1847–1852, 2006.

[119] A. Nefedov and C. Wöll. Advanced Applications of NEXAFS Spectroscopy for Functionalized Surfaces. In G. Bracco and B. Holst, editors, *Surface Science Techniques*, volume 51 of *Springer Series in Surface Sciences*, pages 277–303. Springer Berlin Heidelberg, Berlin, Heidelberg, 2013.

[120] J. Stöhr. *NEXAFS Spectroscopy*, volume v.25 of *Springer Series in Surface Sciences Ser.* Springer Berlin / Heidelberg, Berlin, Heidelberg, 1st ed. edition, 1992.

[121] B. Watts, L. Thomsen, and P. C. Dastoor. Methods in carbon K-edge NEXAFS: Experiment and analysis. *J. Electron Spectrosc. Relat. Phenom.*, 151(2):105–120, 2006.

[122] J. Diaz, O. R. Monteiro, and Z. Hussain. Structure of amorphous carbon from near-edge and extended x-ray absorption spectroscopy. *Phys. Rev. B*, 76(9):388, 2007.

[123] O. Dhez, H. Ade, and S.G Urquhart. Calibrated NEXAFS spectra of some common polymers. *J. Electron Spectrosc. Relat. Phenom.*, 128(1):85–96, 2003.

[124] B. Brüster, C. Amozoqueño, P. Grysan, I. Peral, B. Watts, J. M. Raquez, P. Dubois, and F. Addiego. Resolving inclusion structure and deformation mechanisms in polylactide plasticized by reactive extrusion. *Macromol. Mater. Eng.*, 302(12):4579, 2017.

[125] J. L. Solomon, R. J. Madix, and J. Stöhr. Orientation and absolute coverage of benzene, aniline, and phenol on Ag(110) determined by NEXAFS and XPS. *Surf. Sci.*, 255(1-2):12–30, 1991.

[126] S. Tunmee, P. Photongkam, C. Euaruksakul, H. Takamatsu, X. Zhou, P. Wongpanya, K. Komatsu, K. Kanda, H. Ito, and H. Saitoh. Investigation of pitting corrosion of diamond-like carbon films using synchrotron-based spectromicroscopy. *J. Appl. Phys. (Melville, NY, U. S.)*, 120(19):994, 2016.

Part III.
Contributions

7. Surface treatment of biopolymer films Polylactic acid and Polyhydroxybutyrat with angular changing oxygen plasma – More than just gradual purification

This article by Lucas Beucher, Torben Schlebrowski, Kevin Rohe, Stefan Wehner and Christian B. Fischer has been released in *Surfaces and Interfaces* Volume 30, June 2022, 101856 with the DOI: 10.1016/j.surfin.2022.101856. The paper examines the O_2 pretreatment of the biopolymers PLA and PHB, which was previously perceived as a cleaning and activation process. The films used were purchased from Goodfellow GmbH, Friedberg, Germany. The plasma treatment was carried out at NTTF Coatings GmbH, Rheinbreitbach, Germany by L. Beucher. The measurements and evaluations of CA, morphology and WVTR were carried out by L. Beucher. The synchrotron based X-ray spectroscopy measurements were performed at the Helmholtz-Zentrum Berlin für Materialien und Energie, Berlin, Germany at the beamline of the Karlsruhe Institute for Technology, Group: Chemistry of oxidic and organic interfaces; X-ray and Electron Spectroscopy at Interfaces by L. Beucher, T. Schlebrowski, K. Rohe and C.B. Fischer. The analysis was carried out by L. Beucher. The results were presented and discussed in the Surface Physics research group. The formatting was changed and adapted to the thesis.

7.1. Graphical abstract
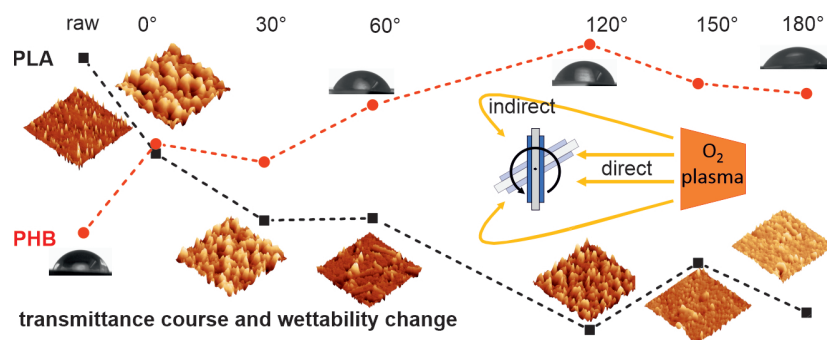
Fig. 33: Graphical abstract of surface treatment of biopolymer films Polylactic acid and Polyhydroxybutyrat with angular changing oxygen plasma – More than just gradual purification.

7.2. Abstract

Bio-based and biodegradable polymers such as polylactic acid (PLA) and polyhydroxybutyrate (PHB) are developing into increasingly important raw materials. Especially when it comes to replacing conventional polymers in order to save resources and reduce environmental impact. Such biopolymers often conform to mechanical requirements of industry, but inappropriate surface characteristics such as poor barrier properties and increased degradation limit their application. Appropriate surface modification, such as the deposition of thin amorphous hydrogenated carbon films (a-C:H) produced by low-temperature mediated radio frequency plasma-enhanced chemical vapor deposition (RF-PECVD) can provide a remedy here. Prior to this, the surfaces are mostly cleaned/activated with oxygen plasma to enable better deposition of the subsequent a-C:H layer. It has been noticed that the O_2 treatment,

strongly changes the surface properties. It is now to be determined how a change in the O_2 plasma treatment geometry affects the surface properties and whether this can be used accordingly. Surface morphology was analyzed by AFM, surface free energy (SFE) was determined using a contact angle goniometer, and changed barrier properties were investigated via the water vapor transmission rate. Top surfaces were studied by synchrotron supported X-ray spectroscopy, revealing angle-dependent changes in C and O content and binding conditions. The present angle-dependent O_2 treatment not only changed the surface roughness and its chemical composition, but also, contrary to expectations, improved the barrier properties of PLA up to 18% at highest value, while the transmittance of PHB increased by more than 10%. A similar change in the mobility of the contact angle hysteresis is observed for both materials.

7.3. Introduction

Surface modifications by plasma-based treatment processes are nowadays having an ever-increasing influence on the manufacturing processes of functional products. Since only the surface properties are changed in these processes, the main properties of the substrate material are retained. In this context, it appears advantageous to treat or coat polymers in particular, due to their intrinsic properties and versatile application possibilities, in order to generate customized surfaces. Due to their sustainability and environmental compatibility, biopolymers are also increasingly used in this field [1]. Two types of biopolymers are used largely in industry and agriculture. One is polylactic acid (PLA) produced by condensation polymerization of lactic acid [2–4]. And secondly polyhydroxybutyrate (PHB), which belongs to the class of polyhydroxyalkanoates and is polymerized by a fermentative production process of sugar and starch [3,5]. An established plasma-based coating technique for improving the surface properties of biopolymers is the covering with a barrier layer of hydrogenated amorphous carbon (a-C:H) [6–15]. A commonly used process for this is chemical vapor deposition (CVD), which can be further enhanced by the use of radio-frequency plasma (RF-PECVD), enabling deposition at low temperatures and allowing coatings on non-conductive substrates. In our previous research [10,15], it was found that the geometry of the coating is a determining factor for the composition of the later a-C:H layer. The substrate was placed directly in front of the plasma source, or indirectly by treating the substrate on the side opposite to the plasma (180° rotation). The results suggested that the layer properties, especially the sp^2/sp^3 ratio, can be controlled by changing the deposition angle so that the surfaces can be adapted and thus customized. Before applying any a-C:H layer, the surface is pretreated resp. cleaned with an O_2 plasma [10–15]. It was found that this preceding step also significantly changes the starting material. Additionally, the geometry of the oxygen treatment affects the surface properties such as contact angle and roughness [10,15]. In the present work, the surface modification occurring with a geometrically changing O_2 plasma treatment will be investigated in order to reveal specific surface and material effects. Therefore, the present study focuses on a stepwise angle-dependent O_2 plasma treatment for the biopolymers PLA and PHB and their associated property changes. The surface morphology was studied by atomic force microscopy (AFM). Surface sensitive and synchrotron supported X-ray techniques such as near edge X-ray absorption fine structure analysis (NEXAFS) and X-ray photoelectron spectroscopy

(XPS) were used to analyze the chemical composition of the O_2 plasma treated PLA and PHB. Contact angles (CAs) with different liquids were performed to evaluate macroscopic physical aspects and obtain information on surface free energy (SFE) and contact angle hysteresis (CAH). The barrier properties were measured by water vapor transmission rate (WVTR) revealing a significant difference between both angle-dependent, O_2 plasma treated biopolymers.

7.4. Materials and methods

Sample preparation and film deposition

Films of PLA (50 μm) and PHB (25 μm, 92% PHB and 8% polyhydoxyvalerate blend) of industrial quality (Goodfellow GmbH, Friedberg, Germany) were cut to 10×5 cm pieces and clamped in self-made aluminum sample holders. These were fixed to an in-house manufactured device at angles from 0° to 180° in 30° steps, as shown in Fig. 34. Since no significant change in the surface could be observed at a treatment angle of 90°, this will not be considered further in the following. The center of the samples was always 275 mm apart from the RF-driven plasma source (13.65 MHz Copra DN 400, CCR GmbH, Troisdorf, Germany). The samples were treated with O_2 plasma (O_2 purity: 6.0) for 10 min (1 Pa, 60 $sccm/min$, 200 W, further details in ref: [10–15]) and for each fixed angle geometry between the maximum values, directly 0° and indirectly 180° angle [10,15]. The occurring low process temperature on the sample ($< 40°C$) prevents structural changes within the biopolymer [10].
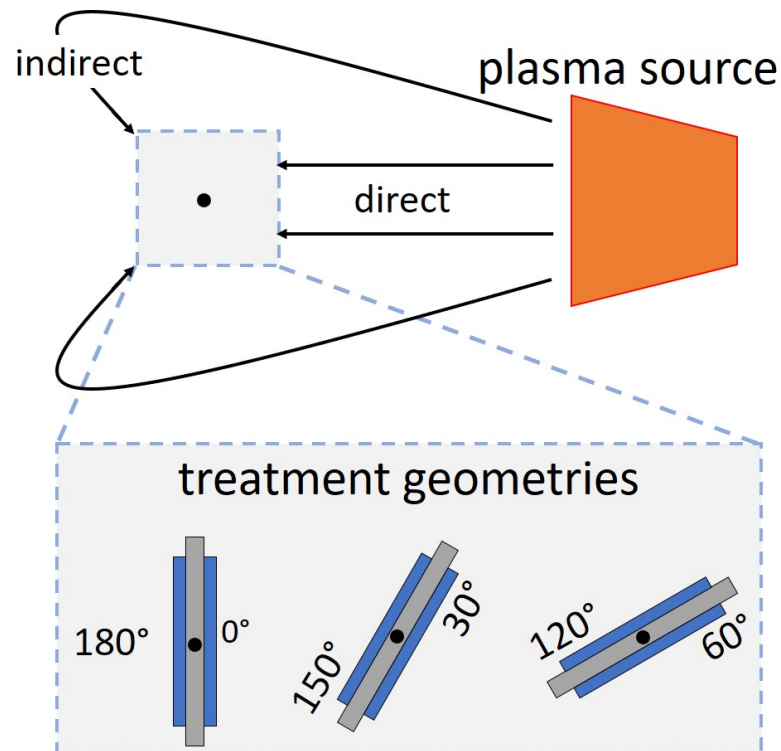

Fig. 34: Schematic of the fixed angle-dependent O_2 plasma treatment process in top view. The treatment was performed for 10 min with a source distance of 275 mm. The center of the samples marked with a black dot is the pivot point.

AFM imaging

The surface morphology of the O_2 plasma treated polymer films was examined with an atomic

force microscope Asylum Research MFP-3D-BIO (Oxford Instruments, Abingdon, UK). The measurement was performed in contact mode at ambient conditions, recording a height profile of an area of $5 \times 5\mu\ m^2$ with a resolution of 512 scan points, corresponding to a pixel image size of $512 \times 512\ px$. The measurement was performed at a speed of $5\mu m/s$ with AC240TS cantilevers (Oxford Instruments, Abingdon, UK). The recorded images were analyzed and processed using the Gwyddion 2.58 software (GNU General Public License). In the present study, all micrographs show a 3D representation of the deflection retrace. Filters with a mean, a median, and a conservative noise reduction of $3\ px$ each were applied to smooth artifacts and suppress noise. A minimum of three different positions distributed across the sample were recorded. Repeating the AFM measures ensured correctness of acquisition. The roughness R_a and R_q were statistically determined from the height retrace (same parameter set as deflection retrace).

Contact angles (CA)

To analyze the surface wettability of the O_2 plasma treated polymer films a contact angle goniometer (OCA 15EC, DataPhysics Instruments GmbH, Filderstadt, Germany) was used. For this purpose, drops of $1\mu l$ deionized water (HPLC grade, CHEMSOLUTE ®, Th. Geyer GmbH & Co. KG, Renningen, Germany) were dispensed at ambient conditions with the sessile drop technique. To ensure the accuracy of the values obtained, the CA was determined at five different locations. The resulting mean value adequately describes the average wettability of the surface. The CA were evaluated with the software SCA202 V5.0.41 (DataPhysics Instruments GmbH, Filderstadt, Germany).

Contact angle hysteresis (CAH)

To determine the advancing CA (ACA) and receding CA (RCA) of the hysteresis (CAH), a drop of $1\ \mu l$ was added to each surface while keeping the dosing syringe centered in it. The droplet was then expanded with an additional $5\ \mu l$ dosage, allowing the ACA to be determined. RCA was assayed by removing $4.5\ \mu l$ from the droplet. This procedure was repeated five times in succession. The ACA and RCA value can be measured respectively when droplet volume and baseline of the droplet change; meanwhile, the CA remains constant [16]. The CAs were measured automatically using SCA202 V5.0.41 software (DataPhysics Instruments GmbH, Filderstadt, Germany) with the sessile drop (needle in) method. The CAH indicates the distance between ACA and RCA and can be obtained by subtraction. The CAH not only provides information on wettability and surface energy, but is also a measure for surface roughness and adhesion [16,17].

Surface free energy (SFE)

The SFE was determined indirectly by observing disperse as well as polar interactions with CA analysis and subsequently using the Owens, Wendt, Rabel and Kaelble method (OWRK). In this method, charge distributions are determined between temporarily occurring asymmetric charge distributions: dispersion forces (e.g. hydrocarbons) and polar forces (e.g. water). A spectrum of five liquids was selected to determine the polar γ_p and disperse γ_d fractions and the total SFE. As liquid with high electronegativity difference HPLC water ($\gamma_d \approx\ 26\ mN/m$,

$\gamma_p \approx 47\ mN/m$) [18] was used and as liquid with dominant non-polar portion diiodomethane ($\gamma_d \approx 47\ mN/m$, $\gamma_p \approx 3\ mN/m$) [19] and 1-bromonaphthalene ($\gamma_d \approx 44\ mN/m$, $\gamma_p \approx 0\ mN/m$) [19]. Furthermore the CAs of formamide ($\gamma_d \approx 28\ mN/m$, $\gamma_p \approx 29\ mN/m$) [18] and ethylene glycerol ($\gamma_d \approx 26\ mN/m$, $\gamma_p \approx 21\ mN/m$) [18] were measured. A separate sample surface location was used for each liquid and the CAs were measured in triplicate. The data analysis was performed with the internal software SCA202 V5.0.41 (DataPhysics Instruments GmbH, Filderstadt, Germany).

Water vapor transmission rate (WVTR)

The WVTR measurements were performed with a W3/031 Water Vapor Transmission Rate Tester from Labthink (Labthink GmbH, Neu Isenburg, Germany). The WVTR indicates how much moisture passes through a volume, referred to 24 h and normalized to $1 m^2$ under specified test conditions from a wet room through the test area/volume into the test room. The WVTR depends on the thickness, the test area, the density as well as the surface properties of the material according to DIN 53,122–1/ISO 2528:2017 [20,21]. The measuring area of the sample is 4.91 cm^2, clamped in a customized adapter in a sealed test dish containing 10 ml of deionized water, with the O_2 treated sample surface not facing the water reservoir. At 38°C a relative humidity difference of 90 %RH is generated between both sides of a sample [20,21]. The water vapor penetrates through the sample into the dry side and is continu- ously detected by a sensor. Each test dish was weighed after a test interval of 90 min to determine the amount of water evaporated, the procedure was repeated four times per measurement. To ensure reproducibility and the stability of the polymer films, each sample was measured twice.

Synchrotron based X-ray spectroscopy

The composition of the carbon and oxygen compounds on the surface was investigated with X-ray photoelectron spectroscopy (XPS) and near- edge X-ray absorption fine structure (NEXAFS, see SI). Both were performed at the Helmholtz-Zentrum Berlin with beamline HE-SGM during the low alpha mode (ring current max. 100 mA, decay mode). The HE- SGM analytical system is described in detail elsewhere [22]. For XPS the spectrum between 600 and 0 eV was recorded at two different sample positions with a resolution of 0.1 eV, for reproducibility and to ensure homogeneity. The C1s peak was analyzed with software CasaXPS (software version 2.3.18, Casa Software Ltd., United Kingdom) and the proportions of sp^2, sp^3, C=O and C−O bonds in the $C1s$ peak were identified and evaluated [23–25]. In addition, the $O1s$ peak was verified to be present in the layers (see SI).

7.5. Results and discussion

7.5.1. AFM imaging

The surface morphology of PLA treated with O_2 plasma recorded by AFM are displayed in Fig. 35 and that of PHB in Fig. 35a shows the raw, untreated PLA, representing the initial morphology and reference for the other PLA surfaces treated by O_2 plasma Fig. 35b–g show the surfaces treated with O_2 plasma in an angle-dependent manner, between 0° and 180° in 30° steps and 10 min duration each. Table 2 lists the values of average roughness R_a and root mean square roughness R_q of the samples. The surface of the raw PLA (Fig. 35a)

shows a smooth, homogeneous surface with small particles of 0.1 to 0.4 μm size attributed to manufacturing processes. The height profile shows a difference of 8 nm, which agrees well to the roughness R_a and R_q (Table 2). In contrast, the surface treated in direct O_2 plasma (0°, Fig. 35b) shows significant changes. Small surface particles are no longer detected and the previously smooth surface exhibits a pronounced coarse graining. Therefore, R_a increases to 41.9 nm, and the height profile to 13.2 nm. This granular texture is evident in all samples treated with O_2 plasma, regardless of the treatment angle, but it is most distinct in direct treatment. By increasing the angle, the grain size becomes progressively finer and the structure is less visible, also reflected in the height profile and a decreasing roughness, which can be attributed to the decrease in the incident ion energy. At 30° (Fig. 35c) R_a is 35.9 nm, lowering to 21.1 nm at 60° (Fig. 35d). The grain size decreases particularly between 120° (Fig. 35e) and 150° (Fig. 35f), likewise R_a decreases from 19.2 to 10.1 nm. At 180° (Fig. 35g) in the lower area, a pore is visible attributed to the manufacturing process [11]. The noticeable decrease in graininess according to the angular changing O_2 plasma treatment is also evident there with a minimum of 8.2 and 11 nm, respectively, which is nearly the roughness of the raw PLA.

In Fig. 36 the morphology of untreated PHB (Fig. 36a), as well as the PHB surfaces treated with O_2 plasma are displayed (Fig. 36b-g). As for PLA, the PHB surfaces are exposed to the O_2 plasma for 10 min at the respective angles between 0° to 180° in 30° steps. The surface of the untreated PHB shows a fine structure, linear elevations ("worm-like", see 2D in SI) [10] appear repeatedly with a R_a of 15.5 nm (Table 2). These structures are also detectable on the PHB samples treated with O_2 plasma, but the angle-dependent treatment does not appear to have any effect on them. The surface after direct plasma treatment (0°, Fig. 36b) shows hardly any changes, which is reflected in a nearly unchanged R_a of 17.9 nm, indicating that PHB behaves differently under ion bombardment than the chemically similar PLA. At 30° (Fig. 36c), these structures are particularly clearly visible, which also explains the somehow increased R_a. Similarly, at 120°, they are readily discernible with a comparatively low R_a of 15.1 nm. The large R_a of $27.5 nm$ at 180° (Fig. 36g) is attributed to a small curvature in the film, as well as isolated higher peaks.

Table 2: Average roughness R_a and the root mean square roughness R_q of untreated and angle dependent O_2 plasma treated PLA and PHB.

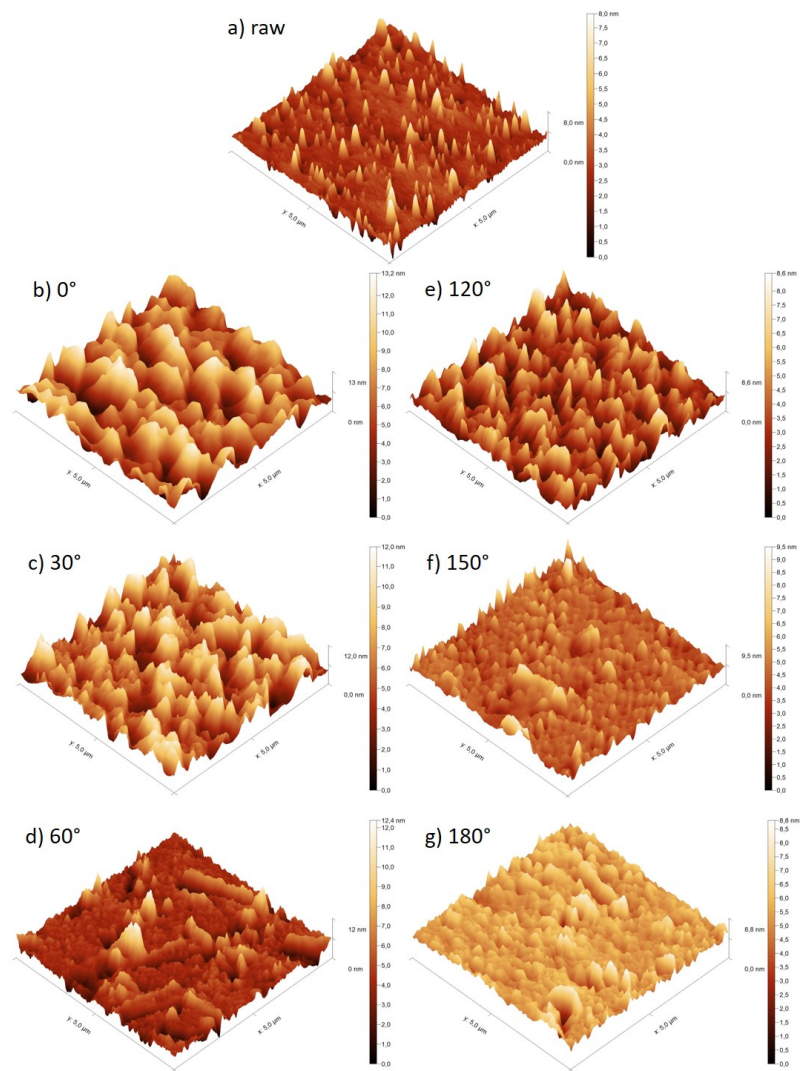|	PLA		PHB	
	R_a/nm	R_q/nm	R_a/nm	R_q/nm
raw	8.3 ± 2.3	10.8 ± 2.8	15.5 ± 3.5	19.1 ± 3.7
0°	41.9 ± 8.5	51.8 ± 9.7	17.9 ± 6.1	23.2 ± 6.9
30°	35.9 ± 9.7	44.7 ± 10.6	21.0 ± 6.3	25.8 ± 7.0
60°	21.1 ± 10.7	29.0 ± 14.7	13.3 ± 2.5	15.8 ± 3.0
120°	19.5 ± 3.9	23.8 ± 4.9	15.1 ± 5.1	19.2 ± 6.4
150°	10.1 ± 3.9	13.6 ± 4.6	14.0 ± 2.5	18.1 ± 2.4
180°	8.2 ± 2.4	11.0 ± 3.3	27.3 ± 11.7	34.6 ± 13.3

Fig. 35: $5.0 \times 5.0 \ \mu m^2$ AFM images showing untreated (a) and angle dependent O_2 plasma treated PLA for 0° to 180° (b-g).
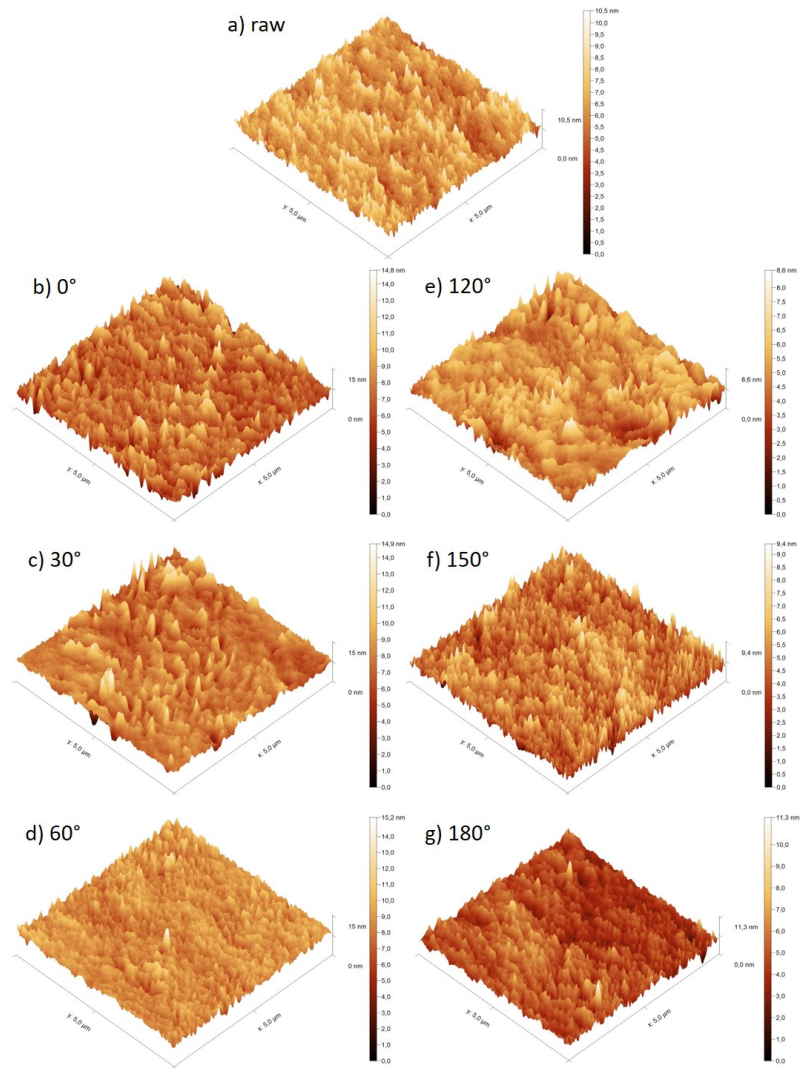
Fig. 36: $5.0 \times 5.0 \ \mu m^2$ AFM images showing untreated (a) and angle dependent O_2 plasma treated PHB for $0°$ to $180°$ (b-g).

7.5.2. Contact angle (CA)

The overall surface wettability results from the morphology of the surface and the prevailing chemical bonds [10–17,26,27]. As a result, of the treatment with O_2 plasma, it can be assumed that oxide groups are formed on the sample surface, which leads to a hydrophilic character [26–29]. In addition, the hybridization state causes a change. A sp^3 rich surface results in a reduced contact angle compared to a sp^2 rich surface due to the difference in surface free energy [10–17,26–28]. Fig. 37 shows the CAs of the angular O_2 treated PLA and PHB samples. For reference, the contact angles of raw, untreated PLA ($78°$) and PHB ($75°$) are plotted. The CA of both materials decreases after direct treatment, which can be explained by the oxidation, but also by the roughening of the surface (Table 2). The CA of PLA decreases with $67°$ more than that of PHB with $72°$. Differences between both materials can also be seen for error analysis. In the case of PLA, it changes only insignificantly over the treatment angles and remains almost constant. When the error bars are compared with the obtained roughness (Table 2), it is noticeable that this factor seems to play a major role; with smaller roughness, the error bar is also small and inverted. Such a behavior cannot be observed for

PLA. With increasing treatment angle, the CA of PLA initially increases to about 70° at 30°, then remains constant up to 120° in the error interval, and decreases again to about 67° at 150° and 180°, which is consistent with the XPS analysis (Section 3.6). For PHB, the CA de- creases continuously from 0° to 60° from 72° to 61°, increases slightly at 120°, indicating a decreasing sp^3 content, but remains almost constant within the error interval until 180° at around 64°.
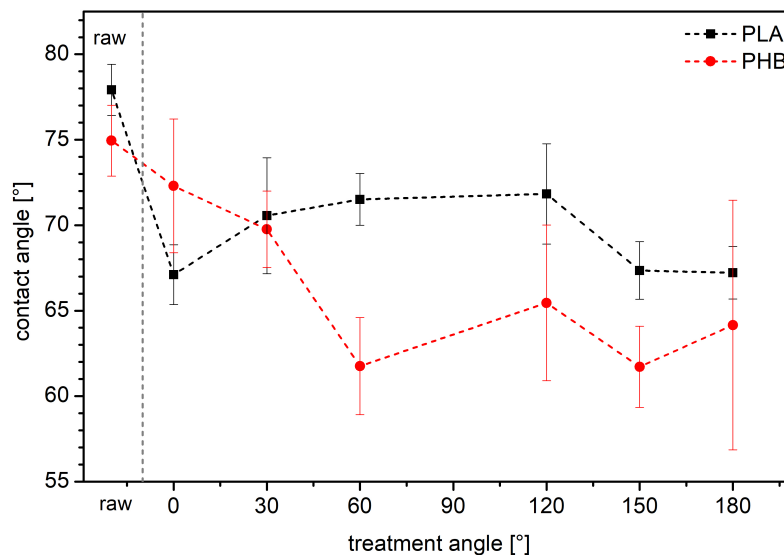

Fig. 37: CA of angle-dependent O_2 plasma treated PLA and PHB surfaces between 0° and 180°. The first measured value shows the raw and untreated polymer.

7.5.3. Surface free energy (SFE)

The OWRK method for determining the surface energy is described in detail elsewhere [30–32]. SFE results from the wettability of different liquids. Therefore, morphology, chemical bonds and hybridization states are of crucial importance. Oxidized surfaces form a stronger dipole moment, which leads to a stronger interaction with polar liquids and thus to a more hydrophilic layer [33]. In the hybridizations of C, sp^3 rich surfaces of compounds exhibit not only a higher wettability for water but also an increased surface energy, in contrast to sp^2 rich surfaces, which have a lower SFE and an increased CA [34]. Since at least three measuring locations per liquid (here water, diiodomethane, 1-bromonaphthalene, formamide, and ethylene glycerol) and sample are averaged, morphological irregularities should not have a statistical effect. Fig. 38 shows the SFE for the angular O_2 plasma treated PLA surface split into the polar and disperse component. It can be seen that the disperse component always accounts for the larger fraction of the SFE, except for the direct plasma treatment at 0°. The maximum of the disperse component shows the surface of the raw PLA (first value) and at the same time the lowest amount of polar interaction. However, due to the O_2 plasma process and the resulting oxidation of the surface, this fraction increases strongly while the disperse component decreases strongly at the same time. This is most evident in the frontal plasma treatment (0°); the disperse fraction decreases from approx. 40 to 30 mN/m and the polar fraction increases from 2 to 11 mN/m, but the total SFE changes only slightly. This suggests O_2 groups on the surface giving a higher polar fraction of the SFE [29], which can also be

seen in the CA (Fig. 37). In the further course, the polar fraction remains roughly the same for 30° to 120°, changing from 7 to 6 mN/m; which is consistent with the CA findings. The disperse fraction rises from 30 mN/m at 0° to 37 mN/m at 30°, drops to 32 mN/m and rises again to 40 mN/m at 120° where it continuously decreases to 35 mN/m again at 180°. The increased disperse fraction is attributed to the fact that more indirect plasma is applied, which also has less energy for surface activation [10, 12–14,20]. Considering error bars, it is noticeable that they are in a small range for raw PLA, 150° and 180°. Here only indirect plasma radiation (150° and 180°) arrives and no mixtures. Fig. 39 shows the SFE for the angular O_2 plasma treated PHB, the SFE is separated into its polar and disperse component. Raw PHB has an SFE of 44.5 mN/m, which is split into a polar component of 3 mN/m and a disperse of 41.5 mN/m. The disperse fraction is thus similar to that of PLA (Fig. 38), but the slightly higher polar fraction in PHB is different, resulting in a slightly higher SFE overall. As for PLA, the SFE decreases after frontal O_2 plasma treatment, with primarily the disperse fraction decreasing to 35.5 mN/m - is higher than for PLA with 40 mN/m - the disperse increases to 5 mN/m - is lower than for PLA with 11 mN/m. For 30°, the polar and disperse values remain similar, but the disperse component increases again to40 mN/m at 60°, with the polar continuing to remain constant up to 120°. The disperse component de- creases continuously from 40 to 36 mN/m from 60° to 180° - thus PLA and PHB are similar in the behavior of the disperse component at indirect treatment angles. In contrast to PLA, the polar component increases from 5 mN/m (60°) to 12 mN/m (180°) - with PLA, the polar component decreases. The strong increase at 180° can be explained by the strongly enhanced roughness and its large error bar (Table 2).
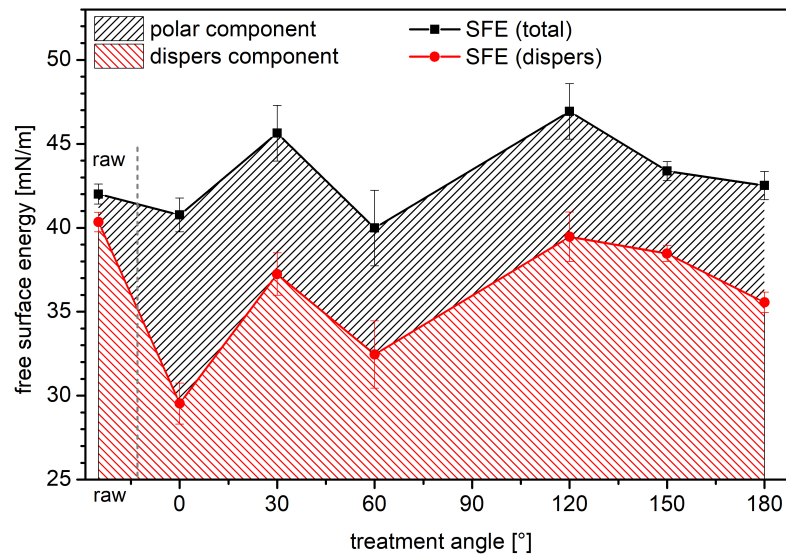

Fig. 38: SFE course of PLA, treated for 10 min with O_2 plasma with advancing angle geometries. The first value is the raw sample; the black squares are the total SFE. The red dots and the red hatched pattern below are the disperse component of the total SFE in which the black hatched area shows the polar component.

Fig. 39: SFE course of PHB, treated for 10 *min* with O_2 plasma with advancing angle geometries. The first value is the raw sample; the black squares are the total SFE. The red dots and the red hatched pattern below are the disperse component of the total SFE in which the black hatched area shows the polar component.
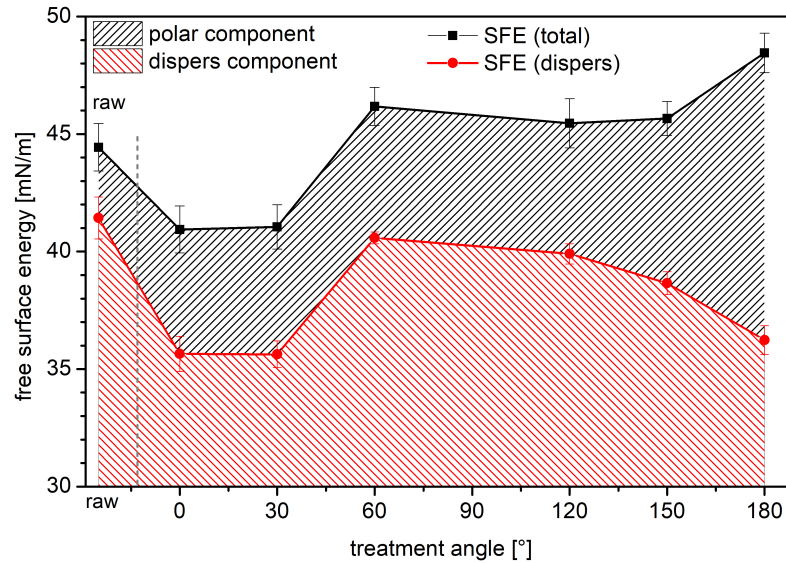
7.5.4. Contact angle hysteresis (CAH)

Another characterization technique for the chemical and topographical investigation of the surface is the CAH, which is obtained indirectly via the difference of the advancing (ACA) and receding CA (RCA) (Table 3). The ACA provides details about interactions between solid and water and thus wettability; the RCA removes the droplet from the surface and is related to adhesion forces between solid and the water droplet. Overall, the hysteresis can be seen as a measure for the mobility of a water droplet on the surface (the wetting and removal) [16,17]. Fig. 40 presents the data for the CAH of PLA and PHB untreated surfaces, as well as the angle dependent O_2 plasma treated ones. The corresponding ACA and RCA are listed in Table 3. With a few exceptions, both materials show the same tendency, which is characterized by the fact that, with direct treatment, the mobility initially increases steeply with increasing angle, but then decreases and no longer reaches the value of the raw polymer. The two raw polymers have a similar hysteresis of about 23°, and ACA and RCA are also close to each other (see Table 3). With direct O_2 treatment, the CAH for PLA increases, which is partly due to the increase in the polar fraction of the SFE, and partly associated with the increased roughness after treatment. The high polar fraction is also reflected in the ACA and RCA, both of which decrease to their minimum (compare CA, Fig. 37). Further, the low RCA shows that here the adhesion forces due to the polarity of the surface is at its maximum [16,17,35,36]. At 30°, the CAH for PLA reaches its maximum of 39.3°, the ACA returns to about the initial value; the RCA does not increase as much (which also gives the large CAH). Subsequently, the CAH successively decreases to 31.1° for a treatment angle of 180°. This result correlates, on the one hand, with the decrease of the polar fraction of the SFE (especially for indirect treatments) and, on the other hand, with the decrease of the surface roughness (Table 2). In the case of PHB, the CAH initially decreases with direct treatment or remains at a similar level in the defect analysis, which is due to the only slightly

changing RCA. An explanation for this is the only slightly changing roughness of the surface, as well as the only little changing polar fraction of the SFE. Since the SFE remains constant even at a treatment angle of 30°, the change here is due to the increasing roughness. Since at 60° the roughness decreases again, the increase in CAH to 38.3° here is due to the increasing SFE. The constant value at 120° can also be explained in this way. The CAH for 150° and 180° are also similar and are at about 32°. The large error at 180° can be explained by the larger surface roughness (Table 2) and the sudden increase in the polar fraction of the SFE.

Table 3: Advancing (ACA) and receding contact angle (RCA) of raw and angle dependent O_2 plasma treated PLA and PHB.

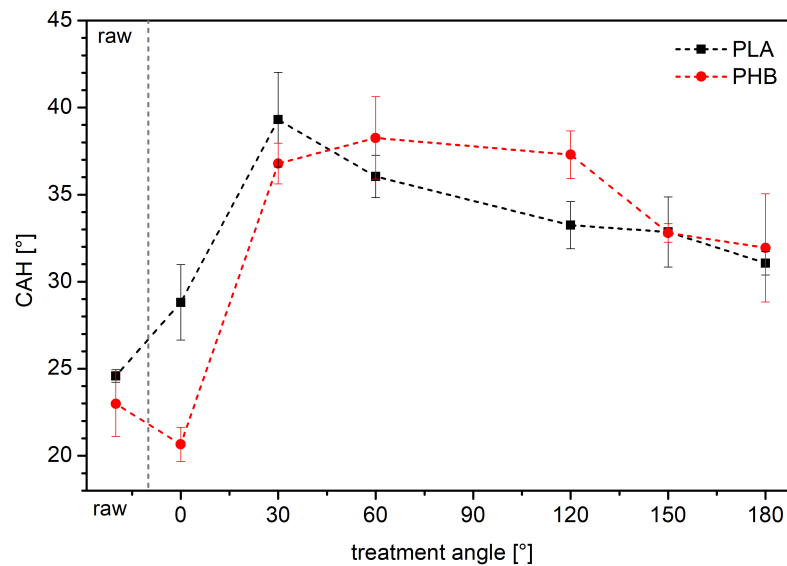| coating angle	ACA [°]			RCA [°]		
	2.5 min	5.0 min	10.0 min	2.5 min	5.0 min	10.0 min
0°	67.9 ± 0.3	73.4 ± 1.5	68.5 ± 1.0	31.5 ± 1.5	32.5 ± 1.6	28.6 ± 0.9
30°	63.9 ± 0.5	70.1 ± 0.3	69.9 ± 0.2	30.7 ± 1.3	31.3 ± 1.1	29.8 ± 0.1
60°	73.7 ± 1.2	72.9 ± 0.8	69.4 ± 1.3	30.5 ± 1.8	32.2 ± 0.8	28.7 ± 1.1
120°	65.2 ± 0.4	70.1 ± 1.0	65.5 ± 0.6	26.2 ± 2.2	28.5 ± 2.6	24.7 ± 2.8
150°	61.4 ± 0.8	70.0 ± 0.3	68.7 ± 1.5	29.6 ± 1.0	26.2 ± 2.7	30.8 ± 2.2
180°	70.5 ± 1.2	67.2 ± 0.2	70.4 ± 0.3	29.7 ± 2.4	28.2 ± 2.2	29.8 ± 4.6

Fig. 40: CAH of the angle dependent O_2 plasma treated PLA and PHB surfaces. The first value shows the raw and untreated polymers.

7.5.5. Water vapor transmission rate (WVTR)

The water vapor transmission is a gravimetric method and described as per definition the penetration of water vapor through a volume with a standardized area to one m^2 during a period of 24 h under defined test conditions: From the absorption room (dish), through the test area resp. volume of the sample film into the test room. The WVTR depends on the film thickness, test area, material density, and the properties of surface resp. deposited layer [20,21], i.e. it is not a material constant in itself. Raw PLA has the highest water permeability at 121 g per m2 per 24 h, as shown in Fig. 41. Since the morphology of the surface appears rough and uneven and there are inclusions from the manufacturing process (Fig. 2 AFM),

the diffusion of water molecules is obviously favored despite high CA [11,37]. It has also been shown that PLA has process-induced channeling through which liquid can penetrate the polymer [11,37]. If the raw polymer is treated with O_2 plasma for 10 min at advancing angle settings, a drop in permeability is observed up to the 120°. Compared to the CAs and the roughness (Table 2), a different picture emerges, since the CA and the roughness initially rises. From this it can be concluded that no or only limited conclusions about the WVTR can be drawn from the CA, since the already mentioned channels are a volume specific component. From 120° to 180° the permeability remains constant at around 102 $g/(m^2 \cdot 24h)$ within the error. This phenomenon is not yet fully understood and is the subject of current research. One explanation could be a reorganization of the formed oxygen-containing groups, which are reactive molecules on the surface of the PLA. Indirect irradiation reduces the penetration depth of the plasma bombardment. Therefore, the retention time of the radicals on the surface could be extended and this reorganization process could be promoted, possibly closing or narrowing channel entrances. Oxide containing groups, such as hydroxyl groups, lead to more absorption sites [5,10,12,15,38] which further blocks the diffusion of the reactant in the near surface areas of polymer substrates [39]. The WVTR values of PHB film show a different course in Fig. 41 compared to the PLA one. The transmission rate increases instead of decreasing as in the case of PLA. Furthermore, the initial value of the raw material of 201 $g/(m^2 \cdot 24h)$ is significantly higher, which is mainly related to the lower material thickness of 25 μm. Both the initial value and the WVTR for 0° treatment are close to each other and both show pronounced errors, which is attributed to the low film thickness. From 30°, the errors become smaller and allow a more accurate evaluation. The WVTR for 30° is 211.6 $g/(m^2 \cdot 24h)$ and similar to 60° with 219.8 $g/(m^2 \cdot 24h)$. The maximum transmittance is reached at 228.6 $g/(m^2 \cdot 24h)$ at 120°, then drops slightly to 222 $g/(m^2 \cdot 24h)$ for 150° and 180°. It is assumed that the slight increase in transmission is due to the increase in the polar fraction of the SFE (Fig. 39), as well as the surface area increase due to the roughness increase (Table 2).
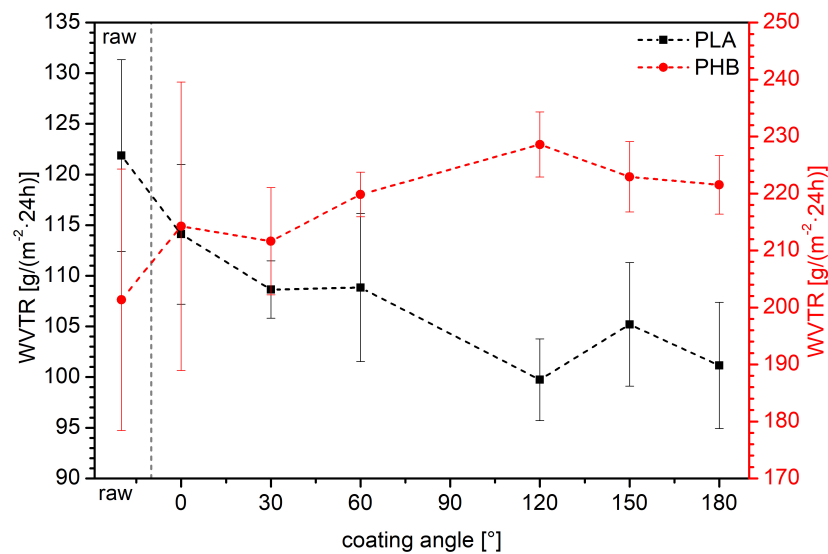

Fig. 41: WVTR values of the PLA and PHB films untreated (first value) and treated for 10 min with O_2 plasma with advancing angle geometries. The left y-axis presents the WVTR for PLA (black) and the right y-axis for the PHB (red, note different scaling).

7.5.6. X-ray photoelectron spectroscopy (XPS)

In Fig. 42, the fraction of carbon-containing binding states of the C1s signals (see SI) is shown as a percentage of sp^2, sp^3, C−O and C=O binding for a raw PLA sample and PLA surface treated with O_2 plasma in an angle-dependent manner. The quantitative binding percentages are plotted versus the ascending O_2 plasma angle treatment geometry. Data analysis was performed as described in the experimental section. The positions were evaluated using the NIST database and the work of other groups [23–25]. It can be seen that the chemical composition of the PLA surface hardly changes after direct O_2 treatment. The sp^3 fraction remains dominant ($\approx 73\%$) and is slightly increased; correspondingly, the remaining bonds are slightly decreased ($sp^2 \approx 10\%$, C−O $\approx 1\%$, C=O $\approx 15\%$). Even with the changing treatment angles, the composition appears to remain nearly stable at 30°. At 60° the sp^3 fraction decreases slightly and the C−O fraction is increased, this also coincides with a decrease of the disperse fraction of the SFE (Fig. 38); the WVTR value is almost the same but the error strongly increased to 30°. At 150°, the sp^2 fraction decreases to 5% and the C−O fraction increases to 7%. Here it can be observed that in the case of SFE, the polar component decreases and the WVTR value increases with a larger error compared to 120° and 180°. At 180°, sp^2 rises again to 10% and C−O drops to 9%. The WVTR lowers in value and the polar components behaves similarly to 150°. PHB shows a similar behavior as PLA for the raw polymer with a binding ratio of $\approx 71\%$ sp^3, $\approx 7\%$ sp^2, $\approx 2\%$ C−O and 20% C=O (Fig. 42). After direct O_2 treatment, the sp^3 value increases to 75%, drops to 62% at 30° and increases again successively to 76% until 180°. The sp^3 fraction remains the dominant binding mode at all treatment angles. The sp^2 content also rises to 11% at direct treatment and continues to rise steadily to 19% up to an angle of 60°, remains constant at 120° and then drops to a minimum of 3% until 180°. The C=O fraction decreases at 0° to 10% and then remains in this range. C−O remains below 5% up to 120°, with the exception of 30° (7%), and increases to 9% from 150° to 180°. It is observable that from 150°, the proportion of C−O and C=O exceeds that of sp^2. The proportional increase of the O bonds is also observable in the SFE, whose polar component increases strongly at 150° and 180° (Fig. 39). In general, it can be observed that the chemical composition of the surface changes due to the O_2 plasma, which is also angle-dependent, but does not necessarily lead to an excessive number of O bonds.
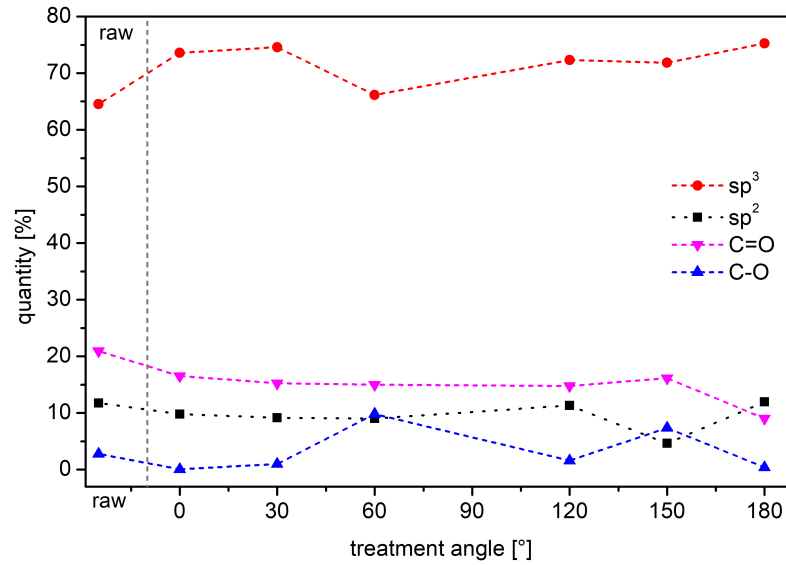
Fig. 42: XPS results given as percentage of appropriate binding types for untreated PLA (first value) and angle dependent O_2 plasma treated PLA surfaces.
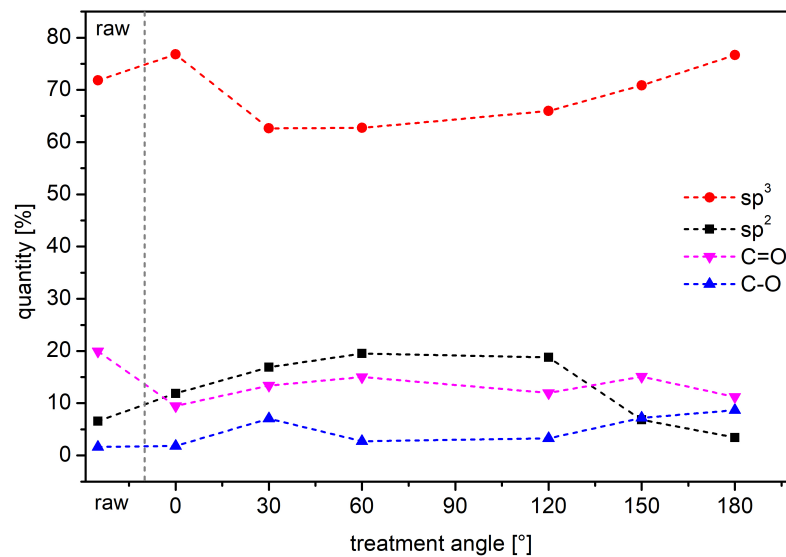

Fig. 43: XPS results given as percentage of appropriate binding types for untreated PHB (first value) and angle dependent O_2 plasma treated PHB surfaces.

7.6. Conclusion

The biopolymers PLA and PHB were treated with variable deposition geometry in a RF-PECVD process with O_2 plasma. The sample surfaces were analyzed for topography with AFM and for their chemical composition by synchrotron supported XPS. Likewise, the barrier property was determined by WVTR and the SFE and CAH by contact angle analysis. Treating PLA shows most of the structure is exposed in the direct O_2 plasma, which is also visible in the roughness factors. As the angle increases, less structure is exposed and the roughness successsively decreases until it reaches the value of the starting material at 180°. PHB shows linear structures that do not change due to the plasma process. With a few exceptions, the roughness remains very similar here. The polar fraction of the SFE increases

by O_2 plasma in both materials. This effect is greater with PLA than with PHB, but not substrate dependent with direct treatment at 0°. It is only during indirect treatment that the differences between the materials become clear. While PLA shows a slight decrease of the polar fraction at high angles, PHB shows an increase. The disperse fraction also changes and initially decreases with direct O_2 plasma treatment and increases again with the indirect angles. The O_2 plasma treatment of PHB and PLA lowers the mobility of a water droplet. It turns to be angle dependent; the mobility increases with increasing angle for direct treatment up to 60° and decreases again slightly for indirect treatments. This correlates with the decrease of the SFE polar fraction and a reduction of surface roughness. The appearance of a barrier property for PLA when the surface is O_2 plasma treated is demonstrated here. Thus, not only cleaning and activation processes are attributed to this treatment, but also changes in the morphological composition of the PLA surface, which improve the barrier property. Furthermore, recombination is believed to narrow pores occurring in PLA. In contrast, an increase in transmittance properties is observed for PHB, which is assumed to originate from rising erosion of the surface. The XPS evaluation shows that there is only little change in the basic chemical composition. The predominant dominance of sp^3 in untreated PLA and PHB is maintained and varies only slightly. In PLA it could be shown that the percentage of $C-O$ bonds exceeds that of sp^2, apart from 180°. In PHB, a different behavior is observed; here the $C{=}O$ fraction exceeds that of sp^2 only from 150°. The $C-O$ bonds are detectable in all samples in small numbers except for PHB at 150° and 180° where they are more than the sp^2 fraction. The chemical arrangement of the surface clearly changes due to the angle-dependent O_2 plasma treatment, which, however, does not immediately lead to a higher number of O bonds at the surface.

7.7. Author contributions

Conceptualization of the study, developing and organization of processes was arranged by L.B. and C.B.F. L.B. designed the experimental set up, prepared the samples and performed the data acquisition and evaluation of XPS, NEXAFS, AFM, CA, and WVTR results. L.B. also arranged the overall data curation, visualization and wrote the manuscript draft. T.S. and K.R. contributed in the acquisition of synchrotron measurements. L.B., T.S. and C.B.F. validated the results; all authors reviewed and edited the manuscript. Both S.W. and C.B.F. contributed in terms of funding acquisition, project administration, supervision and overall guidance in the study.

7.7.1. Declaration of competing Interest

The authors declare that they have no known competing financial interests or personal relationships that could have appeared to influence the work reported in this paper.

7.7.2. Acknowledgements

7.7.3. Supplementary materials

Supplementary material associated with this article can be found, in the online version, at doi:10.1016/j.surfin.2022.101856.

7.8. References

[1] A.L. Andrady, M.A. Neal, Applications and societal benefits of plastics, Philos. Trans. R. Soc. B 364 (2009) 1977–1984, https://doi.org/10.1098/rstb.2008.0304.

[2] S. A. Ruellan, A. Guinault, C. Sollogoub, G. Chollet, A. Ait-Mada, V. Ducruet, Domenek, Industrial vegetable oil by-products increase the ductility of polylactide, eXPRESS, Polym. Lett. 9 (2015) 1087–1103, https://doi.org/10.3144/ expresspolymlett.2015.98.

[3] Y. Tokiwa, B.P. Calabia, C.U. Ugwu, S. Aiba, Biodegradability of plastics, Int. J. Mol. Sci. 10 (2009) 3722–3742, https://doi.org/10.3390/ijms10093722.

[4] L.-.T. Lim, R. Auras, M. Rubino, Processing technologies for poly(lactic acid), Prog. Polym. Sci. 33 (2008) 820–852, https://doi.org/10.1016/j. progpolymsci.2008.05.004.

[5] J. Wong, et al., Current Developments in Biotechnology and Bioengineering, Elsevier, Amsterdam, Netherlands and Cambridge, MA, United States, 2017.

[6] P. Couderc, Y. Catherine, Structure and physical properties of plasma-grown amorphous hydrogenated carbon films, Thin Solid Films 146 (1987) 93–107, https://doi.org/10.1016/0040-6090(87)90343-9.

[7] J. Robertson, Plasma deposition of diamond-like carbon, Jpn. J. Appl. Phys. 50 (2011) 01AF01, https://doi.org/10.1143/JJAP.50.01AF01.

[8] J. Robertson, Diamond-like amorphous carbon, Mater. Sci. Eng. R 37 (2002) 129–281, https://doi.org/10.1016/S0927-796X(02)00005-0.

[9] A. Grill, Plasma-deposited diamondlike carbon and related materials, IBM J. Res. Dev. 43 (1999) 147–162, https://doi.org/10.1147/rd.431.0147.

[10] M. Rohrbeck, S. Körsten, C.B. Fischer, S. Wehner, B. Kessler, Diamond-like carbon coating of a pure bioplastic foil, Thin Solid Films 545 (2013) 558–563, https://doi.org/10.1016/ j.tsf.2013.07.028.

[11] Z.A. Boeva, A. Catena, L. Höfler, S. Wehner, C.B. Fischer, T. Lindfors, Improved water barrier properties of polylactic acid films with an amorphous hydrogenated carbon (a-C:H) coating, Carbon N Y 120 (2017) 157–164, https://doi.org/ 10.1016/j.carbon.2017.05.005.

[12] T. Schlebrowski, L. Beucher, H. Bazzi, B. Hahn, S. Wehner, C.B. Fischer, Prediction of a-C:h layer failure on industrial relevant biopolymer polylactide acide (PLA) foils based on the sp^2/sp^3 ratio, Surf. Coat. Technol. 368 (2019) 79–87, https:// doi.org/10.1016/j.surfcoat.2019. 03.069.

[13] T. Schlebrowski, L. Beucher, H. Bazzi, B. Hahn, S. Wehner, C.B. Fischer, T changing contents of carbon hybridizations in amorphous hydrogenated carbon layers (a-C:H) on sustainable polyhydroxybutyrate (PHB) exhibit a significant deterioration in stability, Depending on Thickness, C 5 (3) (2019) 52, https://doi.org/10.3390/ c5030052.

[14] T. Schlebrowski, H. Acharchi, B. Hahn, S. Wehner, C.B. Fischer, Refinement of sustainable polybutylene adipate terephthalate (PBAT) with amorphous hydrogenated carbon films (a-C:H) revealing film instabilities influenced by a thickness-dependent change of sp^2/sp^3 ratio, Materials 13 (5) (2020) 1077, https://doi.org/10.3390/ma13051077.

[15] C.B. Fischer, M. Rohrbeck, S. Wehner, M. Richter, D. Schmeißer, Interlayer formation of diamond-like carbon coatings on industrial polyethylene: thickness dependent surface characterization by SEM, AFM and NEXAFS, Appl. Surf. Sci. 271 (2013) 381–389, https://doi.org/10.1016/j.apsusc.2013.01.210.

[16] J.T. Korhonen, T. Huht/"amaki1, O. Ikkala, R.H.A. Ras, Reliable measurement of the receding contact angle, Langmuir 29 (2013) 3858–3863, https://doi.org/10.1021/ la400009m.

[17] T. Huhtamäki1, X. Tian, J.T. Korhonen, R.H.A. Ras, Surface-wetting characterization using contact-angle measurements, Nat. Protoc. 13 (7) (2018) 1521–1538, https://doi.org/10. 1038/s41596-018-0003-z.

[18] K.F. Gebhardt, Report: Grundlagen der physikalischen Chemie von Grenzfl/"achen und Methoden zur Bestimmung grenzflächenenergetischer Größen, FhG IGB Stuttgart, 1982.

[19] H.J. Busscher A.W.J. van Pelt, P.de Boer, H.P. de Jong J. Arends, The effect of surface roughening of polymers on measured contact angles of liquids, Colloids Surf 9 (1984) 319–331, https://doi.org/10.1016/0166-6622(84)80175-4.

[20] DIN 53122-1:2001-08, Testing of plastics and elastomer films, paper, board and other sheet materials - determination of water vapour transmission - Part 1: gravimetric method, (2001).

[21] ISO 2528:2017-10, sheet materials - determination of water vapour transmission rate (WVTR) - gravimetric (dish) method, (2017).

[22] A. Nefedov, C. Wöll, Advanced applications of NEXAFS spectroscopy for functionalized surfaces, in: G. Bracco, B. Holst (Eds.), Surface Science Techniques, Springer, Berlin, Heidelberg, 2013, pp. 277–303.

[23] J.L. Solomon, R.J. Madix, J. Stöhr, Orientation and absolute coverage of benzene, aniline, and phenol on Ag(110) determined by NEXAFS and XPS, Surf. Sci. 255 (1991) 12–30,

https://doi.org/10.1016/0039-6028(91)90008-G.

[24] F.C. Tai, S.C. Lee, C.H. Wei, S.L. Tyan, Correlation between ID/IG ratio from visible Raman spectra and sp^2/sp^3 ratio from XPS spectra of annealed hydrogenated DLC film, Mater. Trans. 47 (2006) 1847–1852, https://doi.org/10.2320/ matertrans.47.1847.

[25] P.M. Dietrich, T. Horlacher, P.L. Girard-Lauriault, T. Gross, A. Lippitz, H. Min, T. Wirth, R. Castelli, P.H. Seeberger, W.E.S. Unger, Adlayers of dimannoside thiols on gold: surface chemical analysis, Langmuir 27 (2011) 4808–4815, https://doi. org/10.1021/la104038q.

[26] T. Werder, J.H. Walther, R.L. Jaffe, T. Halicioglu, P. Koumoutsakos, On the water carbon interaction for use in molecular dynamics simulations of graphite and carbon nanotubes, J. Phys. Chem. B 107 (2003) 1345–1352, https://doi.org/ 10.1021/jp0268112.

[27] A. Bismarck, W. Brostow, R. Chiu, H.E. Hagg Lobland, K.K.C. Ho, Effects of surface plasma treatment on tribology of thermoplastic polymers, Polym. Eng. Sci. 48 (2008) 1971–1976, https://doi.org/10.1002/pen.21103.

[28] E. Tomasella, L. Thomas, M. Dubois, C. Meunier, Structural and mechanical properties of a-C:h thin films grown by RF-PECVD, Diam. Relat. Mater. 13 (2004) 1618–1624, https://doi.org/10.1016/j.diamond.2004.01.017.

[29] L. Ostrovskaya, V. Perevertailo, V. Ralchenko, A. Dementjev, O. Loginova, Wettability and surface energy of oxidized and hydrogen plasma-treated diamond films, Diam. Relat. Mater. 11 (2002) 845–850, https://doi.org/10.1016/S0925-9635(01)00636-7.

[30] D.H. Kaelble, Dispersion-polar surface tension properties of organic solids, J. Adhesion 2 (1970) 66–81, https://doi.org/10.1080/0021846708544582.

[31] D. Owens, R. Wendt, Estimation of the surface free energy of polymers, J. Appl. Polym. Sci. 13 (1969) 1741–1747, https://doi.org/10.1002/app.1969.070130815.

[32] W. Rabel, Einige Aspekte der Benetzungstheorie und ihre Anwendung auf die Untersuchung und Ver/"anderung der Oberfl/"acheneigenschaften von Polymeren, Farbe und Lack 77 (1971) 997–1005.

[33] J.O. Hansen, R.G. Copperthwaite, T.E. Derry, J.M. Pratt, A tensiometric study of diamond (111) and (110) faces, J. Colloid Interface Sci. 130 (1989) 347–358, https://doi.org/ 10.1016/0021-9797(89)90114-8.

[34] A. Scholze, W.G. Schmidt, F. Bechstedt, Structure of the diamond (111) surface: single-dangling-bond versus triple-dangling-bond face, Phys. Rev. B 53 (1996) 13725, https://doi.org /10.1103/PhysRevB.53.13725.

[35] S. Falah Toosi, S. Moradi, M. Ebrahimi, S.G. Hatzikiriakos, Microfabrication of polymeric surfaces with extreme wettability using hot embossing, Appl. Surf. Sci. 378 (2016) 426–434, https://doi.org/10.1016/j.apsusc.2016.03.116.

[36] E. Wolfram, R. Faust, In wetting, spreading and adhesion; padday, J. F., Ed.;, academic press: London,NewYork, San Francisco, 1978; pp 213–222.

[37] B. Palai, S. Mohanty, S.K. Nayak, Synergistic effect of polylactic acid (PLA) and Poly(butylene succinate-co-adipate) (PBSA) based sustainable, reactive, super toughened eco-composite blown films for flexible packaging applications, Polym. Test. 83 (2020), 106130, https://doi.org/10.1016/j.polymertesting.2019.106130.

[38] Y. Lee, S. Seo, I. Oh, S. Lee, H. Kim, Effects of O_2 plasma treatment on moisture barrier properties of SiO_2 grown by plasma-enhanced atomic layer deposition, Ceram. Int. 45 (2019) 17662–17668, https://doi.org/10.1016/j. ceramint.2019.05.332.

[39] H.G. Kim, J.G. Lee, S.S. Kim, Surface modification of polymeric substrates to enhance the barrier properties of an Al2O3 layer formed by PEALD process, Org. Electron. 50 (2017) 239–246, https://doi.org/10.1016/j.orgel.2017.07.030.

7.9. Supporting Information

7.9.1. X-ray photoelectron spectroscopy (XPS)

Table 4: Percentage of different C bonds at the C1s peak of angle dependent O_2 plasma treated PLA (see Fig. 42).

treatment angle [°]	sp^2 [%]	sp^3 [%]	C−O [%]	C=O [%]
raw	11.76	64.52	2.79	20.93
0	9.82	73.59	0.07	16.52
30	9.16	74.60	0.99	15.25
60	9.04	66.15	9.82	15.00
120	11.33	72.31	1.60	14.75
150	4.64	71.84	7.36	16.15
180	11.94	75.26	0.41	9.03

Table 5: Percentage of different C bonds at the C1s peak of angle dependent O_2 plasma treated PHB (see Fig. 43).

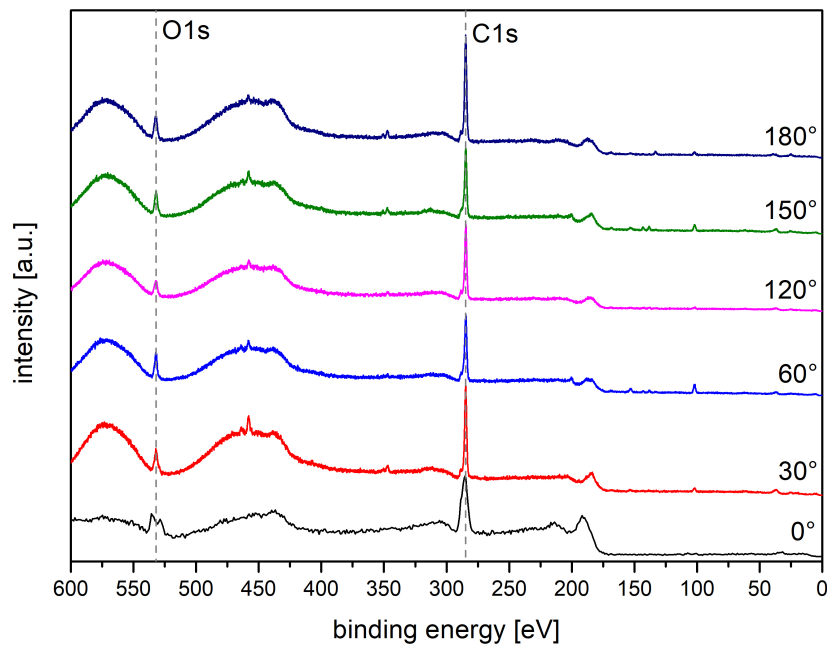| treatment angle [°]	sp^2 [%]	sp^3 [%]	C−O [%]	C=O [%]
raw	6.58	71.82	1.64	19.96
0	11.88	76.81	1.84	9.47
30	16.89	62.65	7.08	13.38
60	19.51	62.74	2.73	15.01
120	18.79	65.95	3.29	11.97
150	6.84	70.87	7.21	15.08
180	3.44	76.66	8.69	11.21

Survey

Fig. 44: XPS survey for angle dependent O_2 plasma treated PLA. Highlighted is the $O1s$ and the later analyzed $C1s$ peak.
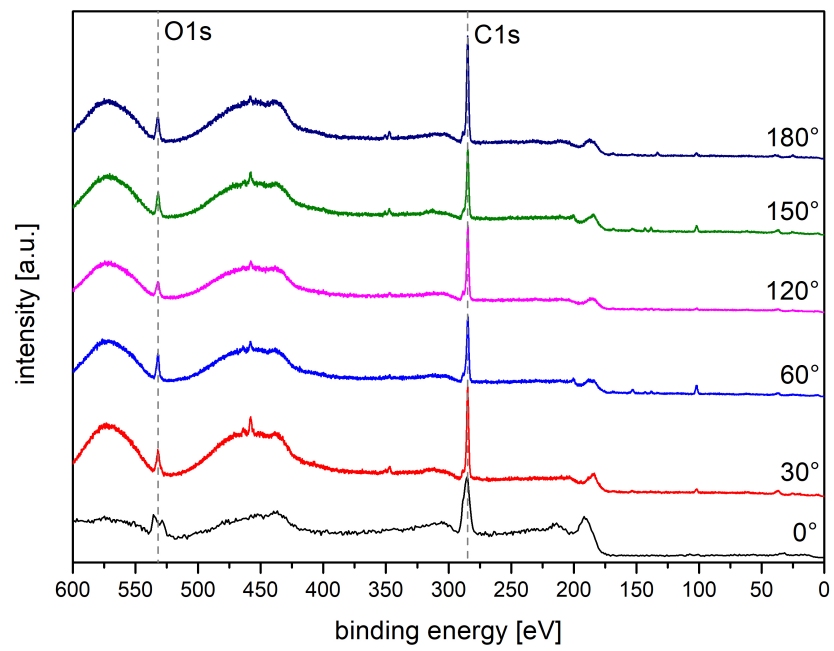
Fig. 45: XPS survey for angle dependent O_2 plasma treated PHB. Highlighted is the $O1s$ and the later analyzed $C1s$ peak.

7.9.2. Near edge X-ray absorption fine structure (NEXAFS)

Before the C- and O-edge measurements, the soiling of the grating and mirror artifacts were determined by a gold edge [1S]. In order to minimize charging effects due to beam irradiation an integrated flood gun is used. To prove the reproducibility and the homogeneity, the C-edges shown here was measured at two different positions. Background noise correction spectra normalizing, smoothing and synchronizing with the ring current decay was performed using Origin8.1Pro. The obtained ratios of the relevant bonds are normalized to the $C = C\pi$ peak by shifting the whole spectrum from the measured position to 284.85 eV [2S-4S].
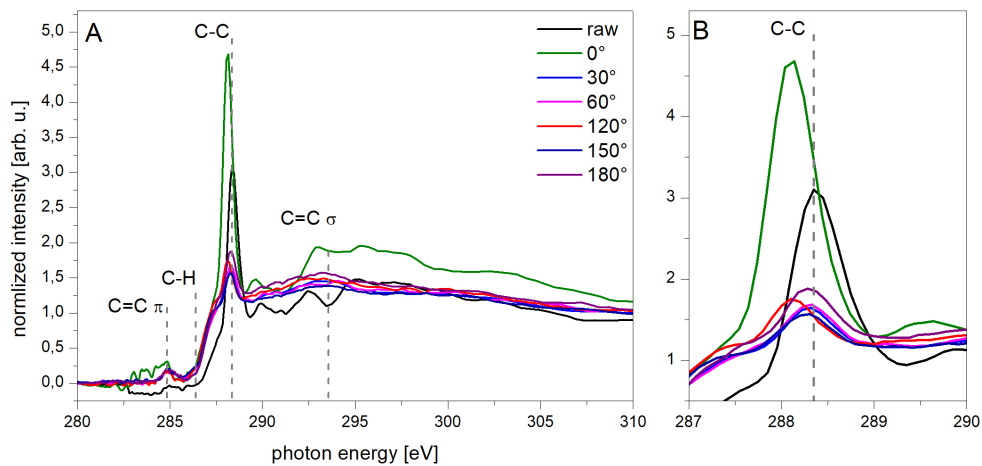

Fig. 46: NEXAS for raw and angle dependent O_2 plasma treated PLA. Fig. A shows the full NEXAFS spectra from 280.0 to 310.0 eV. Fig. B shows a magnification between 287.0 to 290.0 eV for the C−O peak (here: ≈ 288.5 eV).
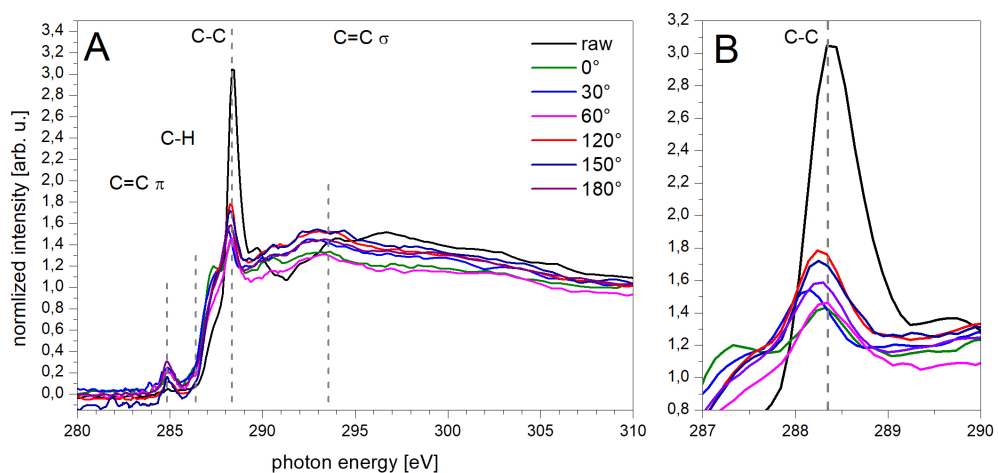

Fig. 47: NEXAS for raw and angle dependent O_2 plasma treated PHB. Fig. A shows the full NEXAFS spectra from 280.0 to 310.0 eV. Fig. B shows a magnification between 287.0 to 290.0 eV for the C−O peak (here: ≈ 288.5 eV).

7.9.3. Atomic force microscope (AFM)

Fig. 48: $5.0 \times 5.0 \ \mu m^2$ AFM images showing untreated (a) and angle dependent O_2 plasma treated PLA for $0°$ to $180°$ (b-g). Fig. 35 is the 3D display.
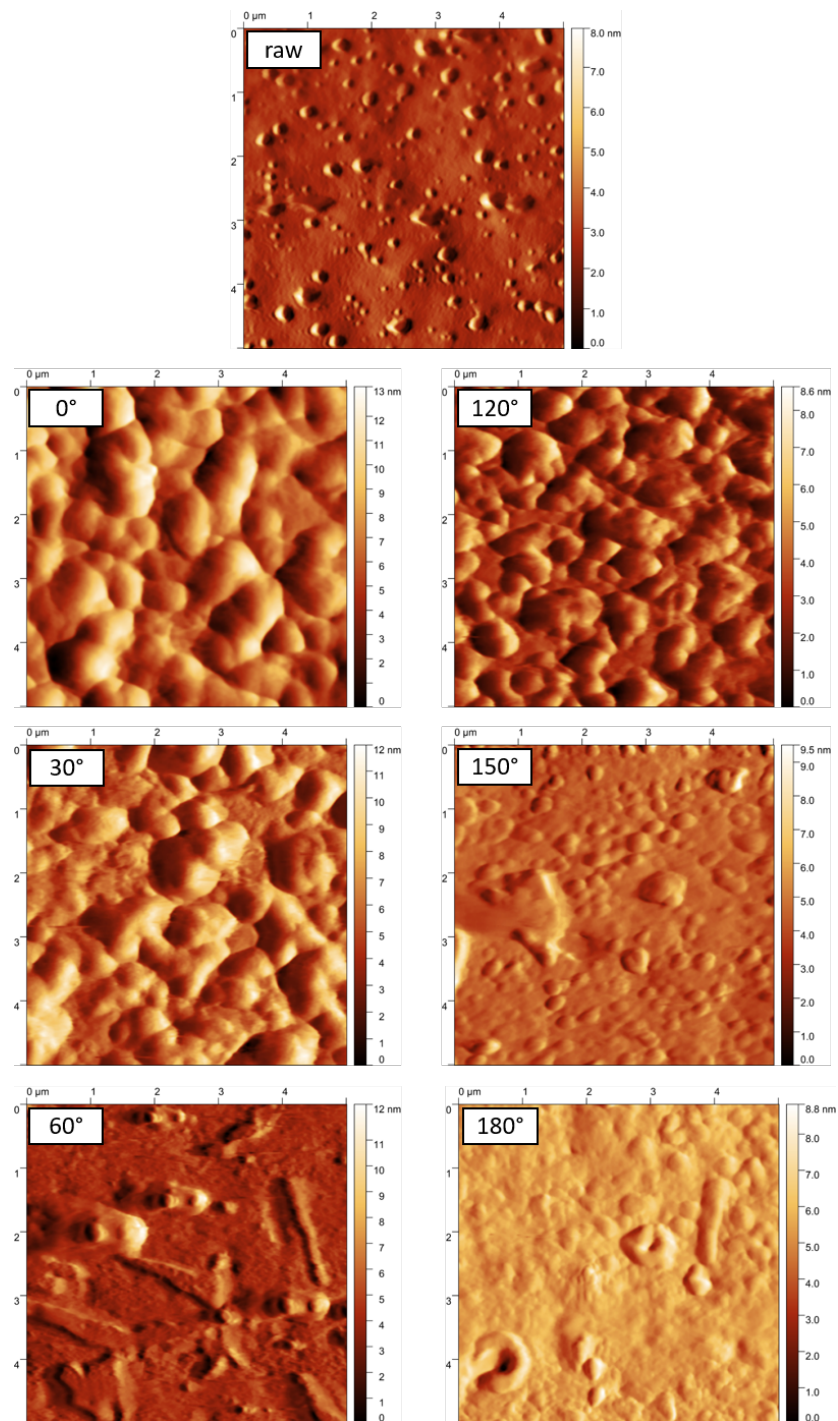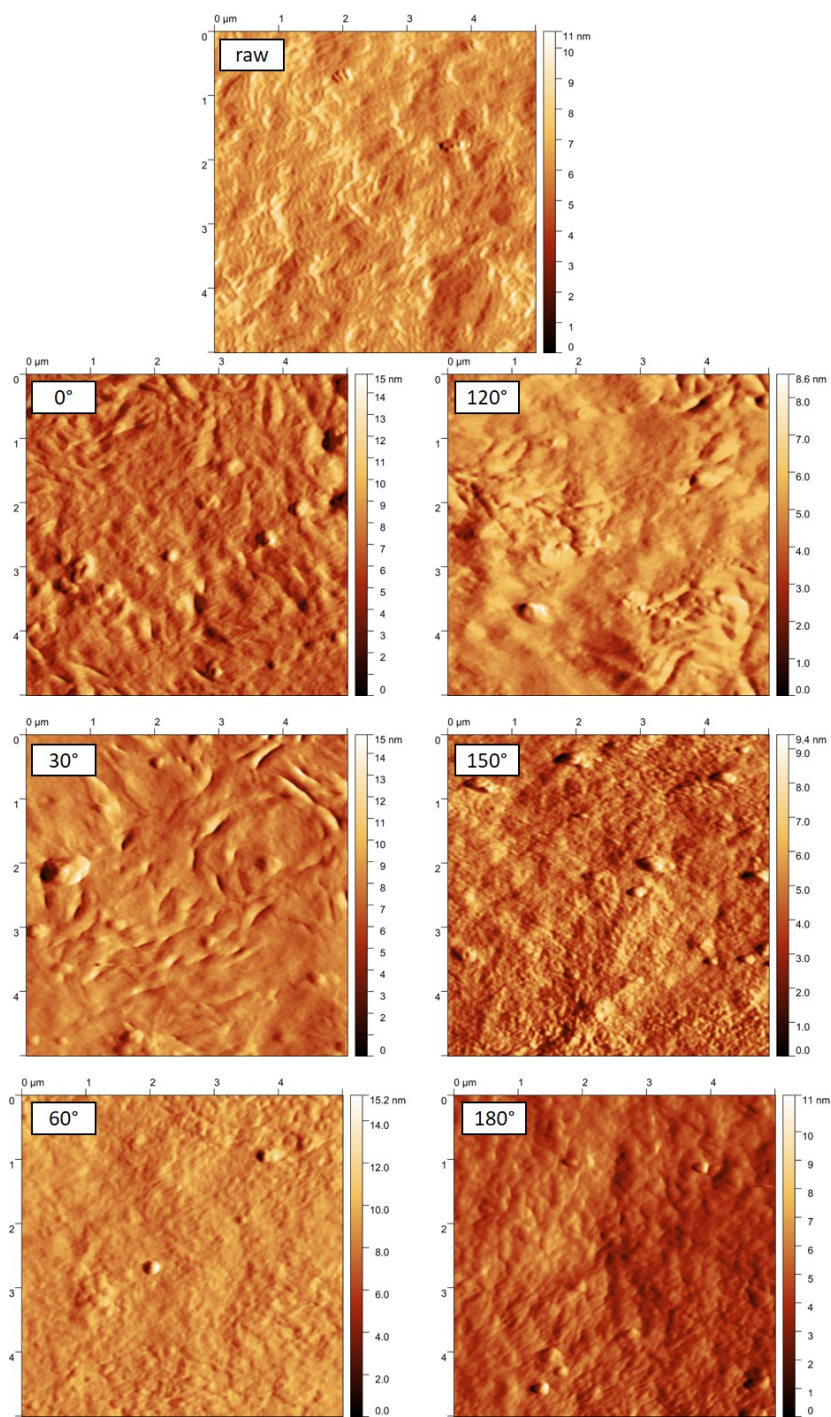
Fig. 49: $5.0 \times 5.0 \ \mu m^2$ AFM images showing untreated (a) and angle dependent O_2 plasma treated PHB for 0° to 180° (b-g). Fig. 35 is the 3D display.

7.9.4. References SI

[1S] B. Watts, L. Thomsen, P.C. Dastoor, Methods in carbon K-edge NEXAFS: experiment and analysis, J. Chem. Phys. 140 (2014) 105–120, https://doi.org/10.1016/j. elspec.2005.11.006.

[2S] J.L. Solomon, R.J. Madix, J. Stöhr, Orientation and absolute coverage of benzene, aniline, and phenol on Ag(110) determined by NEXAFS and XPS, Surf. Sci. 255 (1991) 12–30, https://doi.org/10.1016/0039-6028(91)90008-G.

[3S] F.C. Tai, S.C. Lee, C.H. Wei, S.L. Tyan, Correlation between ID/IG ratio from visible Raman spectra and sp2/sp3 ratio from XPS spectra of annealed hydrogenated DLC film, Mater. Trans. 47 (2006) 1847–1852, https://doi.org/10.2320/matertrans.47. 1847.

[4S] P.M. Dietrich, et.al., Adlayers of dimannoside thiols on gold: surface chemical analysis, Langmuir 27 (2011) 4808–4815, https://doi.org/10.1021/la104038q.

8. Controlling the sp^2/sp^3 ratio of amorphous hydrogenated carbon layers (a-C:H) on polylactide acid (PLA) at constant distance but angle-dependent deposition

This article by Lucas Beucher, Torben Schlebrowski, Melanie Fritz, Stefan Wehner and Christian B. Fischer has been released in *Surfaces and Interfaces* Volume 30, June 2022, 101856 with the DOI: 10.1016/j.apsusc.2023.157450. The paper expands the paper **Surface treatment of biopolymer films Polylactic acid and Polyhydroxybutyrat with angular changing oxygen plasma – More than just gradual purification** and shows the angle-dependent a-C:H coating of different layer thicknesses on PLA surface treated with O_2. The films used were purchased from Goodfellow GmbH, Friedberg, Germany. The plasma coating was carried out at NTTF Coatings GmbH, Rheinbreitbach, Germany by L. Beucher. The measurements and evaluations of CA, AFM morphology and WVTR were carried out by L. Beucher. The SEM images were taken by K. Eshtaya and analyzed by L. Beucher. The synchrotron based X-ray spectroscopy measurements were performed at the Helmholtz-Zentrum Berlin für Materialien und Energie, Berlin, Germany at the beamline of the Karlsruhe Institute for Technology, Group: Chemistry of oxidic and organic interfaces; X-ray and Electron Spectroscopy at Interfaces by L. Beucher, T. Schlebrowski, M. Fritz and C.B. Fischer. The analysis was carried out by L. Beucher. The results were presented and discussed in the Surface Physics research group. The formatting was changed and adapted to the thesis.
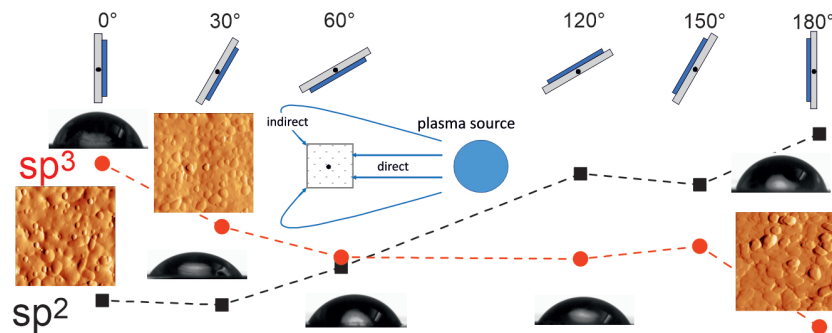
8.1. Graphical abstract

Fig. 50: Graphical abstract of controlling the sp^2/sp^3 ratio of amorphous hydrogenated carbon layers (a-C:H) on polylactide acid (PLA) at constant distance but angle-dependent deposition.

8.2. Abstract

The biopolymer polylactide acid (PLA) is suitable as an eco-friendly substitute for conventional polymers, but polymer surfaces often do not meet industrial requirements and thus severely limit applications. Surface adhesion, substrate related decomposition and barrier permeability can be modified with plasma-deposited thin amorphous hydrogenated carbon (a-C:H) coatings. Their properties depend significantly on the sp^2/sp^3 ratio, here to be controlled by changing the coating geometry between sample and plasma source. A 50 μm PLA film was a-C:H coated at different angle settings (30° intervals) for 2.5, 5.0, 7.5 and 10.0 min to analyze angle-dependent layer growth. Surface morphology was recorded by scan-

ning electron and atomic force microscopy, and the surface free energy (SFE) and contact angle were determined. Modified barrier properties such as the water vapor transmission rate were investigated and showed a reduction in permeability of up to 47% for defined coating geometries and times. In addition, investigations of the top a-C:H layers by synchrotron assisted X-ray techniques revealed angle-dependent changes in the sp^2/sp^3 binding ratio. The angle-dependent coating not only changes the chemical composition of the layer, but also improves the barrier properties and extends the SFE of PLA by an increased polar fraction.

8.3. Introduction

Surface modifications, for example plasma assisted coating processes, which have an even greater impact on surface properties, allow the areas of application to be further expanded and likewise individualized even for polymer materials. Nowadays, as sustainability and environmental compatibility are becoming more and more important in industrial processes and products, biodegradable and bio-based polymers are increasingly used [1]. One of these polymers is polylactide acid (PLA), which is based on corn starch and can be degraded by naturally occurring microorganisms [2-5]. A proven method of coating biopolymers, and PLA in particular, is to deposit a hydrogenated amorphous carbon (a-C:H) layer using radio frequency plasma-induced chemical vapor deposition (RF-PECVD) [6-8]. Deposition on the non- conductive (bio)polymer can be performed in low to high vacuum and at low temperatures [6,9-11]. Each coating is preceded by a 10 minute treatment with O_2 plasma, which has already been performed for PLA in an angle-dependent manner [12]. The surface properties of the a-C:H layer are basically dependent on the chemical composition; especially on its sp^2/sp^3 ratio and the hydrogen content [13-16]. By appropriate variation, different surface properties such as high hardness or low friction can be implemented, which in turn depends multifactorially on the gas composition, gas flow, prevailing pressure and ionization power [13-16]. Another important factor is the coating geometry, which al- lows to control the sp^2/sp^3 ratio. It is known that an a-C:H coating applied directly in front of the source forms sp^3 dominant layers, whereas coatings applied 180° away from the source (indirectly coated) are sp^2 rich [6,11,14,16]. A gradually study of a more or less direct to indirect deposition for these RF-PECVD mediated a-C:H coatings by changing the deposition geometry alone while keeping all other parameters unchanged has not been performed yet. An advantage of this method is that by simply rotating the sample surface to the plasma direction, a change can be induced in respect to deposition thickness and morphology and subtle nuances in surface texture can be achieved that would be more difficult to achieve by parameter changes alone. In the current investigation the sp^2/sp^3 ratio of a-C:H layers on PLA films is therefore to be controlled by an angle-dependent coating, for which different coating thicknesses resp. coating times are also applied. The produced a-C:H layers of different thickness are studied in terms of microscopic and macroscopic impacts. Effects on surface morphology were recorded by scanning electron microscopy (SEM) and atomic force microscopy (AFM). Surface sensitive synchrotron X-ray techniques such as near edge X-ray absorption fine structure (NEXAFS) and X-ray photoelectron spectroscopy (XPS) were used to investigate the chemical composition of the top plasma-fabricated a-C:H layers on the PLA and to confirm the gradually change from sp^3 (0° of deposition) to sp^2 (180°) richer layers. The relation between sp^2/sp^3

ratios and the macroscopic effects was studied by contact angle (CA) measurements and to determine the surface free energy (SFE). The anticipated improvement in barrier properties of the a-C:H coated PLA films was verified by water vapor transmission tests (WVTR).

8.4. Materials and methods

The pretreatment of PLA films (50 μm, Goodfellow GmbH, Friedberg, Germany) is described in detail in reference [12]. Therefore just briefly: PLA pieces of 10×5 cm are distanced in a self-made rotator device with its pivot point 275 mm in front of the plasma source (see Fig. 51). Samples were treated between 0° (direct) and 180° (indirect) in 30° intervals. Each coating at the respective angular position starts with an O_2 plasma (O_2 purity: 6.0, 1 Pa, 60 $sccm/min$, 200 W) for 10 min [8-10,12] followed by a-C:H deposition with acetylene plasma (C_2H_2 purity: 2.6, 0.65 Pa, 60 $sccm$, 107 W) for 2.5, 5.0, 7.5, and 10.0 min. The respective coating rate is ~ 10 nm/min for the direct and ~ 2 nm/min for the indirect coatings. Please note: According to our previous investigations, no elevated temperature could be detected for the films [6]; no deposits could be realized at 90° and will not be discussed further here [12]. The coating thickness was determined with a profilometer (Dektak 3, Veeco Instruments Inc., Plainview, NY, USA) by half-covering silicon wafers with vacuum-compatible and residue-free removable Kapton$^{©}$ tape (Hi-Temp Masking Tape, Elegoo Inc., China).
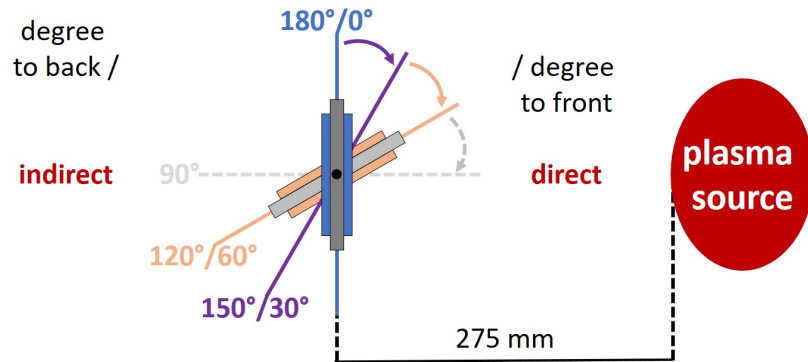

Fig. 51: Schematic representation of the angle-dependent coating process.

The surface of the plasma-treated samples was examined with a scanning electron microscope (SEM515, Phillips, $10 - 20$ kV WD 20 mm). Charging effects could be eliminated by a 17 nm thin gold layer on each sample, ensuring that the imaged surface could be assigned to the a-C:H layer. Further morphological details were investigated using atomic force microscopy (Asylum Research MFP-3D-BIO, Oxford Instruments, Abingdon, UK) by acquiring a 5×5 cm height profile (resp. 512×512 px) at a speed of 5 $\mu m/s$ using AC240TS cantilevers (Oxford Instruments, Abingdon, UK) in contact mode at ambient conditions. Images, at least from three different positions to ensure homogeneity, were analyzed and processed using Gwyddion 2.58 (GNU General Public License), whereby artifact smoothing and noise suppression was achieved via filters with a mean, median, and conservative noise reduction of 3 px each. Respective 3D graphics show deflection retrace, whereas roughness R_a and R_q were determined from height retrace. The surface wettability was studied with a contact angle goniometer (OCA 15EC, DataPhysics Instruments GmbH, Filderstadt, Germany) with

1 μl of distilled water dispensed onto the surface under ambient conditions (sessile drop technique). Contact angles were determined at five different unoccupied locations to obtain a representative average value of the surface wettability. The surface free energy (SFE) was determined indirectly by observing dispersive as well as polar interactions with the CA-analysis of five different liquids (water, diiodo- methane, 1-bromonaphthalene, formamide, and ethylene glycerol, each of HPLC quality) followed by the Owens, Wendt, Rabel and Kaelble method (OWRK). The dispersive forces (e.g., hydrocarbons) and polar forces (e.g., water) are determined between temporarily occurring asymmetric charge distributions. The respective polar (γ_p) and dispersive (γ_d) fractions of the solvents are described in the literature [17,18]. With the W3/031 Water Vapor Transmission Rate Tester from Labthink (Labthink GmbH, Neu-Isenburg, Germany) barrier properties are examined according to DIN 53122-1 / ISO 2528:2017 (area normalized to 1 m^2 and 24 h) [19,20]. Here, the sample is clamped in a homemade adapter (test area: 4.91 cm^2) with the coated sample surface facing the water reservoir (10 ml deionized water, 38°C and 90% relative humidity difference) [19,20]. After a test interval of 90 min the water loss is automatically determined by weighing. The procedure was repeated four times per measurement and twice per coating angle. The top surface composition with carbon and oxygen was analyzed with X-ray photoelectron spectroscopy (XPS) and near-edge X-ray ab- sorption fine structure (NEXAFS) at the synchrotron facility of the Helmholtz-Zentrum Berlin at beamline HE-SGM [21] in the low alpha mode (ring current max. 100 mA, decay mode). XPS was recorded at two different positions between 600 and 0 eV (measured from 700 to 0 eV) with a resolution of 0.1 eV. The C1s peak was analyzed using CasaXPS software (v 2.3.18, Casa Software Ltd., United Kingdom), and the pro- portions of sp^2, sp^3, C−O, and C=O bonds were assigned and evaluated [22-24]. In addition, the decrease of the O1s peak in the layers was monitored. NEXAFS was used to measure the C- and O-edge; a correction for background noise was performed, and the spectra were shifted to the C=C π-peak, normalized, and smoothed (see also SI). Subsequently, the C=C σ, C−C, and C−H peaks were attributed [21,22,25].

8.5. Results and discussion

The carbon plasma deposition rate by direct coating (0°) was confirmed with profilometry as in previous studies at 10 nm/min [6]. The respective coating times of 2.5, 5.0, 7.5 and 10.0 min resulted in corresponding a-C:H thicknesses of 2.5, 5.0, 7.5 and 100 nm. At the coating angle of 30°, a gradient due to the coating geometry (Fig. 51) was identified. A layer thickness deviation of 10% towards the edges could be observed: At a deposition time of ~ 10 min, the center consists of a 100 nm layer; the edge closer to the plasma source results in a deposition of 110 nm and 90 nm is deposited at the more distant edge. At the coating angle of 60°, the gradient increases to 20%. Therefore, measurements were taken as far as possible in the center. The coating rate for the indirect coating (180°) is reduced to one fifth and could be confirmed to 2 nm/min [6]. This results in coating thicknesses of 5, 10, 15 and 20 nm for the respective times. In contrast to the more direct coating, these thicknesses were also obtained uniformly at the angles of 120° and 150°; whereby a gradient is below the resolution of the profilometer.

The SEM micrographs in Fig. 52 show selected surface structures of raw PLA film (52a), the O_2 plasma treated ones (52a-e), and exemplary the films coated with 10 min a-C:H (52f-i) at different angles. The reference sample 52a shows an evenly roughened surface characterized by isolated particles or bumps, which are associated with dust particles from the ambient air or impurities (additives) already deposited in the production process. Compared to the reference, the 52b appears more pronounced and contrasted after the 10 min direct O_2 treatment. This step mainly serves as cleaning and activation process but also leads to an exposure of production-related structures. This is also visible for the incidence angle of 30° in 52c. From a morphological point of view, the respective opposite angles 150° (52d) and 180° (52e) show a similar but less pronounced structure. It is assumed that the morphology at 60 and 120° also shows similarities to the more directly and indirectly treated surfaces, respectively, and these will be investigated in more detail via AFM. The smaller difference appears with an increasing indirect plasma fraction, where the O_2 ion radiation becomes energetically lower and thus changes the surface less. Compared to the PLA reference 52a or the O_2 treated samples 52b-e, significant morphological changes can be seen for the a-C:H depositions (52f-i). Fig. 52f shows the PLA film 52b after the 10 min a-C:H coating with a resulting layer of 100 nm. Here an overall covering layer is obtained showing no structures of the O_2 plasma cleaning in 52b or the PLA reference film in 52a. However, cracks occur throughout the entire layer, with some of the fracture edges appearing partly straight and smooth, and others partly interlocked, which is contrary to our earlier findings [8]. In addition, a bulging of the layer is visible, which is caused by stress effects for which a sp^3 rich layer is known [6] (see also section 3.5 XPS). After exceeding a critical value of residual stress [16], this leads to the phenomenon of "cord buckling" [28,27] and finally to tearing of the layer. Possible reasons for the occurrence of such stresses may be different expansion or material coefficients of both PLA and a-C:H. Different batches and varying proportions of additives may also cause such effects, especially in direct comparison to previous studies of other batches. Likewise, the a-C:H layer may have formed islands in the early stages of coating growth with corresponding interactions leading to macroscopic deformations [26]. At a coating angle of 30°, the deposited layer has an evenly closed surface structure in which the typical pattern of the embedded raw material is weakly visible. That is, an angle-dependent coating unequal to a frontal coating reduces the internal stress to such an extent that no cracks or cord buckling effects are no longer detected. This is the same for 150° and 180°, even if the coating is significantly thinner within the range of 20 nm. It should be noted that at 180° the O_2 treated surface is mapped most clearly, which is be explained by the indirect coating.
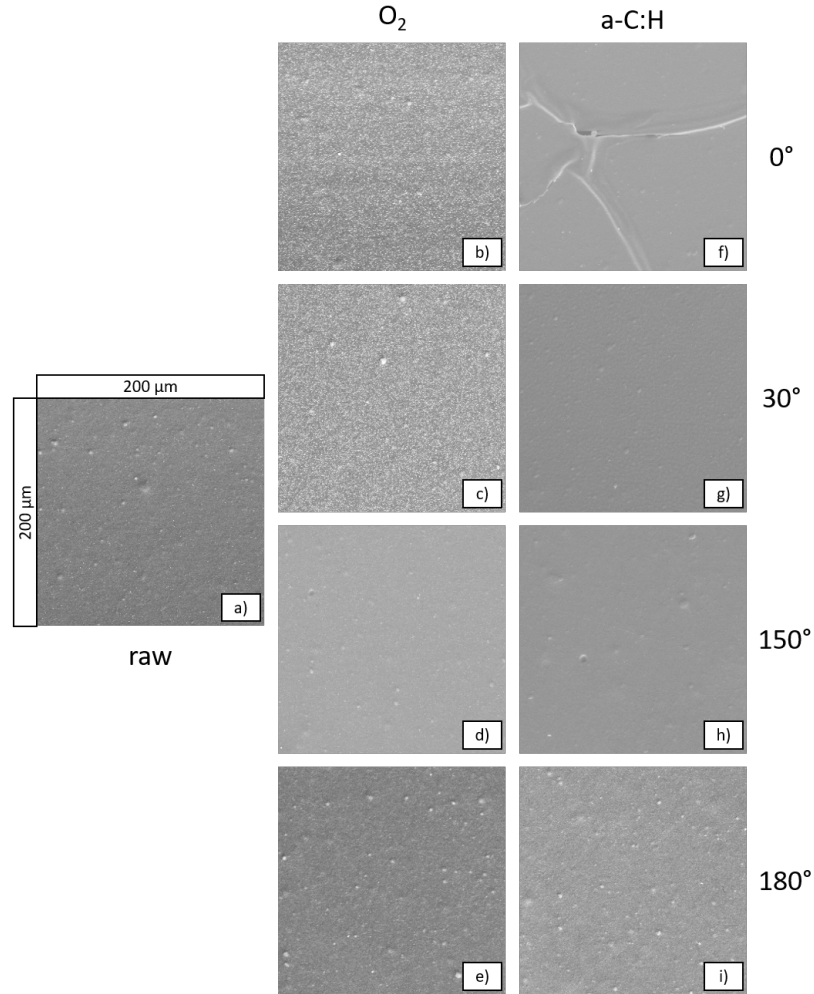
Fig. 52: Selected SEM micrographs of raw (a) and O_2 treated (b-e) PLA films and 10 min a-C:H coated PLA surfaces (f-i) at selected angles.

Fig. 53 shows the surface morphology of PLA films using the example of the 10 min angle dependent a-C:H coating recorded by AFM. The surface treated angular with O_2, as well as the raw PLA film is described in detail elsewhere [12]. The average roughness R_a and the root mean square roughness R_q of these coatings is summarized in Table 6. The surface of the directly deposited (0°) 10 min a-C:H in 53a exhibits in the subsurface the coarse-grained structure $(1-3\ \mu m)$ of the equiangular O_2 cleaned film, with the texture appearing more filled and smoothed. This is also evident in the roughness; if R_a of O_2 treated PLA is 41.9 nm [12], it is reduced to 18.1 nm here (R_q from 51.8 to 23.3). Well formed small grains, which are assigned here to the a-C:H layer, with sizes between 0.1 and 0.5 μm are found on this surface. A similar picture emerges with the 30° coating in 53b. The substrate is fully covered and a similar granular structure is visible, but the contrast is less pronounced. This is also reflected in the increase of the height profile from 11.4 to 17.0 nm and the roughness R_a and R_q to 21.4 and 26.3, respectively. This increasing trend is in contrast to the roughness observed for the O_2 treatment, which decreases with increasing angle [12]. This continues up to the 60° coating: The roughness R_a increases to 28.2 nm and R_q to 34.1 nm with a height profile remaining similar. Morphologically, the previously O_2 treated structure is more prominent here, but the grains are not as pronounced as before (0°/30°) and more widely dispersed.

Therefore, the grain-like structure is more due to the morphology of the O_2 structure. As the angle progresses, this subsurface trend is also observable. Even at 120° (53d), coarse O_2 structures can be seen super- imposed. However, the resulting grain size is much smaller with around 0.1 μm, which is apparent in the decreasing height profile and in lower roughness values, showing that interlayer growth (the transition from the polymeric PLA surface to the applied a-C:H structure [11]) is not yet complete. At 150°, as shown in 53e, few coarse structures from the O_2 treatment are also present [12]. The grain density is higher, but the main pattern remains the same. The height profile stays about the same and roughness values R_a and R_q decrease to 7.6 and 9.8 nm, respectively, due to the lower initial structure and the high, but not pronounced grain structure. For coatings at 180° in 53f, no granular structure is discernible, but a surface morphology similar to that of the O_2 treatment is produced, but it appears smoother and less structured with a similar height profile. However, the roughness here increases again to 11.3 and 15.2 nm for R_a and R_q (8.2 and 11.0 nm for O_2 treatment).
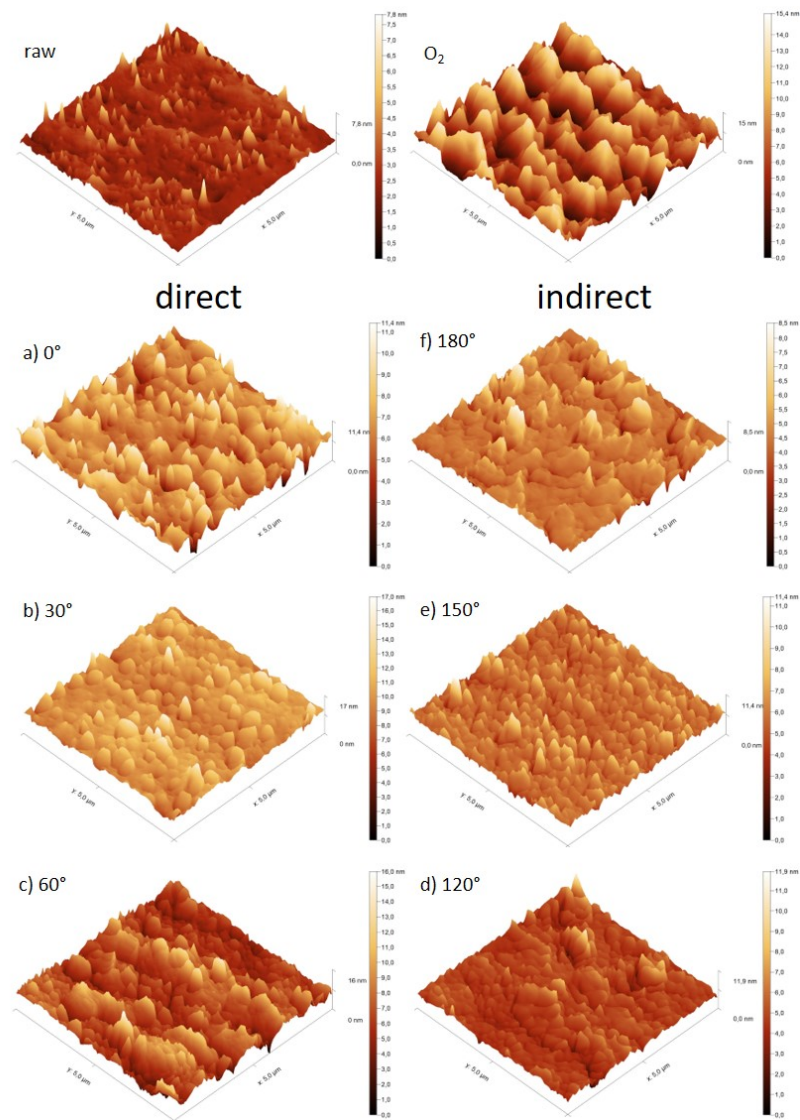

Fig. 53: AFM micrographs of 10 min a-C:H coated PLA samples at angle settings of $0 - 180°$ in 30° steps (a-f). Opposite each other are the respective counter-angles. The first two pictures show the surface of raw and direct O_2 treated PLA [12].

Table 6: Average roughness R_a and the root mean square roughness R_q of 10 min angle dependent a-C:H plasma depositions on PLA films.

coating angle [°]	R_a [nm]	R_q [nm]
0	18.1 ± 4.9	23.3 ± 5.9
30	21.4 ± 4.5	26.3 ± 4.9
60	28.2 ± 3.8	34.1 ± 4.0
120	13.2 ± 3.1	16.5 ± 3.4
150	7.6 ± 2.0	9.8 ± 2.6
180	11.3 ± 4.3	15.2 ± 6.2

8.5.1. Contact angle (CA)

The surface wettability or the resulting CA between the deposited a- C:H surface, the liquid and ambient air results from the combination of surface structure [29-31], chemical bonds [32-36], and the degree of hybridization on the surface [37]. C−H bonds on the surface prevent possible interaction with water [33-36], which results in a hydrophobic layer for hydrated surfaces. However, if the surface contains more oxygen groups or is intentionally oxidized resp. preactivated, this leads to a more hydrophilic character [33]. Moreover, a change in the hybridization states also causes a change in the CA behavior on the sample surface [37]. An sp^3 rich surface has a lower CA than an sp^2 rich a-C:H layer, reasoned by a modified SFE. The low polarity of their free bonds for sp^2 hybridized carbon has a lower surface energy compared to the covalent character of sp^3 bonded carbon [36]. Fig. 54 illustrates the sum of CAs of the different coating times minus the respective reference CA - resulting from the O_2 treatment - over different deposition angles. A negative value indicates a lower CA compared to the reference. The CA values for the respective samples treated with only O_2 plasma are displayed [12]. The first value ($11°\Delta$) shows raw untreated PLA with a CA of 78°, minus the CA of the surface treated with O_2 (at 0°, 67° [12]). It can be seen that the wettability is predominantly reduced by applying the a-C:H layer to the surface previously treated with oxygen and means that oxygen groups are covered. The partially large error deviations make an accurate analysis rather difficult; nevertheless, the following conclusions can be drawn. For the CAs at 5.0 min, a strong fluctuation is evident, which is attributed to interlayer effects [11]. For the remaining coating times, a decrease of the CAs with increasing direct ($0 - 60°$) coating angle can be observed, whereby firstly the initial value is different in each case and secondly the decrease of the CAs is smaller with higher coating times, which indicates a more homogeneously coated surface. For 2.5 min, the CA decreases from $-4°\Delta$, through $-10°\Delta$ to $-18°\Delta$. The CA at 7.5 min is positive, i.e. above the value of the O_2 reference, at about $3°\Delta$ and decreases to $14°\Delta$. For 10 min direct coating, the influencing factor of morphological effects has an impact on the CA and the visible cracks can be responsible for fluctuating CA (see delamination in Fig. 52f). For the time being, it is assumed that the CA is similar for 0 and 30° (approx. $1.5°\Delta$) with a slight descend towards 30° and a larger error bar. For 60°, the CA drops to $8°\Delta$ and remains in the region for 120° in the error analysis. Therefore, the deposited a-C:H layer shows an only slightly fluctuating sp^2/sp^3 hydrogenation ratio. Also for 7.5 min the value between 60° and 120° is almost the same at $-14°\Delta$. For 2.5 min it can be assumed that the CA for $60 - 180°$ is in a very small interval (between $11°\Delta$ and $16°\Delta$),

since the deposited layer can be considered very thin. From the coating angle 120° to 180° and 10.0 min, the CA increases constantly, from about $-1.5°\Delta$ to $3°\Delta$, respectively. In the maximum case (180°), the CA even exceeds the corresponding value of the reference treated O_2. This is due to a higher sp^2 content, which was detected in the XPS analysis (see section XPS). Overall, however, it must be said that there is no uniform surface, so that the CA measurements are prone to error. This increase in CA can also be seen at 7.5 min, where the value changes from $-14°\Delta$ (for 120°) to $-4°\Delta$, so it does not exceed the value of O_2.
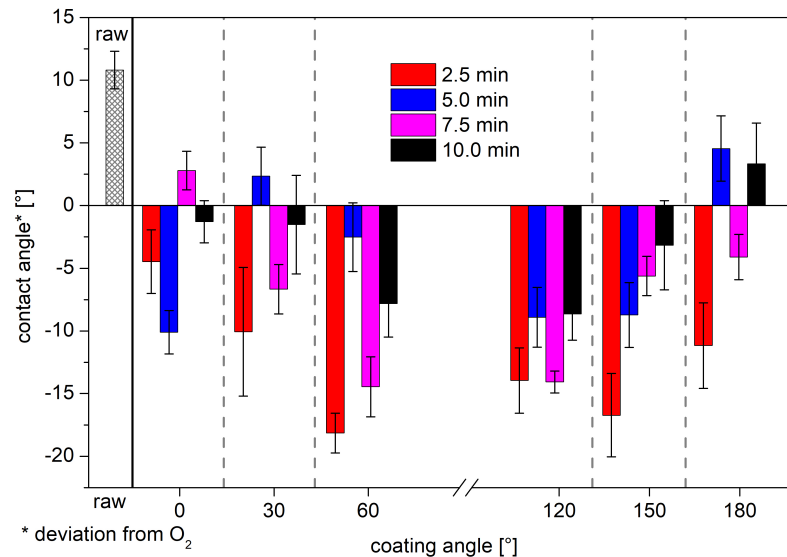
Fig. 54: CA of coating angles from 0° to 180° and treatment times of 2.5, 5.0, 7.5 and 10.0 min minus the respective O_2 reference value. The first gray patterned bar shows the CA for raw untreated PLA (78°). The O_2 treated CA (direct: 67°) is described in detail in [12].

8.5.2. Surface free energy (SFE)

For the coating times of 2.5, 7.5 and 10.0 min, it can be seen in Fig. 55 that the disperse fraction is subject to only small variations of 4 mN/m and can therefore be assumed to be constant at 40 mN/m, which means that a-C:H coating of PLA changes the SFE by only the polar fraction. For direct coating at 2.5 min, the polar content of 8 mN/m increases to 14 mN/m and then decreases slightly to 12 mN/m. Something similar applies for 7.5 min, first increase from 6 to 11 mN/m, then decrease to 8 mN/m, although not as pronounced. However, the total polar fraction is lower, which is consistent with the observation of CAs in Fig. 54. At 10.0 min, no difference can be detected anymore and the range of value is between 12 and 14 mN/m. The indirect coating angles are also similar at 7.5 and 10.0 min. At 2.5 min, the polar fraction is 11 mN/m - similar to 60° - increases to 16 mN/m at 150° and then decreases back to 9 mN/m again, as can also be seen in the CAs (Fig. 54). In contrast, the 7.5 min indirect plasma deposition results in a different pattern, characterized by a steady decrease in the polar fraction from 15 to 11 mN/m, while the disperse fraction can still be considered more or less constant. The increase at 120° could be due to following reasons: a higher concentration of C−C bonds and fewer C−H bonds compared to before, an oxidized surface, or the shining through of O groups through the layer. The decrease at 150° and 180° most likely results from the saturation of dangling bonds by hydrogen, i.e., an

increase in C$-$H bonds, or the increase in sp^2 bonds due to the indirect coating of the surface (see section 3.5 XPS). In comparison, the indirect polar fraction decreases more strongly at 10 min from 14 to 7 mN/m. The lower fraction compared to 7.5 min is also described in the CAs. As with the CA data, considerable variation in SFE is observed at a coating time of 5.0 min, although some values are also in the range of the other coating times. The polar fraction is nearly constant at 10 mN/m for direct coating $(0-60°)$, which corresponds to the increase in the O_2 treated sample; the indirect coatings are also constant at 14 mN/m with a slight increase at 180° (17 mN/m). The dispersed fraction, however, shows strong interval variations from 43 to 35 mN/m, which could indicate that the O_2 surface (30 mN/m) could always shine through the layer, which could be attributed to interlayer effects.
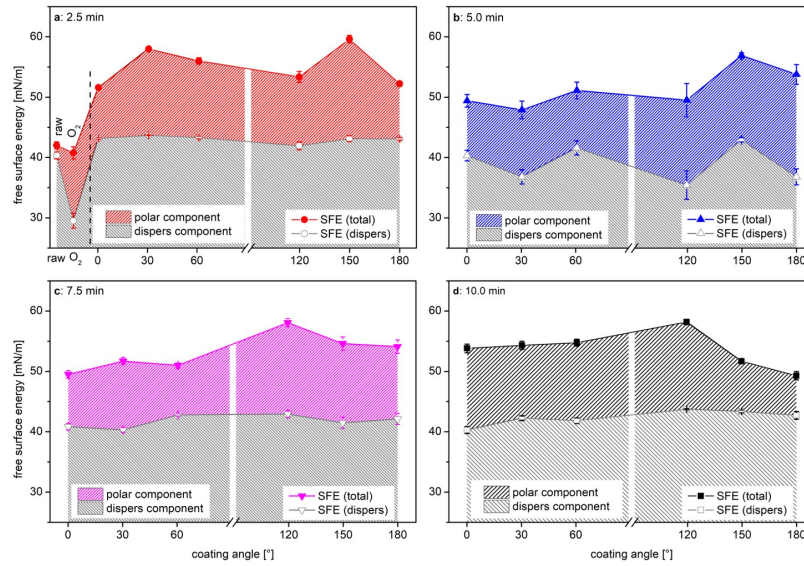
Fig. 55: Time-dependent SFE courses of PLA as a function of the angular direction of the a-C:H deposition. The filled symbols show the course of the total energy, the empty symbols and the gray shaded area show the disperse component. The colored shaded areas show the polar component. Fig. 55a shows the profile for 2.5 min; the first two symbols here represent the raw and the O_2 treated surface, which are described in detail in [12]. These are also the reference for b (5.0 min), c (7.5 min) and d (10.0 min).

8.5.3. Water vapor transmission rate (WVTR)

In Fig. 56, the water vapor transmittance results of the individual coating times are given as subtraction from the respective O_2 plasma treatment values as reference and plotted to the coating angles. A negative permeability thus describes a reduction compared to the reference; a positive value an increase. The first, separated value with 8 $\Delta g/(m^2 \cdot 24\ h)$ shows the permeability of raw, untreated PLA with an averaged value of 122 $g/(m^2 \cdot 24\ h)$ minus the direct O_2 treated result of 114 $g/(m^2 \cdot 24\ h)$ [12]. The higher value compared to the O_2 treated surface shows a decrease in permeability due to the O_2 pretreatment process, which was investigated in detail in [12]. Since the morphology of the surface appears rough and uneven and inclusions from the manufacturing process are present (see SEM Fig. 52b), diffusion of water molecules is obviously favored despite high CAs [6-8]. PLA has also been shown to have process-related channels through which liquid can enter the polymer [6-8]. A 2.5 min coating results in similar values to the O_2 treated surfaces at all coating angles,

with transmittance tending to be slightly improved (down to ca. -4 $\Delta g/(m^2 \cdot 24\ h)$) for direct coatings ($0 - 60°$) and slightly reduced (up to ca. $+10$ $\Delta g/(m^2 \cdot 24\ h)$) for indirect coatings ($120 - 180°$), with a local minimum at $120°$ of $+2$ $\Delta g/(m^2 \cdot 24\ h)$. These values show that a very thin a-C:H layer (less than 25 nm) does not change the barrier effect of PLA much compared to its O_2 treatment. It is assumed that the pores described in [7,12] have not yet been significantly closed. The 7.5 and 10.0 min coatings show a rather similar behavior here for the WVTR. After a direct 10 min a-C:H coating, the WVTR decreases to 39 $\Delta g/(m^2 \cdot 24\ h)$, which corresponds to a reduction of more than 38% compared to the raw PLA. Here, it can be assumed that the barrier property would be better due to the surface coverage in the case of a closed coating in contrast to the observed cracks (see SEM Fig. 52f). Nevertheless, the transmittance is reduced by about 40% with respect to the starting material, confirming the results of Boeva et. al [7] for a 120 nm thick, sp^2 enriched a-C:H coating on PLA. A similar improvement in barrier properties with 31 $\Delta g/(m^2 \cdot 24\ h)$ or 36% reduction compared to the raw PLA is observed with the $30°$ coating. The increase in the error range can be explained by the thickness gradient observed at $30°$. At $60°$, the barrier effect decreases strongly and is at a similar value, as for the sample treated with pure O_2 plasma. From $120°$ to $180°$, a reversal of this phenomenon can be observed. The transmittance after the carbon coating is even greater than after the O_2 plasma treatment. It is suggested that a less pronounced interlayer forms a lower barrier characteristic due to an indirect coating [7] and inverts the reorganization processes suggested in [12] due to the prior O_2 plasma treatment. At 7.5 min, the permeability at $0°$ is reduced to a maximum of 47% reduction or -49 $\Delta g/(m^2 \cdot 24\ h)$. This value again decreases with increasing coating angle up to $60°$ to -12 $\Delta g/(m^2 \cdot 24\ h)$ and is consistently in the positive range for the indirect coatings ($120-180°$). For 5.0 min, an increase in the transmittance of down to 36 $g/2 \cdot 24\ h)$ is observed and an increased error range. The value for $30°$ is with more than 40 $g/(m^2 \cdot 24\ h)$ somewhat higher, but the error range is significantly larger. This again is attributed to the mentioned interlayer properties, which clearly depend on the coating time and the angle setting to the plasma source. For the $60°$ it turns into a positive value of 5 $\Delta g/(m^2 \cdot 24\ h)$ that is also retained in the case of indirect coatings. In summary, the permeability is strongly reduced for the coatings with an angle below $60°$ over all relevant coating times and even re- verses to increase starting at $120°$, which more or less persists until $180°$. In the case of direct coating, it can be seen that the transmittance in- creases with increasing coating time. The slightly reduced permeability at 10 min is also attributed here to the fractured layer (see SEM Fig. 52f). Overall, a change in permeability with increasing coating angle can be observed, with the initial value depending on the coating thickness. However, already from the $60°$ geometry, the permeability is almost at the level of an O_2 plasma treated sample, which constrains the application range for effective permeability characteristics of the coating here to below $60°$.
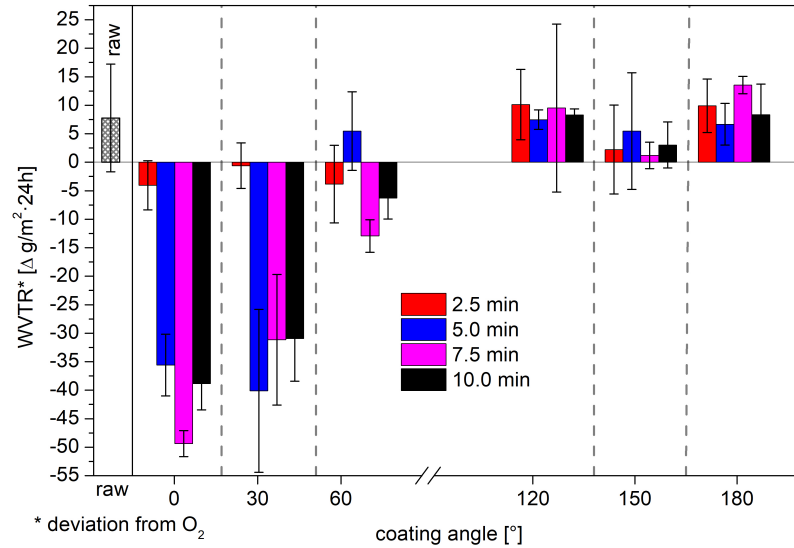
Fig. 56: WVTRs at different angles and different treatment times minus the corresponding O_2 reference transmittance data (described in detail in [12]). The first, gray patterned value shows the corresponding raw PLA result less the O_2 reference value.

8.5.4. X-ray photoelectron spectroscopy (XPS)

The O_2 plasma pretreated PLA surface forms an a-C:H layer as the impinging species from the acetylene plasma react with the rearranged surface and thereby also with the provided O bonds. The resulting bond characteristics can be identified in the respective XPS C1s peaks and are clearly different from the raw and O_2 plasma treated samples [12]. In Fig. 57, the amount of carbon-containing bond states extracted from the C1s signal are displayed in percentage for the sp^2 (a), sp^3 (b), C−O (c), and C−O (d) content, where the quantitative bond fraction is plotted versus the coating angle. The percentages were determined from the corresponding C1s peak (284.80 eV) [22-24]. Up to an angle of 60°, the sp^3 fraction is dominant over all coating times, but decreases successively from its maximum up to 56% at 10 min and about 50% for 2.5 min in the direct coating, in agreement with previous results [8]. In contrast, the proportion of sp^2 bonds increases and is becoming dominant in the indirect coating. The change from sp^3 to sp^2 dominated behavior by direct or indirect coating has already been shown for other polymers such as polyethylene terephthalate [37]. In all samples, oxygen groups are also found as C−O and C−O groups, with the C−O fraction being slightly higher. However, compared to C−C or C=C, both are present in lower amounts. For 2.5 min direct coating the sp^3 content initially remains at over 50%, but then drops to 35% at 60°. At 120° it increases slightly to 35% and drops in the further course continuously down to 28% for 180°, which corresponds to the lowest sp^3 content of the layers. The sp^2 alternates in the interval of nearly 28% for 0°, up to 48% for 120°, and nearly 35% at 180°. The C−O content is, apart from 30° with 3%, between 8 and 15%. The C−O content is around 9% at 0°, 30°, 120° and over 20% at the remaining angles, with a maximum of almost 25% at 150°. For 5.0 min, the sp^2 content increases steadily for direct coatings from 23 to nearly 44%, alternating abruptly between 39% for 120° and 49% for 150°, which was also observed in the CA and SFE data. The sp^3 content decreases steadily from nearly 56% at 0° to 30% at 180°, after an increase at 150° to 42%. The C−O content also alternates strongly

be- tween 19% and less than 1%, as does the C−O content between 2% and 13%. This alternation of bonds is also observed in the CA and SFE analysis and is an indication that a pronounced interlayer behavior is present [8]. For the 10 min deposition time the fraction for sp^3 starts with a maximum of nearly 56% at 0°, drops to 47% at 30°, fluctuates between 60° to 150° from approximately 43% and slightly more than 44% and reaches a minimum of less than 34% at the indirect plasma treatment with 180°. The sp^2 fraction shows the opposite behavior, with minima of 37% at 0° and 30°, respectively. Thereafter, it increases and becomes dominant from a coating angle of 120° to its maximum of nearly 60% at 180°. In the case of direct coating, the content of oxygen groups seems to be more present than for indirect angles. From 0° to 60°, the C−O content increases continuously to about 7%, then is no longer detectable in sufficient quantity until 180°. The C−O content has a similar course. It starts to increase from 7% at 0° to more than 13% at 30° but decreases already at 60° back to 8% and further down to less than 3% for 120° and 150°, respectively. At 180° it increases again to a value of more than 6%. This change in the oxygen groups and the changing chemical environment could be a reason for the shifting peaks in the overview (see SI for survey spectra). Furthermore, it can be seen that fewer O-bonds can be detected compared to the O_2 treated surface and compared to the other coating times, which also explains the lower CAs.
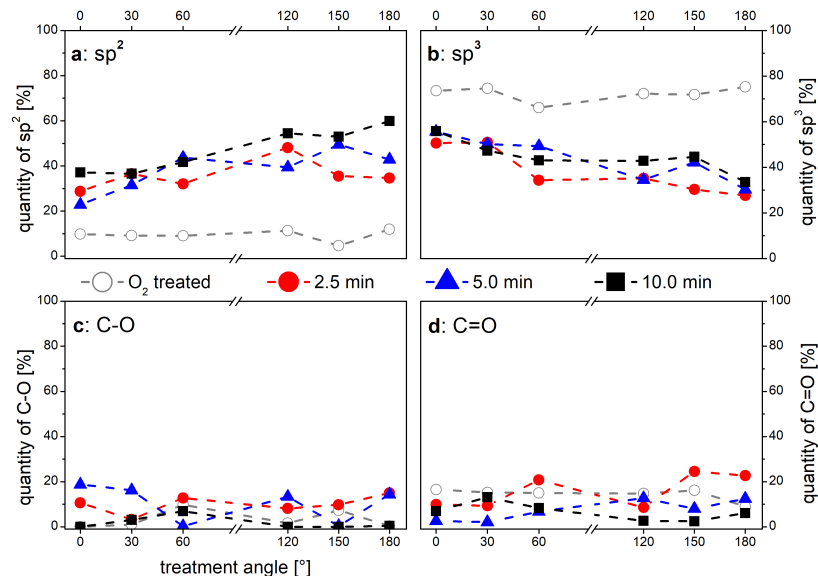
Fig. 57: XPS course of treatment angles from 0° to 180° plus the selected coating times of 2.5, 5.0 and 10.0 min depending on their a) sp^2, b) sp^3, c) C−O, and d) C−O content, respectively. The O_2 plasma treated reference is shown by grey empty circles for completeness [12].

8.5.5. Near-edge X-ray absorption fine structure (NEXAFS)

The NEXAFS spectra are evaluated according to section 2 and normalized to the C=C π to analyze the binding state ratios. Peak positions were determined according to C=C π (284.85 eV), C−H (286.40 eV), C−C (288.35 eV) and C=C σ (292.55 eV) [22,23,38-40] and any shifts were included. In the O_2 treated sample the C−C peak is dominant, this is changed by the 10 min a-C:H coating and the emerging C=C π bond dominates at all coating angles and the C=C σ is filled up. In Fig. 58b it can be seen that the indirectly and directly coated

layers are very close to each other, which is also confirmed by the XPS results. The lower intensity of the indirect layers is attributed to the fact that it is strongly influenced by the O_2 containing surface (Fig. 58a). The C−H signals are very similar over all coating angles, which correlates with the CA and SFE measurements. In Fig. 58c, a decrease in C−C bonds with direct coating is observed with increasing coating angle, although the indirectly coated layer is more intense, which is due to the shining through of the O_2 treated PLA substrate. The indirect peaks are also close together here, with a slight increase at 180°, which is also consistent with the XPS results. The NEXAFS data for the 2.5 and 5 min can be found in the SI.
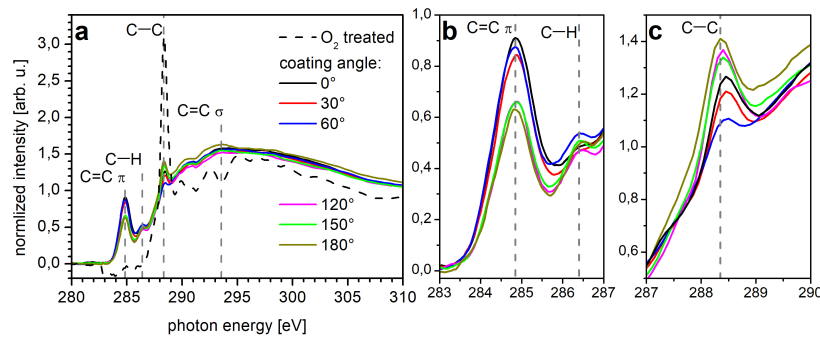
Fig. 58: NEXAS for 10.0 min angle-dependent a-C:H coated PLA. a) shows the full NEXAFS spectra from 280.0 to 310.0 eV including the O_2 plasma treated reference (dotted line). In addition, the O_2 treated surface is shown dashed in black. In b) the C=C π (284.85 eV) and C−H (286.4 eV) peaks are shown between 283.0 and 287 eV. c) shows a magnification between 287.0 and 290.0 eV for the C−C peak (here: $\sim$ 288.5 eV).

8.6. Conclusion

A variable sp^2/sp^3 ratio of a-C:H layers on PLA biopolymer films was achieved by changing the coating geometry using an RF-PECVD acetylene plasma and at different deposition times. SEM images consistently show intact a-C:H depositions except for the frontal coating at 10 min. The AFM images show that the roughness of the layers de- creases compared to the O_2 treated surface. The roughness of the coating itself increases with an advancing angle for the direct coating, which also contributes to the decrease of the CA compared to the O_2 treated films. With the indirect coating, the roughness decreases abruptly and remains at a similar level. The XPS studies confirm for all coating times that sp^3 hybridized bonds dominate for a coating applied at 0°, decreasing with increasing angle to their minimum at 180°. The sp^2 fraction is the opposite, increasing and dominating in the indirect deposition. The sp^2/sp^3 ratio can thus be adjusted with the aid of the appropriate coating geometry and also brings about further changes in the properties. A directly coated sample increases the SFE by the polar fraction. This finding is independent of the coating angle in the case of increasing coating thickness with the direct coating. For the indirect coating, the polar fraction is initially greater for thicker coatings, but then decreases with increasing angle. Alternating bond fractions and SFEs indicate here that interlayer characteristics are present up to a layer thickness of 50 nm (5.0 min for 0°). Regarding the barrier properties, it should be noted that the thicker the a-C:H layer is at the direct depositions the greater the barrier properties are. In particular, the jump in the WVTR from 2.5 to 5.0 min is significant, as

it is assumed that existing pores of the base material are effectively closed. Already at the 30° deposition, the transmission is strongly improved; as the angle progresses the behavior becomes asymptotic and subsequently only low quality barrier proper- ties are observed. In the case of the indirect deposition, the transmission becomes even higher than for the O_2 treated samples. In summary, a window of opportunity for a successful alteration of the sp^2/sp^3 ratio for PECVD mediated a-C:H coatings on the biopolymer PLA films could be provided in terms of deposition time and angle geometry, with the most significant changes in barrier properties with a maximum value of 47% between 0° up to 60°.

8.7. Author contributions

Conceptualization of the study, developing and organization of processes was arranged by LB, TS and CBF. LB designed the experimental set up, prepared the samples and performed the data acquisition and evaluation of XPS, NEXAFS, AFM, CA, and WVTR results. LB also arranged the overall data curation, visualization and wrote the manuscript draft. TS and MF contributed in the acquisition of synchrotron measurements. LB, TS and CBF validated the results; all authors (LB, TS, MF, SW and CBF) reviewed and edited the manuscript. Both SW and CBF contributed in terms of funding acquisition, project administration, supervision and overall guidance in the study.

8.7.1. Declaration of competing Interest

The authors declare that they have no known competing financial interests or personal relationships that could have appeared to influence the work reported in this paper.

8.7.2. Data availability

Data will be made available on request.

8.7.3. Acknowledgements

8.8. References

[1] A.L. Andrady, M.A. Neal, Applications and societal benefits of plastics, Philos. Trans. R. Soc. B 364 (2009) 1977-1984, https://doi.org/10.1098/rstb.2008.0304.

[2] L.T. Lim, R. Auras, M. Rubino, Processing technologies for poly(lactic acid), Prog. Polym. Sci. 33 (2008) 820-852, https://doi.org/10.1016/j. progpolymsci.2008.05.004.

[3] F. Zaaba, M. Jaafar, A review on degradation mechanisms of polylactic acid: Hydrolytic, photodegradative, microbial, and enzymatic degradation, Polym. Eng. Sci. 60 (2020) 2061-2075, https://doi.org/10.1002/pen.25511.

[4] Y. Tokiwa, B.P. Calabia, C.U. Ugwu, S. Aiba, Biodegradability of plastics, Int. J. Mol. Sci. 10 (2009) 3722-3742, https://doi.org/10.3390/ijms10093722.

[5] S. A. Ruellan, A. Guinault, C. Sollogoub, G. Chollet, A. Ait-Mada, V. Ducruet, Domenek, Industrial vegetable oil by-products increase the ductility of polylactide, eXPRESS Polym, Lett. 9 (2015) 1087-1103, https://doi.org/10.3144/ expresspolymlett.2015.98.

[6] M. Rohrbeck, S. Körsten, C.B. Fischer, S. Wehner, B. Kessler, Diamond-like carbon coating of a pure bioplastic foil, Thin Solid Films 545 (2013) 558-563, https://doi.org/10.1016/j.tsf.2013.07.028.

[7] Z.A. Boeva, A. Catena, L. Höfler, S. Wehner, C.B. Fischer, T. Lindfors, Improved water barrier properties of polylactic acid films with an amorphous hydrogenated carbon (a-C:H) coating, Carbon 120 (2017) 157-164, https://doi.org/10.1016/j. carbon.2017.05.005.

[8] T. Schlebrowski, L. Beucher, H. Bazzi, B. Hahn, S. Wehner, C.B. Fischer, Prediction of a-C: H layer failure on industrial relevant biopolymer polylactide acide (PLA) foils based on the sp2/sp3 ratio, Surf. Coat. Technol. 368 (2019) 79-87, https://doi.org/10.1016/j.surfcoat.2019.03.069.

[9] T. Schlebrowski, L. Beucher, H. Bazzi, B. Hahn, S. Wehner, C.B. Fischer, Changing Contents of Carbon Hybridizations in Amorphous Hydrogenated Carbon Layers (a- C:H) on Sustainable Polyhydroxybutyrate (PHB) Exhibit a Significant Deterioration in Stability, Depending on Thickness, C 5 (3) (2019) 52, https://doi.org/10.3390/ c5030052.

[10] T. Schlebrowski, H. Acharchi, B. Hahn, S. Wehner, C.B. Fischer, Refinement of Sustainable Polybutylene Adipate Terephthalate (PBAT) with Amorphous Hydrogenated Carbon Films (a-C:H) Revealing Film Instabilities Influenced by a Thickness-Dependent Change of sp2/sp3 Ratio, Materials 13 (5) (2020) 1077, https://doi.org/10.3390/ma13051077.

[11] C.B. Fischer, M. Rohrbeck, S. Wehner, M. Richter, D. Schmeißer, Interlayer formation of diamond-like carbon coatings on industrial polyethylene: thickness dependent surface characterization by SEM, AFM and NEXAFS, Appl. Surf. Sci. 271 (2013) 381-389, https://doi.org/10.1016/j.apsusc.2013.01.210.

[12] L. Beucher, T. Schlebrowski, K. Rohe, C.B. Fischer, Surface treatment of biopolymer films Polylactic acid and Polyhydroxybutyrat with angular changing oxygen plasma - More than just gradual purification, Surf. Interfaces 30 (2022), 101856, https://doi.org/10.1016/j.surfin.2022.101856.

[13] P. Couderc, Y. Catherine, Structure and physical properties of plasma-grown amorphous hydrogenated carbon films, Thin Solid Films 146 (1987) 93-107, https://doi.org/10.1016/0040-6090(87)90343-9.

[14] J. Robertson, Plasma Deposition of Diamond-Like Carbon, Jpn. J. Appl. Phys., 50 (2011) 01AF01, https://doi.org/10.1143/JJAP.50.01AF01.

[15] J. Robertson, Diamond-like amorphous carbon, Mater. Sci. Eng. R 37 (2002) 129-281, https://doi.org/10.1016/S0927-796X(02)00005-0.

[16] A. Grill, Plasma-deposited diamondlike carbon and related materials, IBM J. Res. Dev. 43 (1999) 147-162, https://doi.org/10.1147/rd.431.0147.

[17] K.F. Gebhardt, Report: Grundlagen der physikalischen Chemie von Grenzflächen und Methoden zur Bestimmung grenzflächenenergetischer Größen, FhG IGB Stuttgart, 1982.

[18] H.J. Busscher, A.W.J. van Pelt, P. de Boer, H.P. de Jong, J. Arends, The Effect of Surface Roughening of Polymers on Measured Contact Angles of Liquids, Colloids Surf. 9 (1984) 319-331, https://doi.org/10.1016/0166-6622(84)80175-4.

[19] DIN 53122-1:2001-08, Testing of plastics and elastomer films, paper, board and other sheet materials - Determination of water vapour transmission - Part 1: Gravimetric method, (2001).

[20] ISO 2528:2017-10, Sheet materials - Determination of water vapour transmission rate (WVTR) - Gravimetric (dish) method, 2017.

[21] A. Nefedov, C. Wöll, Advanced applications of NEXAFS spectroscopy for functionalized surfaces, in: G. Bracco, B. Holst (Eds.), Surface Science Techniques, Springer, Berlin, Heidelberg, 2013, pp. 277-303.

[22] J.L. Solomon, R.J. Madix, J. Stöhr, Orientation and absolute coverage of benzene, aniline, and phenol on Ag(110) determined by NEXAFS and XPS, Surf. Sci. 255 (1991) 12-30, https://doi.org/10.1016/0039-6028(91)90008-G.

[23] F.C. Tai, S.C. Lee, C.H. Wei, S.L. Tyan, Correlation between ID/IG ratio from visible Raman spectra and sp2/sp3 ratio from XPS spectra of annealed hydrogenated DLC film, Mater. Trans. 47 (2006) (1847) 1847-1852, https://doi.org/10.2320/matertrans.47.

[24] T. P.M. Dietrich, T. Horlacher, P.L. Girard-Lauriault, T. Gross, A. Lippitz, H. Min, Wirth, R. Castelli, P.H. Seeberger, W.E.S. Unger, Adlayers of dimannoside thiols on gold: surface chemical analysis, Langmuir 27 (2011) 4808-4815, https://doi. org/10.1021/la104038q.

[25] B. Watts, L. Thomsen, P.C. Dastoor, Methods in carbon K-edge NEXAFS: experiment and analysis, J. Chem. Phys. 140 (2014) 105-120, https://doi.org/ 10.1016/j. elspec.2005.11.006.

[26] C.A. Davis, A simple model for the formation of compressive stress in thin films by ion bombardment, Thin Solid Films 226 (1993) 30-34, https://doi.org/10.1016/0040-6090(93)90201-Y.

[27] A.A. Volinsky, Experiments with in-situ thin film telephone cord buckling delamination propagation, Mater. Res. Soc. Symp. Proc. 749 (2002) 72, https://doi.org/10.1557/PROC-

749-W10.7.

[28] H. Mei, R. Huang, J.Y. Chung, C.M. Stafford, H.-H. Yu, Buckling modes of elastic thin films on elastic substrates, Appl. Phys. Lett. 90 (2007), 151902, https://doi.org/10.1063/1.2 720759.

[29] L.Y. Ostrovskaya, Studies of diamond and diamond-like film surfaces using XAES, AFM and wetting, Vacuum 68 (2002) 219-238, https://doi.org/10.1016/S0042- 207X(02)00460-8.

[30] F. Piazza, G. Morell, Wettability of hydrogenated tetrahedral amorphous carbon, Diam. Relat. Mater. 18 (2009) 43-50, https://doi.org/10.1016/j. diamond.2008.09.023.

[31] B.K. Tay, D. Sheeja, S.P. Lau, J.X. Guo, Study of surface energy of tetrahedral amorphous carbon films modified in various gas plasma, Diam. Relat. Mater. 12 (2003) 2072-2076, https://doi.org/10.1016/S0925-9635(03)00192-4.

[32] Y. Zhou, B. Wang, X. Song, E. Li, G. Li, S. Zhao, H. Yan, Control over the wettability of amorphous carbon films in a large range from hydrophilicity to super- hydrophobicity, Appl. Surf. Sci. 253 (2006) 2690-2694, https://doi.org/10.1016/ japsusc.2006.05.118.

[33] T. Werder, J.H. Walther, R.L. Jaffe, T. Halicioglu, P. Koumoutsakos, On the water carbon interaction for use in molecular dynamics simulations of graphite and carbon nanotubes, J. Phys. Chem. B 107 (2003) 1345-1352, https://doi.org/10.1021/jp0268112.

[34] A. Bismarck, W. Brostow, R. Chiu, H.E. Hagg Lobland, K.K.C. Ho, Effects of surface plasma treatment on tribology of thermoplastic polymers, Polym. Eng. Sci. 48 (2008) 1971-1976, https://doi.org/10.1002/pen.21103.

[35] E. Tomasella, L. Thomas, M. Dubois, C. Meunier, Structural and mechanical properties of a-C:H thin films grown by RF-PECVD, Diam. Relat. Mater. 13 (2004) 1618-1624, https://doi.org/10.1016/j.diamond.2004.01.017.

[36] L. Ostrovskaya, V. Perevertailo, V. Ralchenko, A. Dementjev, O. Loginova, Wettability and surface energy of oxidized and hydrogen plasma-treated diamond films, Diam. Relat. Mater. 11 (2002) 845-850.

[37] A. Catena, Q. Guo, M.R. Kunze, S. Agnello, F.M. Gelardi, S. Wehner, C.B. Fischer, Morphological and chemical evolution of gradually deposited diamond-like carbon films on polyethylene terephthalate: from subplantation processes to structural reorganization by intrinsic stress release phenomena, ACS Appl. Mater. Interfaces 8 (2016) 10636-10646, https://doi.org/10.1021/acsami.6b02113.

[38] J. Diaz, O.R. Monteiro, Z. Hussain, Structure of amorphous carbon from near-edge and extended x-ray absorption spectroscopy, Phys. Rev. B 76 (2007), 094201, https://doi.org/10.1 103/PhysRevB.76.094201.

[39] O. Dhez, H. Ade, S. Urquhart, Calibrated NEXAFS spectra of some common polymers, J. Electron Spectrosc. Relat. Phenom. 128 (2003) 85-96, https://doi. org/10.1016/S0368-2048(02)00237-2.

[40] B. Brüster, C. Amozoquen~o, P. Grysan, I. Peral, B. Watts, J.-M. Raquez, P. Dubois, F. Addiego, Resolving inclusion structure and deformation mechanisms in polylactide plasticized by reactive extrusion, Macromol. Mater. Eng. 302 (2017) 1700326, https://doi.org/10.1002/mame.201700326.

8.9. Supporting Information

8.9.1. X-ray photoelectron spectroscopy (XPS)

survey
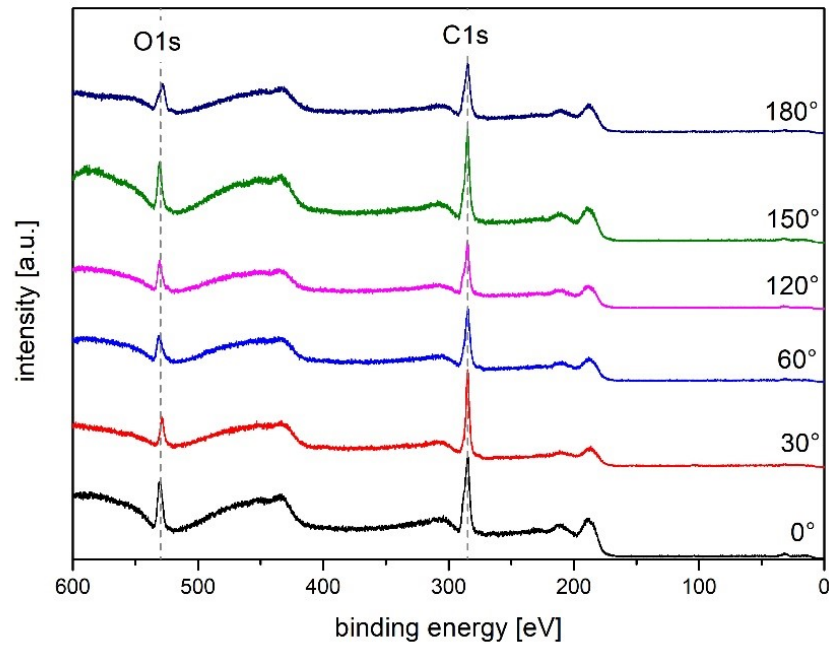
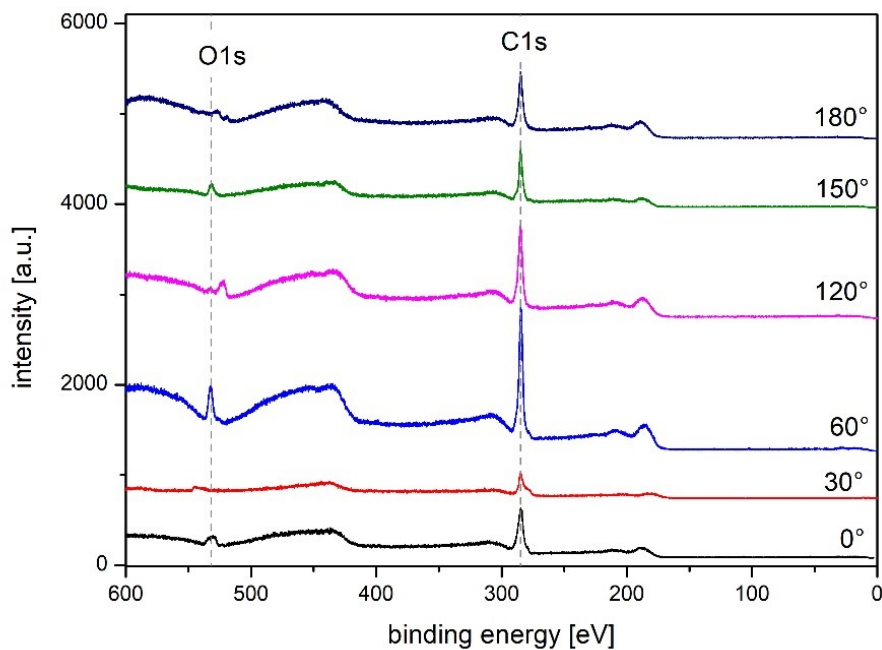**Fig. 59:** XPS survey for angle dependent 2.5 min a-C:H layer on PLA. Highlighted is the $O1s$ and the later analyzed $C1s$ peak.

Fig. 60: XPS survey for angle dependent 5.0 min a-C:H layer on PLA. Highlighted is the $O1s$ and the later analyzed $C1s$ peak.
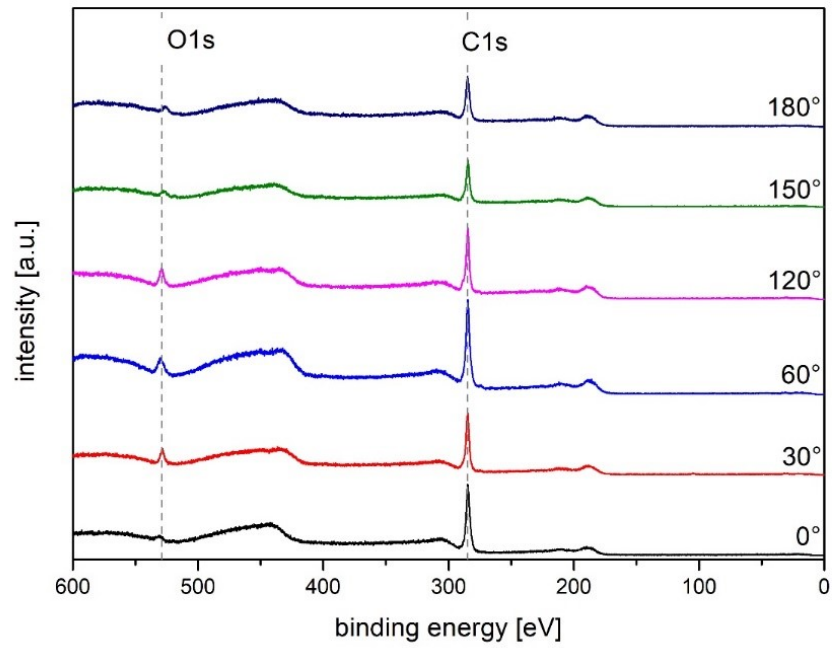
Fig. 61: XPS survey for angle dependent 10.0 min a-C:H layer on PLA. Highlighted is the $O1s$ and the later analyzed $C1s$ peak.

8.9.2. Near edge X-ray absorption fine structure (NEXAFS)

The NEXAFS peaks are determined by [1S-6S] and normalized to the C=C π-peak (284.85 eV). Charging effects were minimized by an integrated flood gun. To ensure reproducibility and homogeneity, the C edges shown here were measured at two different positions on the sample. Grating and mirror artifacts were determined by previously measuring a gold edge [7S,8S], and background noise was normalized with Origin8.1Pro, smoothed, and synchronized with the decay of the ring current.
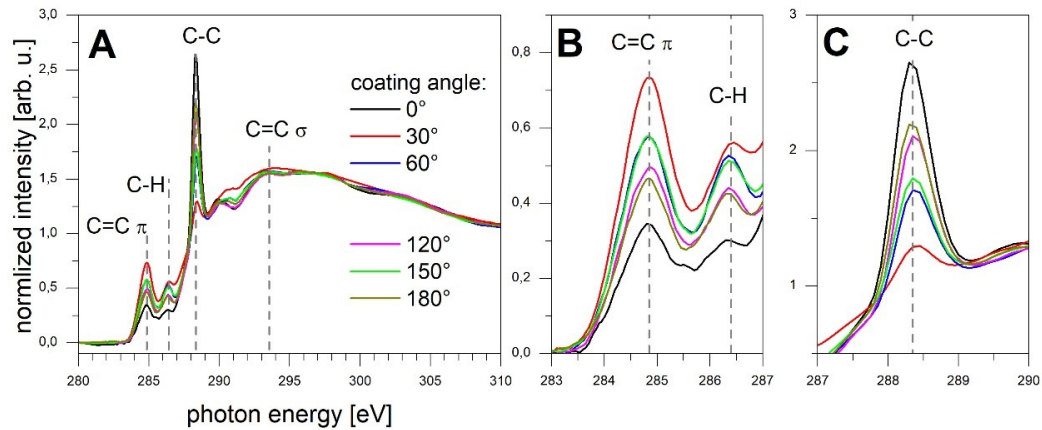
Fig. 62: NEXAS for 2.5 *min* angle dependent a-C:H coated PLA. A shows the full NEXAFS spectra from 280.0 to 310.0eV. In B the C=C π (284.85 eV) and C-H (286.4 eV) peaks are shown between 283.0 to 287 eV. C shows a magnification between 287.0 to 290.0 eV for the C–C peak (here: $\sim$ 288.5 eV).
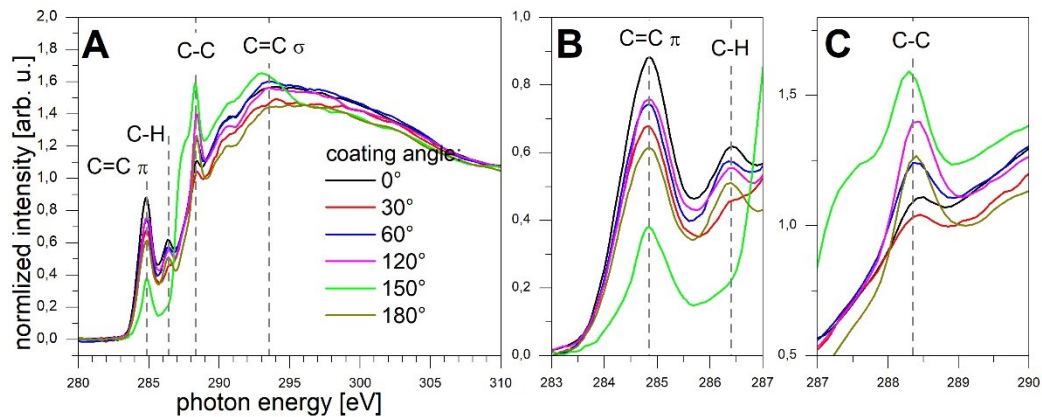
Fig. 63: NEXAS for 5.0 *min* angle dependent a-C:H coated PLA. A shows the full NEXAFS spectra from 280.0 to 310.0eV. In B the C=C π (284.85 eV) and C-H (286.4 eV) peaks are shown between 283.0 to 287 eV. C shows a magnification between 287.0 to 290.0 eV for the C–C peak (here: $\sim$ 288.5 eV).

8.9.3. References SI

[1S] J.L. Solomon, R.J. Madix, J. Stöhr, Orientation and absolute coverage of benzene, aniline, and phenol on Ag(110) determined by NEXAFS and XPS, Surf. Sci. 255 (1991) 12-30, https://doi.org/10.1016/0039-6028(91)90008-G.

[2S] F.C. Tai, S.C. Lee, C.H. Wei, S.L. Tyan, Correlation between ID/IG ratio from visible Raman spectra and sp2/sp3 ratio from XPS spectra of annealed hydrogenated DLC film, Mater. Trans. 47 (2006) 1847-1852, https://doi.org/10.2320/matertrans.47. 1847.

[3S] J. Diaz, O.R. Monteiro, Z. Hussain, Structure of amorphous carbon from near-edge and extended x-ray absorption spectroscopy, Phys. Rev. B 76 (2007) 094201, https://doi.org/10.11 03/PhysRevB.76.094201.

[4S] O. Dhez, H. Ade, S. Urquhart, Calibrated NEXAFS spectra of some common polymers, J. Electron Spectrosc. Relat. Phenom. 128 (2003) 85-96, https://doi.org/10.1016/S0368-2048(02)00237-2.

[5S] B. Brüster, C. Amozoqueño, P. Grysan, I. Peral, B. Watts, J.-M. Raquez, P. Dubois, F. Addiego, Resolving inclusion structure and deformation mechanisms in polylactide plasticized by reactive extrusion, Macromol. Mater. Eng. 302 (2017) 1700326, https://doi.org/10.1002/ mame.201700326.

[6S] P.M. Dietrich, T. Horlacher, P.L. Girard-Lauriault, T. Gross, A. Lippitz, H. Min, T. Wirth, R. Castelli, P.H. Seeberger, W.E.S. Unger, Adlayers of dimannoside thiols on gold: surface chemical analysis, Langmuir 27 (2011) 4808-4815, https://doi.org/10.1021/la104038q.

[7S] B. Watts, L. Thomsen, P.C. Dastoor, Methods in carbon K-edge NEXAFS: experiment and analysis, J. Chem. Phys. 140 (2014) 105-120, https://doi.org/10.1016/j. elspec.2005.11.006.

9. Deposition of amorphous hydrogenated carbon layers (a-C:H) as a function of time and angle: A powerful process to develop surface properties for polyhydroxybutyrate films

This article was written by Lucas Beucher, Torben Schlebrowski, Stefan Wehner and Christian B. Fischer, and has been submitted to *Applied Surface Science* and is in the review process. The article extends the article **Surface treatment of biopolymer films Polylactic acid and Polyhydroxybutyrate with angular changing oxygen plasma - More than just gradual purification** and shows the angle-dependent a-C:H coating of different layer thicknesses on PHB surfaces treated with O_2. The films used were purchased from Goodfellow GmbH, Friedberg, Germany. The plasma coating was carried out at NTTF Coatings GmbH, Rheinbreitbach, Germany by L. Beucher. CA, AFM measurements and evaluations were performed by L. Beucher. The SEM images were taken by K. Eshtaya and analyzed by L. Beucher. The synchrotron-based X-ray spectroscopy measurements were carried out at the Helmholtz-Zentrum Berlin für Materialien und Energie, Berlin, Germany, at the beamline of the Karlsruhe Institute of Technology, Group: Chemistry of Oxidic and Organic Interfaces; X-ray and Electron Spectroscopy at Interfaces by L. Beucher, T. Schlebrowski, M. Fritz and C.B. Fischer. The analysis was carried out by L. Beucher. The results were presented and discussed in the Surface Physics research group. The formatting was changed and adapted to the dissertation.
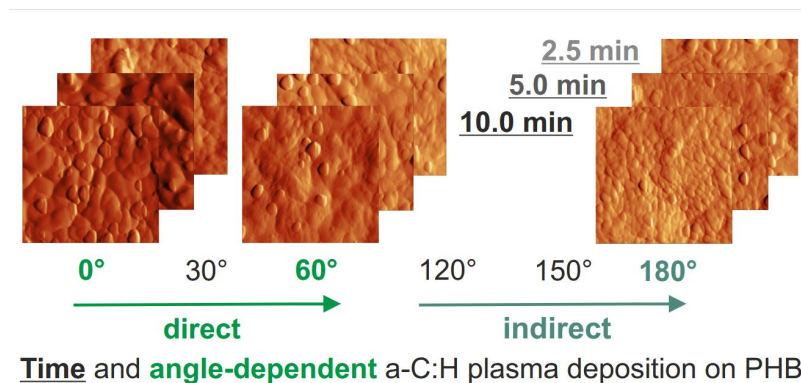
9.1. Graphical abstract

Fig. 64: Graphical abstract of controlling the sp^2/sp^3 ratio of amorphous hydrogenated carbon layers (a-C:H) on polyhydroxybutyrate (PHB) at constant distance but angle-dependent deposition.

9.2. Abstract

Polyhydroxybutyrate (PHB) is a biodegradable polymer derived from renewable raw materials with similar mechanical properties to petrochemical polypropylene. Similar to the latter, the surface properties required for a wide range of applications are demanding and can only be achieved through controlled treatment. Suitable surface modifications can alter the wettability and chemical structure by applying thin layers of amorphous hydrogenated carbon (a-C:H) by low-temperature radio frequency plasmaenhanced chemical vapor deposition. The

surface properties are influenced by the sp^2/sp^3 ratio of the coating, which depends, among others, on the angle of incidence of the plasma on the sample. Accordingly, changing the coating geometry also changes the layer properties. Therefore, a PHB film was coated with a-C:H at different angles and with different thicknesses. Scanning electron and atomic force microscopy recorded the surface morphology, while contact angle goniometry was used to determine the respective hysteresis and surface free energy. It was found that the error range of the contact angle hysteresis decreases with increasing layer thickness. Surface-sensitive, synchrotron-assisted spectroscopy as well as specular reflection IR spectroscopy were used to study the change in the surface chemical structure, detecting angle-dependent changes in the sp^2/sp^3 bond ratio.

9.3. Introduction

Plasma-based surface modifications, e.g. by applying a carbon layer, can be used in an individualized way to expand the already diverse range of applications for polymer films and, for reasons of sustainability and environmental protection, for biopolymer films in particular. One polymer film produced on an industrial scale is polyhydroxybutyrate (PHB). It can be produced by bacterial fermentation [1,2] or by expression in plants [2-4] and serves as an energy and carbon store in various microorganisms, reflecting a high level of sustainability and environmental compatibility [4,5]. The deposition of hydrogenated amorphous carbon (a-C:H) layers by radio frequency plasma-induced chemical vapor deposition (RF-PECVD) is a common technique and the feasibility of depositing a-C:H layers on polymers under vacuum conditions at low temperatures has already been demonstrated [6-8]. It has also been shown that a-C:H can be applied to PHB films [6,9-11], in both direct and indirect (turned away by 180°) coating directions with respect to the plasma source. In direct coating, a distinct interlayer – a mixed layer of the base polymer and the deposited a-C:H – was found up to a layer thickness of 20 nm [11]. The a-C:H layer deposited and the resulting properties are fundamentally dependent on the ratio of sp^2/sp^3 bonded carbon and the corresponding hydrogen content. By changing the sp^2/sp^3 ratio, the surface properties such as high flexibility or low friction can be varied [12,13]. The chemical ratio can be influenced multifactorially, e.g. by the gas composition, the gas flow, the prevailing pressure and the ionization power [12-15]. Furthermore, previous studies have shown that the coating geometry also plays a significant role and that biopolymer films coated directly in front of the source have a higher sp^3 content than those coated indirectly, which are sp^2 richer [6-8]. For instance, it was observed for films of the biopolymer polylactic acid (PLA) that the application of an angledependent a-C:H deposition with different layer thicknesses has a significant influence on the sp^2/sp^3 ratio [8]. Furthermore, it increases the polar part of the surface free energy. However, this proportion was higher with more indirect deposition than with the direct one. In contrast to these findings for the PLA polymer films, a reverse effect is observed when the present polyhydroxybutyrate films are used under equivalent conditions an experimental set-up. The current study demonstrates that the sp^2/sp^3 ratio of different film thicknesses resp. deposition times on PHB can be controlled by an angle-dependent coating and reveals which microscopic and macroscopic surface properties result from this. The main focus is on the investigation of the chemical composition of the top coating, which was determined

by surface-sensitive X-ray-based techniques such as near-edge Xray absorption fine structure (NEXAFS) and X-ray photoelectron spectroscopy (XPS) and by specular reflection infrared spectroscopy (SR-FTIR). The surface morphology was investigated by scanning electron microscopy (SEM) and atomic force microscopy (AFM). Contact angle measurements provide information on the contact angle hysteresis (CAH) – which appears to approach a stationary value with increasing film thickness – and the polar and disperse components of the surface free energy (SFE).

9.4. Materials and methods

The polyhydroxybutyrate films (25 μm) were supplied in industrial quality (Goodfellow GmbH, Friedberg, Germany), cut into pieces of 10×5 cm, clamped in self-made aluminum frames to be mounted in a self-made, rotatable holder. The samples were coated directly (0°) and indirectly (180°), as well as at angles of 30, 60, 120 and 150° with a RF-driven plasma source (13.65 MHz Copra DN 400, CCR GmbH, Troisdorf, Germany). The angular position of 90° was omitted, as no deposits could be detected. During the treatment process, the center point of the holder was always 275 mm away from the source. Fig. 65 shows the schematic arrangement of the plasma source, as well as the fixed angledependent coating positions.
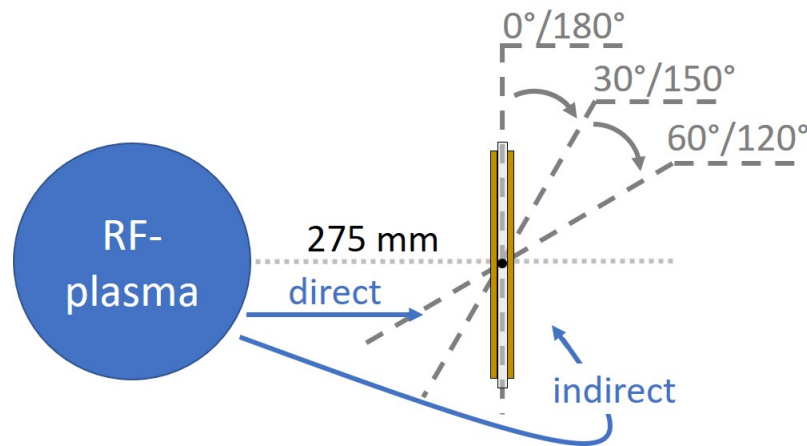
Fig. 65: Schematic of the plasma coating set-up with angle indications. The source distance of 275 mm to the center of the samples is marked with a black dot.

Before applying the main carbon coating, the polymer surface is treated with an O_2 plasma (1 Pa, 60 $sccm/min$, 200 W) according to previous work [16]. The obtained results for this preprocessing of PHB from [16] serve as reference in the following context. The a-C:H was applied subsequently with C_2H_2 plasma (0.65 Pa, 60 $sccm/min$, 107 W) for 2.5, 5.0 and 10.0 min. The deposition rate was 10 nm/min for 0° and 2 nm/min for the indirectly applied layers as described in references [6-8]. The coating thickness and the resulting coating rates were accordingly determined using a profilometer (Dektak 3, Veeco Instruments Inc., Plainview, NY, USA). The morphology was examined using a scanning electron microscope (SEM, SEM515, -lips) with an operating acceleration voltage of $10 - 20$ kV at an average distance of 20 mm. The samples were previously coated with a layer of gold about 17 nm thick to avoid charge effects. Similarly, a height profile of a 5×5 μm area was recorded using atomic force microscopy (AFM, Asylum Research MFP- 3D-BIO, Oxford Instruments,

Abingdon, UK) in contact mode at ambient conditions. The 3D graphs were created with Gwyddion 2.58 and values for the root mean square roughness R_q were determined. The analysis methods of contact angle hysteresis (CAH) and surface free energy (SFE) are based on surface wettability and were investigated with a contact angle (CA) goniometer (OCA 15EC, DataPhysics Instruments GmbH, Filderstadt, Germany) under ambient conditions. The CAH was determined indirectly by subtracting the receding CA (RCA) from the advancing CA (ACA). To determine this, the dosing syringe was positioned directly in a dispensed 1 μl drop of water (HPLC quality) and this was expanded by 5 μl and then reduced again by 4.5 μl. In addition to wettability and surface energy, the CAH also provides information about the surface roughness and adhesion [17-19], as well as the mobility of the droplets. The SFE of the samples was determined indirectly using the Owens, Wendt, Rabel and Kaelble method. For this purpose, a CA analysis of the dispersive and polar interactions of 1 μl with the surface of five different liquids (water, diiodomethane, 1-bromonaphthalene, formamide and ethylene glycerol) was statically investigated [19,20]. The near-surface composition of the C and O compounds was investigated by synchrotron radiation at the Helmholtz-Zentrum Berlin on the HE-SGM beamline in low alpha mode (ring current max. 100 mA) using X-ray photoelectron spectroscopy (XPS) and near-edge X-ray absorption fine structure (NEXAFS) [21]. The XPS spectrum was recorded between 600 and 0 eV with a resolution of 0.1 eV and the proportions of sp^2, sp^3, C=O and C−O bonds of the C1s peak were analyzed and evaluated using CasaXPS software (software version 2.3.18, Casa Software Ltd., United Kingdom) [22-24]. The presence of the O1s peak in the layers was also checked. The C-edge and O-edge recorded by NEXAFS (see SI) were subjected to background noise correction in the course of which they were shifted to the C=C π peak, normalized and smoothed. Subsequently, the C=C σ, C−C and C−H peaks were also identified [21,25,26]. The chemical composition of the a-C:H layers was additionally analyzed by specular reflection infrared Fourier transform spectroscopy (SR-FTIR) (Shimadzu IRPrestige-21 / measuring accessory SRM-8000A, Kyoto, Japan) at ambient conditions. Two ranges of spectra were recorded, each at least at three different locations. Firstly, an overview spectrum from $450 - 4000 cm^{-1}$ ($4 cm^{-1}$ resolution, 100 repetitions) and secondly, a detailed measurement in the C−H stretching range $2800 - 3050 cm^{-1}$ ($1 cm^{-1}$ resolution, 300 repetitions). The spectra were analyzed based on the data of own work [7-11] and references [27-29]. An respective O_2 treated PHB sample was taken here as background and subtracted from each spectrum to record the deposited a-C:H layers separately using the IR Solution-FTIR Control software (software version 1.30, Shimadzu Corporation, Kyoto, Japan). The spectra were then smoothed and the baseline was straightened, which emphasizes the information in the spectrum.

9.5. Results and discussion

9.5.1. Layer thickness and morphology

With direct deposition at 0° in front of the source, a-C:H is deposited at a growth rate of 10 nm/min. Due to the selected coating times, layer thicknesses of 25, 50 and 100 nm are achieved, which are verified by measurements using a profilometer. When changing the coating geometry (see Fig. 65), the layer forms an angle-dependent gradient towards the edges. At a coating angle of 30°, the layer growth is increased by 10% at the edge facing the source

and reduced by 10% at the edge facing away; at 60°, the gradient is ±20%. In the middle, however, the actual coating thickness of 25, 50 and 100 nm is achieved. At a coating angle of 90°, the analysis showed that it was not possible to apply an a-C:H layer, which is why this coating angle is not discussed further. With indirect coating $(120-180°)$, it is noticeable that no gradient formation occurs and the layer grows evenly at a rate of 2 nm/min. Reducing the growth rate by one fifth therefore results in layer thicknesses of 5, 10 and 20 nm for the selected coating times. In Fig. 66 the surface morphology of the differently treated PHB surfaces recorded with SEM are presented. Fig. 66a shows the raw, untreated surface, which has a cloud-like, diffuse texture. Residual particles are recognizable as small white features and damage as fine scratches and roundish indentations, which differ from the rest of the substrate due to their high contrast, are present on the entire surface. After O_2 treatment (66b), the previous cloud-like surface appears much smoother and more homogeneous overall. The number of particles is reduced and indentations in the raw sample are no longer visible. A similar picture can be seen at a treatment angle of 30° (66c). At 180° (66d), the structures of the raw polymer are still very clearly recognizable, even if the indentations appear flatter and the frequency of their occurrence is lower. The cloud-like structure is also smoother, but not in the same way as with direct treatment. After the 2.5 min C_2H_2 plasma treatment (66e), the surface appears similar to that after the O_2 treatment, although the cloud-like structure does not appear as textured, suggesting a thin layer. This can also be observed to the same extent at 30° (66f). At 180° and 2.5 min, the O_2 treated surface is predominantly visible, although it appears sharper and finer (66g). At the 5.0 min treatment, the cloudy structure appears swollen and a layer can be seen at 180° (66j). At 0° (2h) and 30° (66i), a homogeneous smooth surface of a-C:H can be recognized. After 10.0 min at 0° (66k), the surface shows bulges in the covering layer, which are partially closed but also already broken in places. This effect could be due to intrinsic stresses caused by different expansion or material coefficients or layer growth interactions, leading to cord buckling [30]. This phenomena has been already described by the authors in more detail in references [8-10]. Fig. 66l shows that these stress effects and the cord buckling also occur at 30°, but these have not yet caused the coating to break up. With indirect coating (66m) no stress effects can be observed. The surface is completely coated and the cloud-like structure appears sharper and more contrasting.
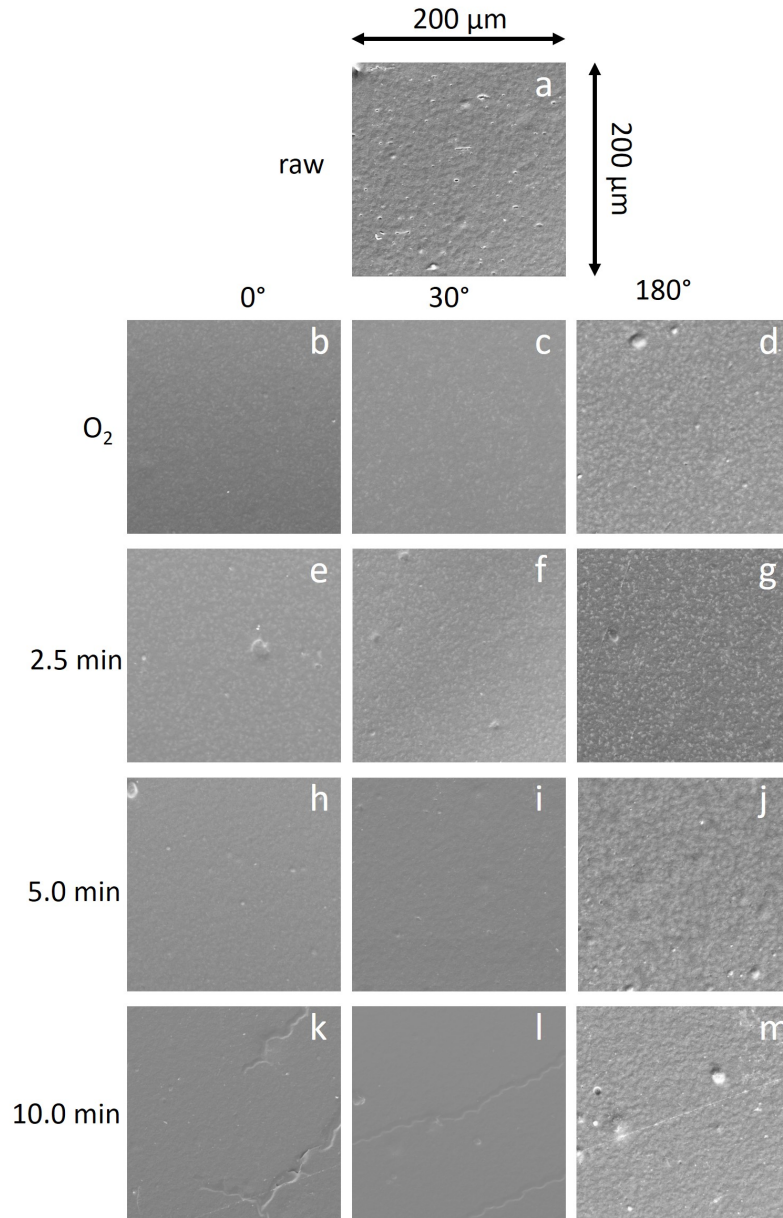
Fig. 66: Selected SEM morphologies of the raw PHB film (a), angle-dependent O_2 treated surfaces (b-d), and coated with a-C:H layers after 2.5 min (e-g), 5.0 min (h-j) und 10.0 min (k-m).

The AFM images of PHB films coated with a-C:H layers at 10 min deposition time and different angles are shown in Fig. 67 (please consult SI for 2.5 and 5.0 min). Tab. 7 summarizes the corresponding R_q values for all angle-dependent and time treatments. Linear elevations ("worm-like structures") can be seen on the raw film (Fig. 67 raw) [6,9]. These were also found after O_2 treatment, where an angledependent treatment does not seem to have any influence, neither on the appearance nor on the roughness according to [16], with a similar roughness value (see Tab. 7) . At 0° grain-shaped structures can be seen, which are coarse structures of up to 1 μm and, building on this, finer grains of approx. 0.25 μm are recognizable. The roughness R_q increases for the 10.0 min direct treated PHB to 37.2 nm compared to the roughness of raw PHB (19.1 nm) and direct O_2 treated one (23.2 nm). As the coating waving progresses, it is noticeable that the coarse-grained substrate structure becomes increasingly less structured. At the same time, the finer on-top grains decrease in frequency and number.

This results in a decreasing roughness from 37.2 nm to 33.3 nm for 30° and 32.5 nm for 60°. The error indication also decreases continuously. With indirect coating, the substrate grain size also appears to cover the entire surface, but is finer ($\sim 0.25 \mu m$) than with direct coating; individual grains of the same size emerge sporadically. However, as the angle increases, the surface shows little change. This can also be seen in the roughness, which is close to each other and shows a similar error, which is smaller in contrast to the direct coating. This is particularly due to the fact that the on-top grains are not or only very slightly present. With increasing layer thickness, it can be observed that the roughness also increases with direct coating. At 0 and 30°, the maximum roughness is at a coating time of 5.0 min, which may be due to interlayer effects that can occur up to a layer thickness of 20 nm according to [11]. For the 10.0 min the roughness values for the direct coatings are consistently more than 30 nm, with a slight decrease in R_q with increasing angles. For the indirect coating, R_q values for the higher angles move around approx. 20 nm, which is lower than for the direct coating and at the same time shows smaller errors. Compared to the results of identical coated PLA films from previous studies of the authors [8], it is noticeable that the error for PHB is usually twice as large. A higher R_q with direct coating and a lower R_q with indirect coating could also be observed with PLA in the same way.
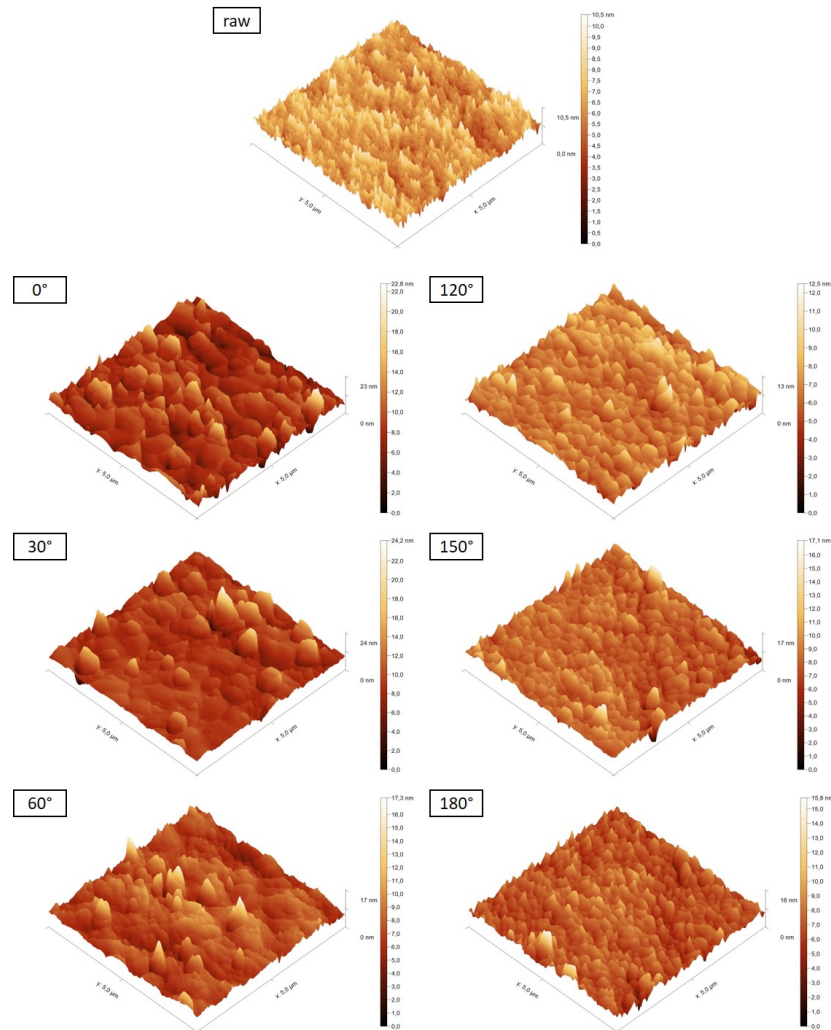
Fig. 67: 3D AFM micrographs of PHB films coated with a-C:H for 10.0min at the selected angle settings of $0 - 180°$ in 30° steps. On top the raw untreated PHB surface is shown.

Table 7: Root mean square roughness R_q values for the 2.5, 5.0 and 10.0 min angle-dependent a-C:H depositions on PHB films, their respective O_2-plasma pretreatment values and the raw substrate.

raw			19.1 $\pm$ 3.7			
	0°	30°	60°	120°	150°	180°
O_2	23.2 $\pm$ 6.9	25.8 $\pm$ 7.0	15.8 $\pm$ 3.0	19.2 $\pm$ 6.4	18.1 $\pm$ 2.4	34.6 $\pm$ 13.3
2.5	23.4 $\pm$ 8.3	31.8 $\pm$ 8.2	21.9 $\pm$ 7.9	28.3 $\pm$ 6.7	24.6 $\pm$ 7.8	19.7 $\pm$ 4.3
5.0	41.4 $\pm$ 5.6	33.7 $\pm$ 11.4	25.2 $\pm$ 8.4	26.2 $\pm$ 12.5	20.7 $\pm$ 7.8	20.2 $\pm$ 7.2
10.0	37.2 $\pm$ 10.9	33.3 $\pm$ 10.4	32.5 $\pm$ 7.5	20.0 $\pm$ 5.8	24.0 $\pm$ 7.0	19.2 $\pm$ 5.3

9.5.2. Chemical composition of a-C:H layers

The PHB surface pre-treated with O_2 plasma (Fig. 68, empty squares) forms the reference for the a-C:H layers of different thickness and geometric variability and is described in detail in an earlier work by the authors [16]. The percentages of sp^2, sp^3, C$-$O and C=O were extracted from the respective C1s signal at 284.80 eV and describe the chemical state of the carbon-containing bonds [22-24]. The data thus provide an indication of the chemical properties of the layer. Initially, sp^3 bound carbon is dominant for all coating thicknesses, but as the angle increases, this proportion decreases successively and there is a change in dominance towards sp^2 bound carbon. The change occurs with increasing layer thickness at smaller angles. The change from sp^3 to sp^2 dominant layers through angle-dependent coating has already been observed with other biopolymers such as PLA [16], and preliminary studies have also shown that indirectly coated conventional polymers exhibit a high sp^2 content in the layer [7]. The C$-$O content of the layer is consistently $< 20\%$, far below the dominant proportions, but higher than the raw polymer (1.6%) and after its corresponding O_2 treatment (1.8%). A noticeable tendency is that the C$-$O bonds decrease with increasing layer thickness and are higher with indirect coating than with direct coating. C=O is less present compared to raw PHB ($< 12\%$), indicating that the C=O bonds present in the PHB are depleted. The value varies differently for the individual layers and only stabilizes after a 10 min coating time, which indicates that there are prior interactions with the polymer surface. At 2.5 min, the sp^3 content appears similar with a slight increase from 0 to 30° and a somewhat steeper drop from 150° to 180°. If the proportion of the raw polymer (sp^3 71.8%) and the O_2 treated surface (sp^3 0° 76.8%) changes only slightly, the sp^3 proportion for the direct coating at 2.5 min is 43.6%, which is significantly lower. This shows that the very thin layer, which is clearly visible in the SEM and AFM (Figs. 66,67), is sufficient to cover the polymer surface somehow by the a-C:H layer. Another reason in the initial stages of such depositions is the formation of an interlayer between the a-C:H and the polymer structure, which has already been shown for a-C:H on PHB [11]. The sp^2 content is lower, but also shows no clear course and appears similar overall. Only at 150° and 180° does the value increase slightly, whereby sp^2 only dominates because the sp^3 content collapses. The C$-$O proportion is higher compared to the other coating times with over 11% - apart from 150° with 9.6%. The value appears to be the same for the frontal coatings and increases for the indirect coatings up to the maximum of 18.6% at 180°. The C=O bonds are significantly reduced at a coating time of 2.5 min in contrast to the raw and O_2 treated surfaces. Here, too, a similar direction of approx. 5%

can be observed with frontal coating and an increase with indirect coating. The course for 5.0 min is clearly different from that for 2.5 min; here the curve for sp^3 is very similar to that for the O_2 treated surface, but the percentages are approx. 10% lower. With indirect coating, the value drops to 29.9% at a coating angle of 120° and then rises again, as with O_2, to 35.9%. The sp^2 curve for direct coating shows a similarly rising curve (up to 44.2%); at 0° the value (16.6%) is again very close to that of the O_2-treated surface (11.9%). The change in dominance takes place between 60 and 120°. The C$-$O curve for 30° and 60° shows the same curve as the O_2 treated surfaces; at 0°, however, more C$-$O bonds are detected. The indirectly coated surfaces show a similar behavior and are around 13%. With C=O, the trend initially continues that the values initially increase on the O_2 surface, but decrease again at 30°, increase again at 120° and then drop again. At 10 min coating, a continuous drop in the sp^3 containing bonds, with a plateau at 60° to 120°, can be observed, while at the same time the sp^2 content increases continuously with a dip at 120°. C$-$O and C=O are at a similar level and alternate in the middle to lower 10% range.
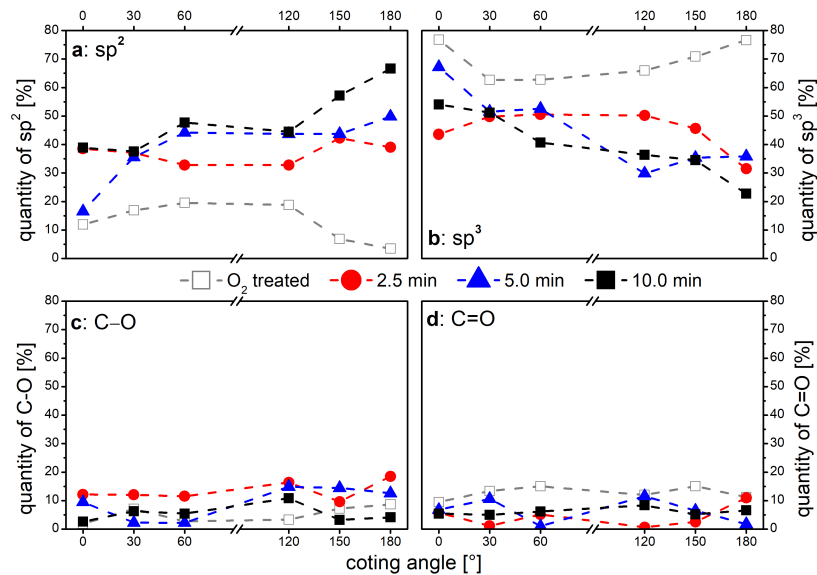
Fig. 68: The course of the treatment angles from 0° to 180° and the selected coating times of 2.5, 5.0 and 10.0 min as a function of their a) sp^2, b) sp^3, c) C$-$O and d) C=O content. For comparison, the corresponding O_2 plasma treated PHB film [16] as reference is shown by empty squares.

The NEXAFS spectra in Fig. 69 show the a-C:H layers deposited on PHB with the 10.0 min angle dependent coating. The peak positions were determined by [22,23,26,31-34] and are 284.85 eV (C=C π), 286.15 eV (C$-$H), 288.35 eV (C$-$C) and 292.55 eV (C=C σ), with all spectra shifted to the C=C π peak. [16] For comparison, the sample treated directly with O_2 is shown as a gray dotted line (respective spectra of raw and angle-dependent O_2 plasma treatments can be found in [16]). In Fig. 69a the entire spectrum is shown; Fig. 69b and c show detailed images of the C=C π and C$-$H peaks, as well as the C=O π and C$-$C peaks. The C$-$C peak at 284.85 eV, which still dominates in the oxygen-treated sample, decreases due to the a-C:H coating, which is also confirmed by the XPS measurement. It is clearly recognizable that the indirectly coated peaks have a more pronounced C$-$C than the directly coated peaks. It can also be seen that the C=C component at 284.85 eV (π) and 293.55 eV

(σ) increases due to the coating and is even more pronounced for the direct coatings than for the indirect ones. Compared to indirect coatings, direct coatings have a higher sp^2 content and a lower C−C content, which is due to the lower layer thicknesses of the indirect coatings. The shift of the peaks is a clear indication of a chemical amorphous surface structure. The absolute intensities are set in relation to each other in order to obtain information independent of the layer thickness. After a-C:H is applied to the O_2 treated PHB surface, the sp^2 to sp^3 ratio increases initially, decreases with increasing coating angle up to 120° and is constant for indirect coating. This implies that the sp^2 proportion, directly coated, decreases to a greater extent than the C−C proportion. However, it remains similar for indirect coating. At 150° it can be seen that the C−C peak is clearly shifted in comparison to the other spectra. The C−H peak (Fig. 69b) becomes more pronounced when the a-C:H layer is applied; if it still appears as a shoulder on the O_2 treated surface, it can then be clearly seen as a peak. It is noticeable that the indirectly coated C−H peaks stand out more clearly than the directly coated ones, with similar intensities for both indirect and direct coatings. The pronounced C=O π peak of the O_2 treated sample (Fig. 69a,c) is strongly attenuated when the a-C:H layer is applied, but can also be found as a shoulder on the coated surfaces.
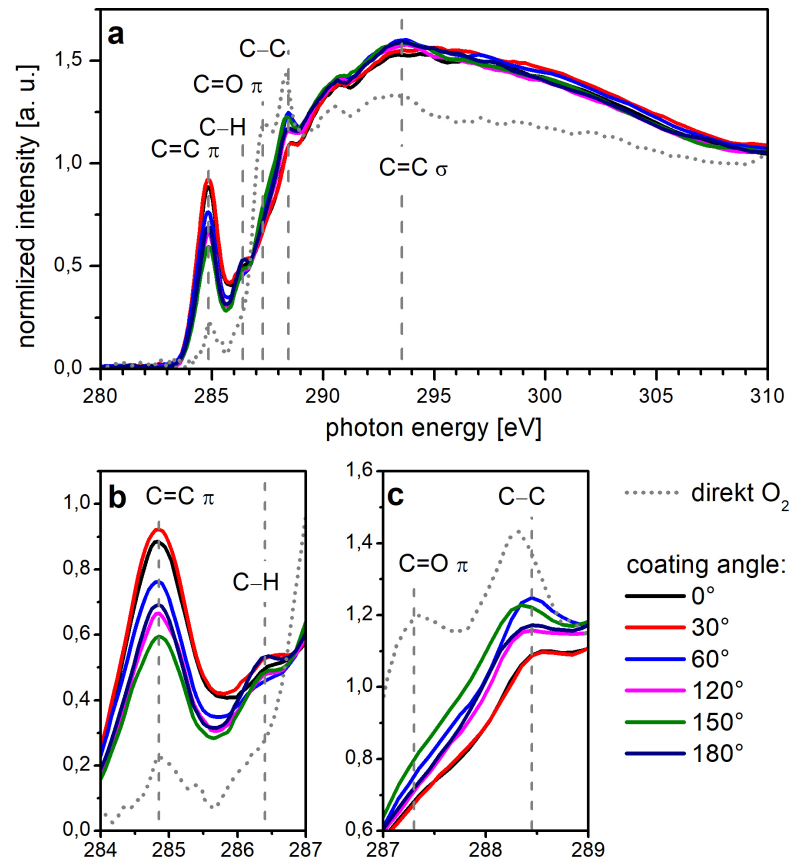
Fig. 69: NEXAFS-data for the 10.0 *min* angle-dependent a-C:H coatings on PHB. In addition, the O_2-plasma 0° treated surface is shown with a gray dotted line. a) Shows the full NEXAFS spectra from 280.0 to 310.0 *eV*. In b) the C=C π (284.85 *eV*) and C−H (286.4 *eV*) peaks are shown between 284.0 to 287 *eV*. c) Shows a magnification between 287.0 to 290.0 *eV* for the C=O (287.3 *eV*) and the C−C peak (here: $\sim$ 288.5 *eV*).

Complementary IR spectroscopy was performed with specular reflection (SR) to obtain further information on the chemical composition of the deposited a-C:H layers. Fig. 70 shows the SR-FTIR spectra for the 10.0 min angle-dependent a-C:H coatings on PHB (spectra of all coating times and angles are summarized in the SI). The evaluation of the spectra was based on the principles of infrared spectroscopy [35] and on [27-29]. First, an overview in the range from 450 to 4100 cm^{-1} was recorded before the C$-$H stretching region at $2750 - 3150 \ cm^{-1}$ was investigated in more detail. The corresponding O_2 treated sample was used as background. As already shown in the NEXAFS, there are also peak shifts in the IR showing the amorphous character of the layers. It should also be noted that the CH_2 bonds typical for an a-C:H layer are formed. The most striking features are the increase and shift of the sp^3CH peak for 10 cm^{-1} at 30° (from $2915 - 2905 \ cm^{-1}$). Up to 120° this remains high, but decreases at 150° and 180° and shifts to 2904 cm^{-1}. The $sp^3CH_2(s)$ position is almost lost in the background noise after direct coating, but can be clearly identified as a larger peak at 150°. In comparison, a particularly clear shift of the C$-$C bonds can also be observed in NEXAFS spectra at this coating angle (Fig. 69c). The shift curve of the symmetrical and asymmetrical oscillation also follows the same course. Beside of this, the $sp^3CH_2(a)$ is the most pronounced peak next to the $sp^2CH_2(s)$, which is in line with earlier observations [9-11]. If one compares the area ratio of the two peaks, it can be seen that the sp^2CH_2 proportion in relation to sp^3CH_2 decreases slightly at 30°, increases strongly at 60°, dominates and is greatest at a coating angle of 180°. These results are consistent with the observations of the XPS analysis (Fig. 68). The slight decrease of sp^2 at 120° for the XPS can also be observed here, even if the sp^3 proportion increases again in the IR, which is due to the different penetration depths of the applied methods. The $sp^2CH_2(a)$ and $sp^3CH_3(a)$ peaks can always be found apart from ($sp^2CH_2(a)$ at 150°) and also show a similar shift behavior.
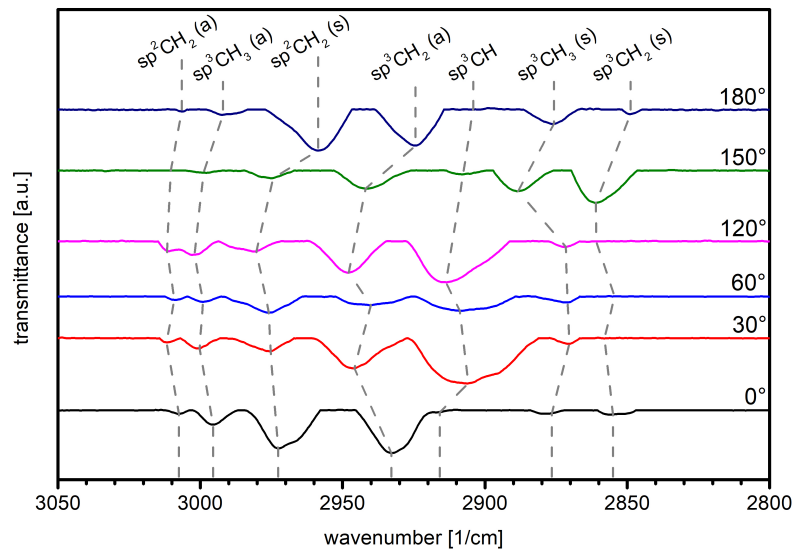
Fig. 70: Evaluated IR spectra for the 10.0 min angle-dependent deposition of a-C:H on PHB. The respective O_2-plasma treated surface is subtracted as background.

9.5.3. Goniometric investigations

Fig. 71 shows the SFE as total, disperse and polar components for the angle-dependent coated surfaces at different times (a: 10.0 min, b: 2.5 min, and c: 5.0 min). The gray area in Fig. 71a indicates the SFE for the PHB surface treated directly with O_2 as a reference. The disperse fraction is much larger here and is subject to fewer fluctuations for all layers than in the O_2 treated sample, but is, as expected, of the same order of magnitude. The polar fraction is also of a similar order of magnitude, but is subject to greater fluctuations as the proportion of SFE is lower. At 2.5 min (71b), an alternation of approx. 5 mN/m can be observed in the SFE with increasing coating angle. Similarly, this can be observed at 5.0 min (71c) in the same direction of deflection with a statistically slight increase. At 10.0 min in Fig. 71a, only a slight alternation at 150° can be observed but the slight increase in the SFE with increasing angle remains. These fluctuations may be due to the fact that the roughness (described at the AFM) in thin layers increases up to the end of the interlayer formation and then changes only slightly. For the dispersed portion at 2.5 min, there are strong fluctuations. These are larger with the direct deposition $(0 - 60°)$ with 35.1 $\pm$ 4.6 mN/m than with the indirect deposition between 120° - 180° with 34.9 $\pm$ 2.3 mN/m. These fluctuations also exist in comparison to the SFE of the surface treated with only O_2 [16]. With the 5.0 min coating, the disperse component remains similarly stable at 33.5 $\pm$ 1.3 mN/m as with 10.0 min at 34.2 $\pm$ 1.8 mN/m. This appears to be the other way around for the polar fraction, with 2.5 min a-C:H coating the fraction for direct coating is stable at approx. 9.4 $\pm$ 0.6 mN/m and indirect coating at 7.3 $\pm$ 0.6 mN/m. If the surface is coated for 5.0 min, the changes in the polar fraction are considerably larger and are approx. 6.0 $\pm$ 3.1 mN/m for direct coating and 8.9 $\pm$ 3.2 mN/m for indirect coating. At 10.0 min a similar picture emerges, but the deviations are smaller; for direct deposition 6.3 $\pm$ 1.4 mN/m and indirect 8.1 $\pm$ 1.5 mN/m. The strong alternation of the surface energy can be explained on the one hand by the fact that the roughness R_q is significantly greater for thin layers (see AFM part, Tab. 7), and also by the fact that the layer is chemically much more stable after completion of the interlayer phase [11]. It should also be noted that the disperse fraction of the SFE does not change depending on the angle and that the coating time appears to have only a minor influence. The polar fraction seems to depend on how the coating is applied. With direct coating, this is greater with approx. 6 mN/m than with approx. 8 mN/m with indirect treatment. Since the error indications are in the same range, it is unlikely that the reduced roughness is the only decisive factor, but that a higher sp^2/sp^3 ratio is the cause.
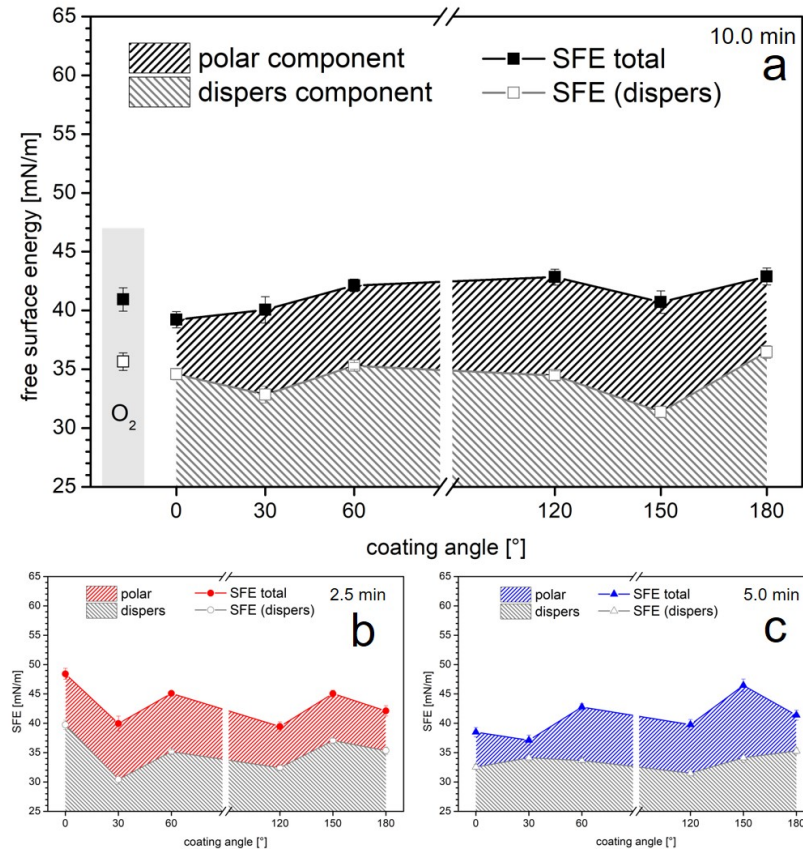
Fig. 71: SFE profiles of PHB coated with a-C:H at different angles $(0 - 180°)$ and different times (2.5, bottom area represent the dispersive component and the top areas the corresponding polar component. a) Shows the profile for 10.0 min; the gray box indicates the values for the direct O_2 treated surface [16]. These are also the reference values for b) 2.5 min and c) 5.0 min.

The contact angle hysteresis is determined indirectly via the difference between the advancing contact angle (ACA) and the receding contact angle (RCA) and provides information about interactions between solids and water droplets. The CAH is a measure of the mobility of a droplet on the surface. Furthermore, it is a measure of wettability, the adhesion of a droplet to the surface, and dewetting, overcoming the adhesive force of the droplet on the surface. Wetting is indicated as ACA and dewetting as RCA, respectively. Fig. 72 shows the CAH of the angle-dependent treated PHB films. The corresponding ACA and RCA values are listed in Tab. 8. Fig. 72a on the one hand shows the mobility of the O_2-treated PHB surface according to earlier results [16], but also the course of mobility after the 10.0 min a-C:H coating. The colored area shows the value distribution of the hysteresis for 10 min a-C:H within the maximum error range. Fig. 72b shows the result for 2.5 min and Fig. 72c for 5.0 min coating time. For the 2.5 min, the particularly large distribution of values is noticeable, which shows statistically large fluctuations. If the corresponding ACA from Tab. 8 is considered, it is noticeable that it also fluctuates very strongly. A comparison with the roughness (Tab. 7) shows a similar trend. Apart from 120°, the RCA remains similar at approx. 30° within the error range. In comparison to the O_2 treated surface, it is not recognizable that the mobility of a water droplet is strongly influenced by a direct coating when a-C:H is applied. At 5.0 min, the value range and the course of the hysteresis stabilize, but

the individual errors are still of a similar order of magnitude. For the ACA and RCA, a slight downward trend can be observed as the angle increases. In the case of the RCA, it should be noted that the error indicators are significantly larger with indirect coating than with direct coating. This can also be seen for the RCA of the 10.0 min coating. As before, the minimum is also found here at 120°. The value range of the CAH is in a similar range as for 5.0 min. Again the error indicators appear to be significantly larger for a coating angle of 60°, which could be due to the increase in the polar component of the SFE.

Table 8: ACA and RCA values for the 2.5, 5.0 and 10.0 min angle-dependent a-C:H depositions on PHB films.

	ACA [°]			**RCA** [°]		
	2.5 min	**5.0 min**	**10.0 min**	**2.5 min**	**5.0 min**	**10.0 min**
0°	67.9 ± 0.3	73.4 ± 1.5	68.5 ± 1.0	31.5 ± 1.5	32.5 ± 1.6	28.6 ± 0.9
30°	63.9 ± 0.5	70.1 ± 0.3	69.9 ± 0.2	30.7 ± 1.3	31.3 ± 1.1	29.8 ± 0.1
60°	73.7 ± 1.2	72.9 ± 0.8	69.4 ± 1.3	30.5 ± 1.8	32.2 ± 0.8	28.7 ± 1.1
120°	65.2 ± 0.4	70.1 ± 1.0	65.5 ± 0.6	26.2 ± 2.2	28.5 ± 2.6	24.7 ± 2.8
150°	61.4 ± 0.8	70.0 ± 0.3	68.7 ± 1.5	29.6 ± 1.0	26.2 ± 2.7	30.8 ± 2.2
180°	70.5 ± 1.2	67.2 ± 0.2	70.4 ± 0.3	29.7 ± 2.4	28.2 ± 2.2	29.8 ± 4.6

Fig. 72: CAH results of PHB surfaces coated with a-C:H at different angles (0 − 180°) and different times (2.5, 5.0 and 10.0 min). The colored areas illustrate the value distribution of the hysteresis within the maximum error range. a) Shows the course for 10.0 min; the empty squares show the angular O_2 treated surface for comparison [16]. These are also the reference values for b) 2.5 min and c) 5.0 min.

9.6. Conclusion

Angle-dependent deposition of a-C:H layers of different thicknesses on a PHB film surface is possible for both direct angles ($0° - 60°$) and indirect coating ($120°$ - $180°$), whereby the deposition rate decreases from 10 nm/min to 2 nm/min and gradient effects can be observed, particularly with direct coating. SEM investigations show stress effects that occur at $30°$ and 10 min, but still with a closed layer. At $0°$ and 10 min, these are more clearly visible, with the layer being cracked. The roughness of the applied layer is significantly larger with the direct coating than with the indirectly applied coating. The chemical analyses show that the sp^2/sp^3 ratio can be varied by changing the layer geometry. The XPS shows that the layer is present for 2.5 min, but the carbon bonds change only slightly, which indicates a forming interlayer. For the remaining coating durations, the sp^3 component dominates at $0°$ and decreases as the coating angle increases. At the same time, the sp^2 proportion increases and becomes dominant earlier as the coating becomes thicker. The SFE revealed that a thicker coating leads to a stabilization of the disperse and polar components. The disperse component stabilizes after 5 minutes of coating. At 10 minutes, the polar component also stabilizes, whereby it splits into a stable direct and indirect part, of which the indirect part is larger. A value stabilization can also be seen in the CAH. Compared to the O_2 treated surface, it is noticeable here that there is no decrease in mobility at $0°$ and the coating angle does not appear to have any influence on a 10.0 min a-C:H layer.

9.7. Acknowledgements

9.8. Author contributions

Conceptualization of the study, developing and organization of processes was arranged by L.B., T.S. and C.B.F. L.B. designed the experimental set up, prepared the samples and performed the data acquisition and evaluation of XPS, NEXAFS, AFM, IR und CA results. L.B. also arranged the overall data curation, visualization and wrote the manuscript draft. L.B., T.S. and C.B.F. validated the results; all authors reviewed and edited the manuscript. Both S.W. and C.B.F. contributed in terms of funding acquisition, project administration, supervision and overall guidance in the study.

9.9. References

[1] H. Brandl, R.A. Gross, R.W. Lenz, R.C. Fuller, Plastics from bacteria and for bacteria: Poly(β-hydroxyalkanoates) as natural, biocompatible, and biodegradable polyesters. Microbial Bioproducts, Adv. Biochem. Eng./Biotechnol., 41 (2005) 77-93 https://doi.org/10.1007/BFb0010232

[2] J. Wong, et. al., Current developments in biotechnology and bioengineering. Elsevier, Amsterdam, Netherlands and Cambridge, MA, United States, 2017

[3] K. Bohmert, I. Balbo, A. Steinbuüchel, G. Tischendorf, L. Willmitzer, Constitutive Expression of the β-Ketothiolase Gene in Transgenic Plants. A Major Obstacle for Obtaining Polyhydroxybutyrate-Producing Plants, Plant Physiol., 128.4 (2002),1282-1290, https://doi.org/ 10.1104/pp.010615

[4] Y. Tokiwa, B.P. Calabia, C.U. Ugwu, S. Aiba, Biodegradability of plastics, Int. J. Mol. Sci., 10 (2009) 3722-3742, https://doi.org/10.3390/ijms10093722

[5] J. C. Chuan Yeo, J. K. Muiruri, W. Thitsartarn, Z. Li, C. He, Recent advances in the development of biodegradable PHB-based toughening materials: Approaches, advantages and applications, Mater. Sci. Eng., 92 (2018) 1092-1116, https://doi.org/10.1016/j.msec.2017.11.006

[6] M. Rohrbeck, S. Körsten, C.B. Fischer, S. Wehner, B. Kessler, Diamond-like carbon coating of a pure bioplastic foil, Thin Solid Films 545 (2013) 558-563, https://doi.org/10.1016/j.tsf.2013.07.028.

[7] A. Catena, S. Agnello, M. Cannas, F.M. Gelardi, S. Wehner, C.B. Fischer, Evolution of the sp2 content and revealed multilayer growth of amorphous hydrogenated carbon (a-C:H) films on selected thermoplastic materials, Carbon, 117 (2017) 351-359, https://doi.org/10.1016/j.carbon.2017.02.093.

[8] L. Beucher, T. Schlebrowski, M. Fritz, S. Wehner, C.B. Fischer, Controlling the sp2/sp3 ratio of amorphous hydrogenated carbon layers (a-C:H) on polylactide acid (PLA) at constant distance but angle-dependent deposition, Appl. Surf. Sci., 629 (2023) 157450, https://doi.org/10.1016/j.apsusc.2023.157450.

[9] T. Schlebrowski, L. Beucher, H. Bazzi, B. Hahn, S. Wehner, C.B. Fischer, T Changing Contents of Carbon Hybridizations in Amorphous Hydrogenated Carbon Layers (a-C:H) on Sustainable Polyhydroxybutyrate (PHB) Exhibit a Significant Deterioration in Stability, Depending on Thickness, C, 5(3) (2019) 52 https://doi.org/10.3390/c5030052.

[10] T. Schlebrowski, R. Ouali, B. Hahn, S. Wehner, C.B. Fischer, comparing the Influence of Residual Stress on Composite Materials Made of Polyhydroxybutyrate (PHB) and Amorphous Hydrogenated Carbon (a-C:H) Layers: Differences Caused by Single Side and Full Substrate Film Attachment during Plasma Coating. Polymers 13 (2021) 184 https://doi.org/10.3390/polym13020184.

[11] T. Schlebrowski, S. Wehner, C.B. Fischer, Thin Amorphous Hydrogenated Carbon Layers on Polylactic Acid and Polyhydroxybutyrate Biopolymers - Influence of Substrate Chemistry on Interlayer Formation, Thin Solid Films 780 (2023) 139943 https://doi.org/10.1016/j.tsf.2023.139943.

[12] J. Robertson, Plasma Deposition of Diamond-Like Carbon, Jpn. J. Appl. Phys. 50 (2011) 01AF01 https://doi.org/10.1143/JJAP.50.01AF01

[13] J. Robertson, Diamond-like amorphous carbon, Mater. Sci. Eng. R 37 (2002) 129-281 https://doi.org/10.1016/S0927-796X(02)00005-0

[14] A. Grill, Plasma-deposited diamondlike carbon and related materials, IBM J. Res. Dev. 43 (1999) 147-162 https://doi.org/10.1147/rd.431.0147

[15] P. Couderc, Y. Catherine, Structure and physical properties of plasma-grown amorphous hydrogenated carbon films, Thin Solid Films 146 (1987) 93-107 https://doi.org/10.1016/0040-6090(87)90343-9

[16] L. Beucher, T. Schlebrowski, K. Rohe, C. B. Fischer, Surface treatment of biopolymer films Polylactic acid and Polyhydroxybutyrat with angular changing oxygen plasma – More than just gradual purification, Surf. Interfaces, 30 (2022) 101856 https://doi.org/10.1016/j.surfin.2022.101856

[17] J.T. Korhonen, T. Huhtamäki1, O. Ikkala, R.H.A. Ras, Reliable Measurement of the Receding Contact Angle, Langmuir, 29 (2013) 3858-3863 https://doi.org/10.1021/la400009m

[18] T. Huhtamäki1, X. Tian, J.T. Korhonen, R.H.A. Ras, Surface-wetting characterization using contact-angle measurements, Nat. Protoc., 13(7) (2018) 1521-1538 https://doi.org/10.1038/s41596-018-0003-z

[19] H.J. Busscher A.W.J. van Pelt, P.de Boer, H.P. de Jong J. Arends, The Effect of Surface Roughening of Polymers on Measured Contact Angles of Liquids, Colloids Surf., 9 (1984) 319-331 https://doi.org/10.1016/0166-6622(84)80175-4

[20] K.F. Gebhardt, Report: Grundlagen der physikalischen Chemie von Grenzflächen und Methoden zur Bestimmung grenzflächenenergetischer Größen, FhG IGB Stuttgart, 1982

[21] A. Nefedov, C. Wöll, Advanced applications of NEXAFS spectroscopy for functionalized surfaces, in: G. Bracco, B. Holst (Eds.), Surface Science Techniques, Springer, Berlin, Heidelberg, (2013) 277-303 http://dx.doi.org/10.1007/978-3-642-34243-1_10

[22] J.L. Solomon, R.J. Madix, J. Stöhr, Orientation and absolute coverage of benzene, aniline, and phenol on Ag(110) determined by NEXAFS and XPS, Surf. Sci. 255 (1991) 12-30 https://doi.org/10.1016/0039-6028(91)90008-G.

[23] F.C. Tai, S.C. Lee, C.H. Wei, S.L. Tyan, Correlation between ID/IG ratio from visible Raman spectra and sp2/sp3 ratio from XPS spectra of annealed hydrogenated DLC film, Mater. Trans. 47 (2006) 1847-1852 https://doi.org/10.2320/matertrans.47. 1847.

[24] P.M. Dietrich, T. Horlacher, P.L. Girard-Lauriault, T. Gross, A. Lippitz, H. Min, T. Wirth, R. Castelli, P.H. Seeberger, W.E.S. Unger, Adlayers of dimannoside thiols on gold: surface chemical analysis, Langmuir 27 (2011) 4808-4815 https://doi.org/10.1021/la104038q.

[25] B. Watts, L. Thomsen, P.C. Dastoor, Methods in carbon K-edge NEXAFS: experiment and analysis, J. Chem. Phys. 140 (2014) 105-120 https://doi.org/10.1016/j. elspec.2005.11.006.

[26] S. Tunmee, et. al.,Investigation of pitting corrosion of diamond-like carbon films using synchrotron-based spectromicroscopy, J. Appl. Phys. 120 (2016) 195303 https://doi.org/10.10 63/1.4967799

[27] E. Tomasella, L. Thomas, M. Dubois, C. Meunier, Structural and mechanical properties of a-C:H thin films grown by RF-PECVD, Diamond Relat. Mater., 13.9 (2004) 1618-1624. https://doi.org/10.1016/j.diamond.2004.01.017

[28] M. Veres, M. Koós, I. Pócsik, IR study of the formation process of polymeric hydrogenated amorphous carbon film, Diamond Relat. Mater., 11 3-6 (2002) 1110-1114 https://doi.org/10.1016/S0925-9635(02)00011-0

[29] P. Koidl, Ch. Wild, B. Dischler, J. Wagner, M. Ramsteiner, Plasma Deposition, Properties and Structure of Amorphous Hydrogenated Carbon Films, Mater. Sci. Forum, 52-53 (1990) 41-70 https://doi.org/10.4028/www.scientific.net/MSF.52-53.41 [30] A. Volinsky, Experiments with in-situ thin film telephone cord buckling delamination propagation, MRS Proceedings 749 (2002) 107 https://doi.org/10.1557/PROC-749-W10.7

[31] S.C. Lee, F.C. Tai, C.H. Wei, Correlation between sp2/sp3 Ratio or Hydrogen Content and Water Contact Angle in Hydrogenated DLC Film, Mater. Trans., 48 9 (2007) 2534-2538 https://doi.org/10.2320/matertrans.MER2007044 [32] J. Diaz, O.R. Monteiro, Z. Hussain, Structure of amorphous carbon from near-edge and extended x-ray absorption spectroscopy, Phys. Rev. B 76 (2007) 094201 https://doi.org/10.1103/PhysRevB.76.094201.

[33] O. Dhez, H. Ade, S. Urquhart, Calibrated NEXAFS spectra of some common polymers, J. Electron Spectrosc. Relat. Phenom. 128 (2003) 85-96 https://doi.org/10.1016/S0368-2048(02)00237-2.

[34] B. Brüster, C. Amozoqueño, P. Grysan, I. Peral, B. Watts, J.-M. Raquez, P. Dubois, F. Addiego, Resolving inclusion structure and deformation mechanisms in polylactide plasticized by reactive extrusion, Macromol. Mater. Eng. 302 (2017) 1700326 https://doi.org/10.1002/mame.201700326.

[35] Günzler, H.; Gremlich, H.-U. IR Spectroscopy. An Introduction; Wiley-VCH: Weinheim, Germany, 2002; ISBN 978-3527288960.

9.10. Supporting Information

9.10.1. X-ray photoelectron spectroscopy (XPS)
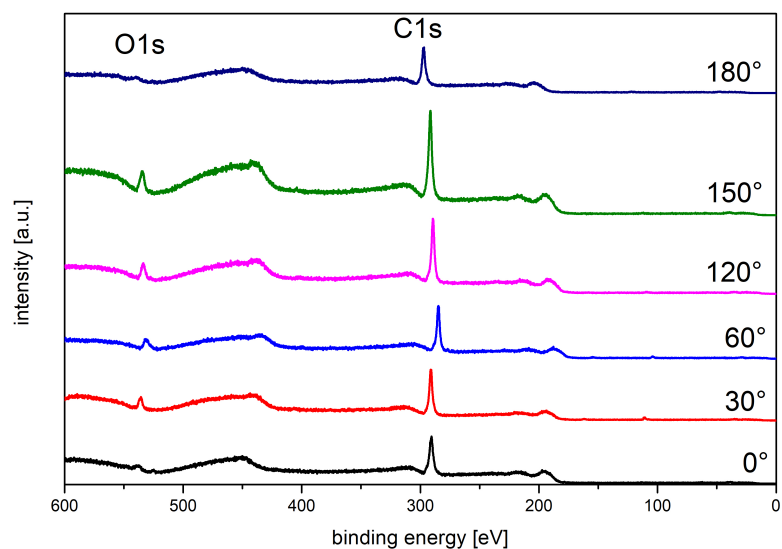
Fig. 73: XPS survey for angle-dependent 2.5 min a-C:H coating on PHB. The O1s and C1s peak is highlighted.
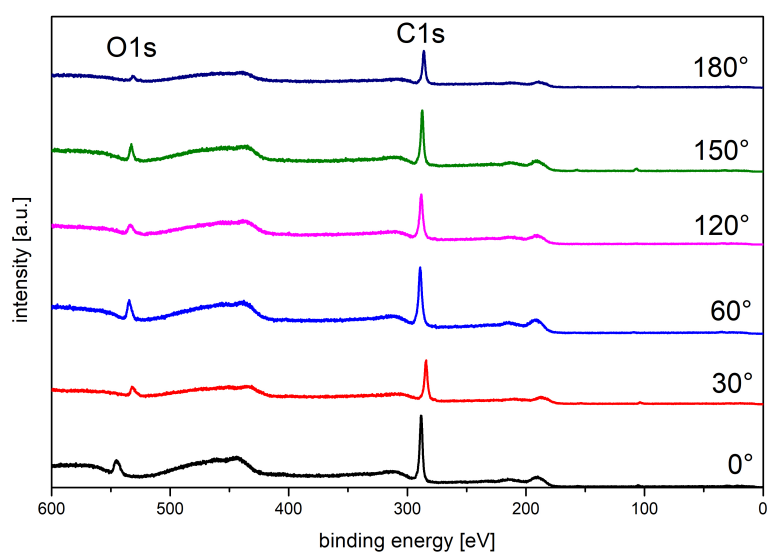
Fig. 74: XPS survey for angle-dependent 5.0 min a-C:H coating on PHB. The O1s and C1s peak is highlighted.
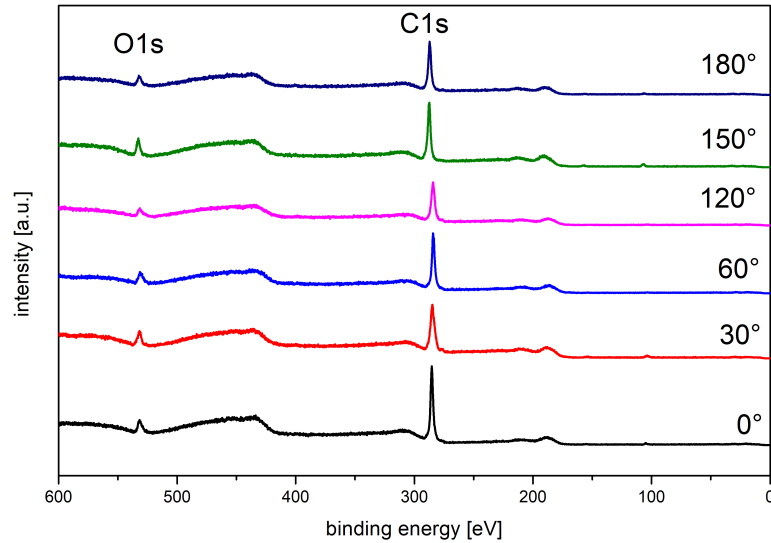
Fig. 75: XPS survey for angle-dependent 10.0 min a-C:H coating on PHB. The O1s and C1s peak is highlighted.

9.10.2. Near edge X-ray absorption fine structure (NEXAFS)

Before the C- and O-edge measurements, the soiling of the grating and mirror artifacts were determined by a gold edge [1S]. In order to minimize charging effects due to beam irradiation an integrated flood gun is used. To prove the reproducibility and the homogeneity, the C-edges shown here was measured at two different positions. Background noise correction spectra normalizing, smoothing and synchronizing with the ring current decay was performed using Origin8.1Pro. The obtained ratios of the relevant bonds are normalized to the C=C π peak by shifting the whole spectrum from the measured position to 284.85 eV [2S-4S].

Fig. 76: NEXAFS for angle-dependent 2.5 min a-C:H coating on PHB. A shows the full NEXAFS spectra from 280.0 to 310.0 eV. B shows a magnification between 287.0 to 290.0 eV for the C=C and the C−H peak. C shows 287.0 to 290.0 eV for the C−C peak.
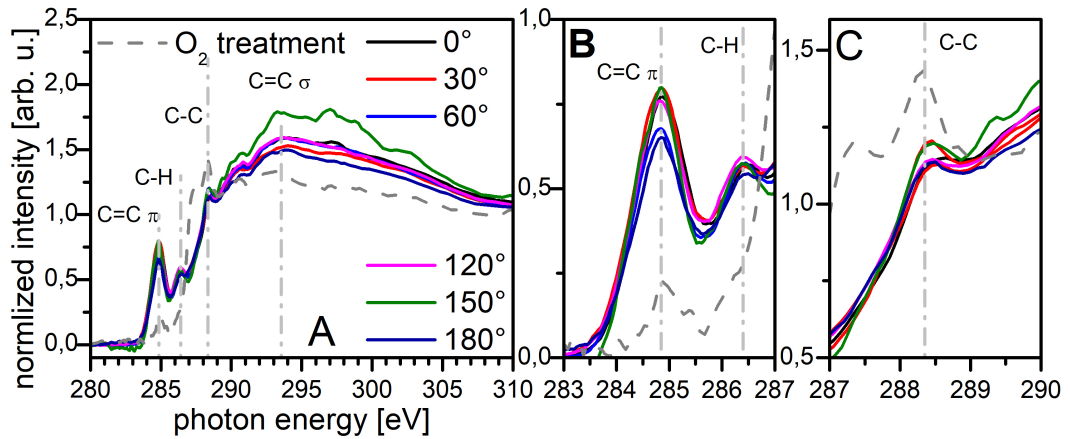
Fig. 77: NEXAFS for angle-dependent 5.0 min a-C:H coating on PHB. A shows the full NEXAFS spectra from 280.0 to 310.0 eV. B shows a magnification between 287.0 to 290.0 eV for the C=C and the C−H peak. C shows 287.0 to 290.0 eV for the C−C peak.

9.10.3. Specular reflectance infrared spectroscopy (SR-FTIR)
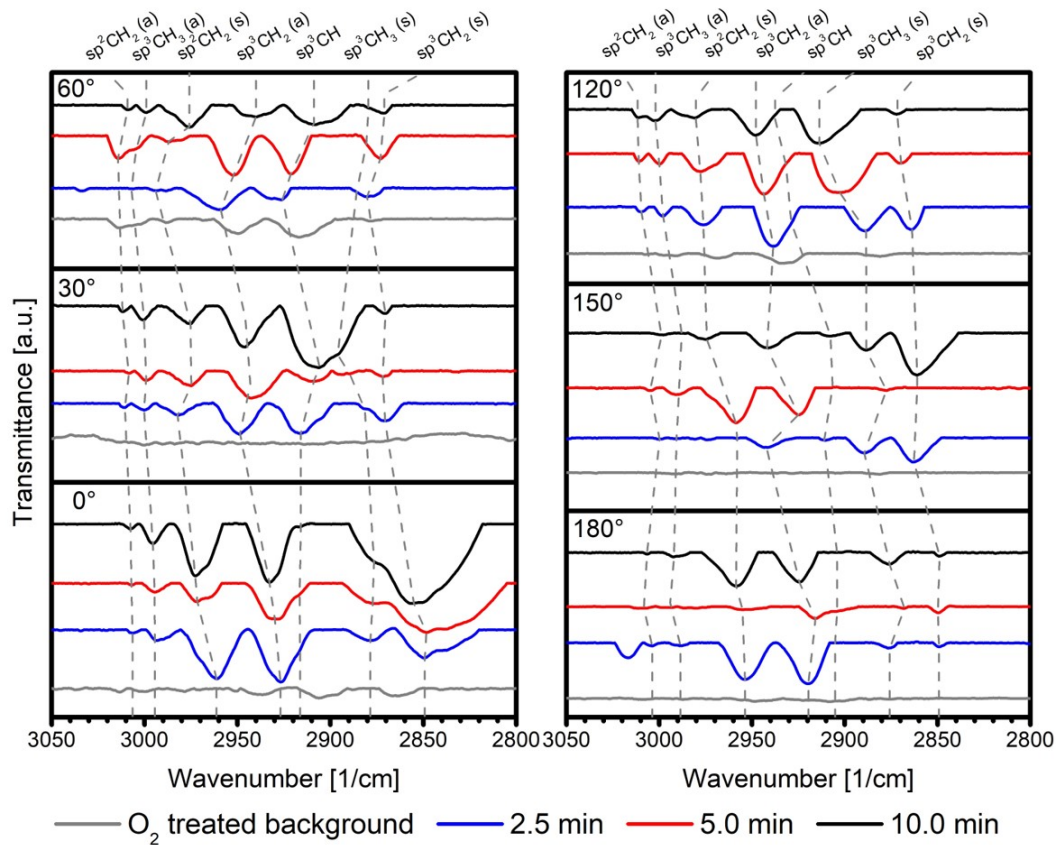
Fig. 78: Evaluated IR spectra angle-dependent deposition of a-C:H with coating times of 2.5, 5.0 and 10.0 min on PHB films. The respective O_2-plasma treated surface is subtracted as background.

9.10.4. Atomic force microscope (AFM)
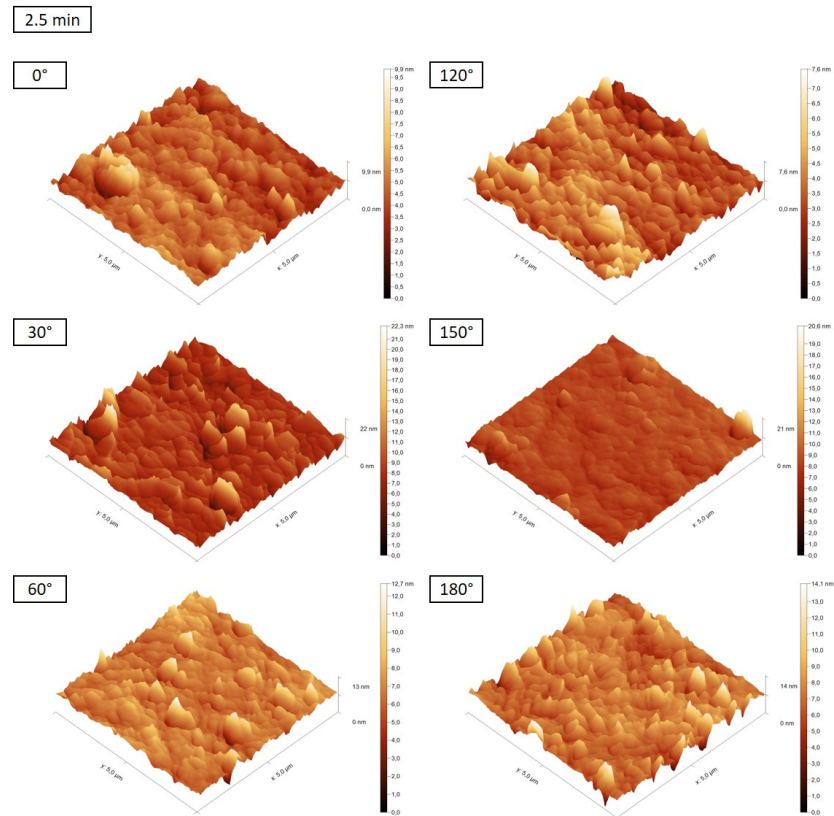
Fig. 79: 5 $\mu m \times$ 5 μm AFM images showing angle-dependent (0° to 180°) 2.5 min a-C:H coating on PHB.
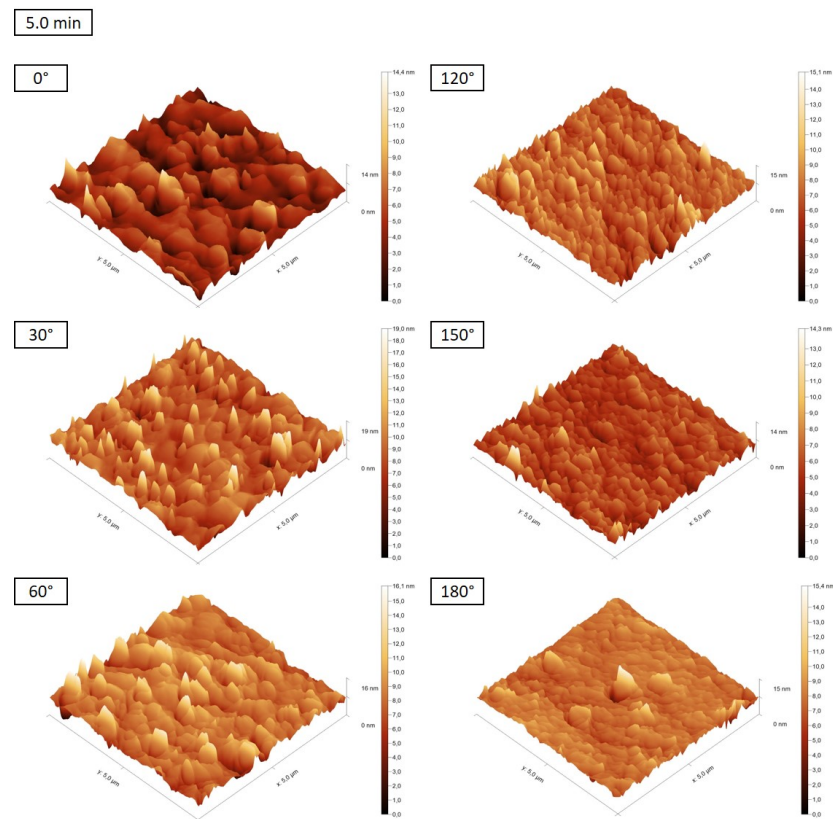
Fig. 80: $5 \ \mu m \times 5 \ \mu m$ AFM images showing angle-dependent ($0°$ to $180°$) $5.0 \ min$ a-C:H coating on PHB.

9.10.5. References SI

[1S] B. Watts, L. Thomsen, P.C. Dastoor, Methods in carbon K-edge NEXAFS: experiment and analysis, J. Chem. Phys. 140 (2014) 105-120, https://doi.org/10.1016/j. elspec.2005.11.0 06.

[2S] J.L. Solomon, R.J. Madix, J. Stöhr, Orientation and absolute coverage of benzene, aniline, and phenol on Ag(110) determined by NEXAFS and XPS, Surf. Sci. 255 (1991) 12-30, https://doi.org/10.1016/0039-6028(91)90008-G.

[3S] F.C. Tai, S.C. Lee, C.H. Wei, S.L. Tyan, Correlation between ID/IG ratio from visible Raman spectra and sp2/sp3 ratio from XPS spectra of annealed hydrogenated DLC film, Mater. Trans. 47 (2006) 1847-1852, https://doi.org/10.2320/matertrans.47. 1847.

[4S] P.M. Dietrich, et.al., Adlayers of dimannoside thiols on gold: surface chemical analysis, Langmuir 27 (2011) 4808-4815, https://doi.org/10.1021/la104038q.

Part IV.
Conclusions

10. Conclusions

The biopolymer films PLA and PHB were treated with variable deposition geometry in an RF-PECVD driven process at first with O_2 plasma. An angle-dependent deposition of a-C:H layers of different thickness on polymer surfaces can also be observed. This is possible with both direct $(0 - 60°)$ and indirect deposition $(120 - 180°)$. However, the deposition rate decreases from 10 nm/min (direct) to 2 nm/min (indirect) and gradient effects can be observed on the entire sample, especially with direct coating. No coating could be applied for a deposition angle of 90°.

The SEM analysis shows that, with a few exceptions, an completely covering intact layer is applied. However, at a coating time of 10 min, cracks can clearly be identified on PLA at 0° and on PHB cord buckling at 0° and 30°, which indicates the release of stress at this layer thickness.

The treatment with only O_2 plasma of PLA shows in the AFM analysis that the entire surface is processed at 0°, which is also visible in the roughness factors. As the angle increases, less structure is treated and the roughness successively decreases until it reaches the value of the starting material at 180°. Compared to the O_2 treated surface, the roughness of the deposited layers on PLA decreases, but does not reach the value for raw PLA. The roughness of the coating itself increases with increasing angle in the direct coating, which contributes to the reduction in CA compared to the O_2 treated layers. In the indirect coating, the roughness decreases abruptly and remains at a similar level. PHB shows linear structures after the O_2 treatment, which do not change due to the plasma process. With a few exceptions, the roughness is very similar here. After coating application, the roughness remains nearly the same, but it is significantly greater with direct coating than with indirect coating.

The polar fraction of the SFE is increased by O_2 plasma in both materials. This effect is greater for PLA than for PHB, but is not substrate-dependent when treated directly with 0°. Only with indirect treatment do the differences between the materials become clear. While PLA shows a slight decrease in the polar fraction at high angles, PHB shows an increase. The disperse fraction also changes and initially decreases with direct O_2 plasma treatment and increases again with indirect angles. For a directly coated PLA surface, the polar fraction of the SFE remains increased. This result is independent of the coating angle with increasing layer thickness in the direct coating. With indirect coating, the polar fraction is initially greater with thicker coating, but then decreases with increasing angle. Alternating bonding fractions and SFEs show here that interlayer properties are present up to a coating thickness of 50 nm (5.0 min for 0°). The disperse fraction stabilizes further with increasing layer thickness via the coating angles. The coating of PHB shows a similar stabilization of the disperse component. With PHB, however, the polar component also fluctuates with thinner layers. The disperse component stabilizes after 5.0 min of coating. After 10.0 min , the polar component also stabilizes, splitting into a stable direct and indirect component. With indirect application, the SFE is statistically greater than with direct coating.

The O_2 plasma treatment of PHB and PLA lowers the mobility of the CAH of a water droplet. It proves to be angle-dependent. The mobility increases with increasing angle with direct O_2 treatment up to 60° and decreases again slightly with indirect treatment. This correlates with the decrease in the polar fraction of the SFE and a reduction in surface

roughness. In comparison to the O_2 treated surface, the coated PHB surface shows that there is no decrease in mobility at 0° and the coating angle does not appear to have any influence on a 10.0 min a-C:H layer. However, as with the SFE, a value stabilization can also be detected here.

The occurrence of a barrier property for PLA with an O_2 plasma treatment of the surface is demonstrated here. Thus, not only cleaning and activation processes are attributed to this treatment, but also changes in the morphological composition of the PLA surface that improve the barrier property. It is also assumed that recombination narrows the pores in PLA. In contrast, an increase in the permeability properties is observed in PHB, which is probably due to increasing erosion of the surface. When coating the PLA surface, it should be noted that the thicker the a-C:H layer in the direct deposits, the greater the barrier properties. In particular, the jump in the WVTR from 2.5 to 5.0 min is significant, as it is assumed that existing pores in the base material are effectively closed. Already at 30° deposition, the transmission is greatly improved; as the angle increases, the behavior becomes asymptotic and only low quality barrier properties are observed. In the case of indirect deposition, the transmission is even higher than for samples treated with O_2. In summary, a successful change in the sp^2/sp^3 ratio is possible for PECVD-mediated a-C:H coatings on biopolymer PLA films in terms of deposition time and angular geometry, with the most significant changes in barrier properties occurring between 0° and 60° with a maximum value of 47%.

The XPS evaluation shows that the basic chemical composition changes only slightly after O_2 treatment. The predominance of sp^3 in untreated PLA and PHB is maintained and varies only slightly. In PLA, the proportion of C−O bonds was shown to exceed that of sp^2, except for 180°. In PHB a different behavior is observed; here the C=O fraction exceeds that of sp^2 only from 150°. The C−O bonds are detectable in small numbers in all samples, except in PHB at 150° and 180°, where they are more than the sp^2 fraction. The chemical arrangement of the surface changes significantly due to the angle-dependent O_2 plasma treatment, but this does not directly lead to a higher number of O-bonds on the surface. The chemical analyses after coating show that the $\frac{sp^2}{sp^3}$ ratio can be varied by changing the layer geometry for both PLA and PHB. For PLA after coating, the XPS shows that sp^3-hybridized bonds dominate for a coating applied at 0° and decrease with increasing angle to their minimum at 180°. The sp^2 fraction is the opposite, it increases and dominates in indirect deposition. The sp^2/sp^3 ratio can therefore be adjusted with the help of the corresponding coating geometry and also causes further changes in the properties. For PHB, the XPS shows that the coating is present for 2.5 min, but the C-bonds change only slightly, indicating a forming interlayer. For the other coating durations, the sp^3 component dominates at 0° and decreases with increasing coating angle. At the same time, the sp^2 component increases and becomes dominant earlier as the coating becomes thicker.

In conclusion, it can be stated that although the $\frac{sp^2}{sp^3}$ ratio can be varied, the application of an indirect layer is economically expensive due to the low deposition rate of 2 nm/min, especially with increasing layer thicknesses. For both PLA and PHB, a thicker layer seems to stabilize the layer properties like the SFE, so that they are less subject to fluctuations. At a layer thickness of 100 nm, the layer starts to break up due to intrinsic stress. This means that the application range of an angle-dependent applied a-C:H layer on PLA or PHB is between

the end of the interlayer at around 50 nm and below 100 nm. The low barrier effect of an indirect layer suggests that the application range of an angle-dependent $\frac{sp^2}{sp^3}$ adaptation in the application interval of $0-60°$ results. Otherwise, only a similar permeability can be achieved with a pure O_2 treatment for PLA.

Danksagung